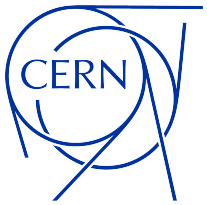

Simulations and measurements to improve the longitudinal quality of fixed target beams at the CERN PS and SPS

Gottfried Wilhelm Leibniz University Hannover
Faculty of Mathematics and Physics
Institute for Theoretical Physics

Master Thesis

Author: Oleksandr Naumenko
MatNr. 10011093

Examiners: Jun.-Prof. Dr. Elina Fuchs
Dr. Giulia Papotti

Submitted on: 05.03.2024

Abstract

Ensuring the delivery of high quality beams from the accelerators to their assigned experiments is one of the primary tasks of CERN. At the Proton Synchrotron (PS) and Super Proton Synchrotron (SPS), fixed-target beams commonly undergo bunch rotations by means of phase jump (henceforth just phase jump) before extraction, which adjusts the beam's longitudinal profile or energy distribution to be suitable for the experiment it is used for. As this is one of the last manipulations performed to adjust the longitudinal qualities of the beam before it reaches the experiment, an optimal phase jump is particularly important. However, there are currently no tools to aid in finding optimal phase jump settings, and experts have to determine them manually in live operation. Therefore, numerical algorithms to optimize phase jump settings automatically are developed in this thesis.

Initially, the SPS SFTPRO beam cycle is targeted, where a homogeneous energy distribution of the beam is desired. By combining simulations of longitudinal beam dynamics using BLonD and longitudinal phase space tomography, a detailed reconstruction of the dynamics is achieved based on measured beam profiles. This reconstruction is performed for various phase jump settings, providing a full overview over the consequences of each setting and determining one providing an optimal energy distribution.

Then, the PS BigTOFEAST cycle is targeted, where two bunches (TOF and EAST) must be extracted at different energies and times. Two phase jumps are studied, with the first one used to extract TOF and the second used to counter-rotate EAST after it is perturbed by the first jump. Numerical simulations tailored to this problem are again developed, tested and finally used to train an optimizer utilizing Bayesian optimization. This optimizer successfully determines physically sensible phase jump settings for both jumps, predicting major improvements if these optimal settings are implemented operationally. Additionally, it predicts that if the bunch intensities increase, highly different optimal phase jump settings can be found, which nevertheless retain close to the original bunch quality.

Zusammenfassung

Eine der Hauptaufgaben des CERN ist es, die Lieferung von qualitativ hochwertigen Strahlen von den Beschleunigern zu den ihnen zugewiesenen Experimenten sicherzustellen. Am „Proton Synchrotron“ (PS) und am „Super Proton Synchrotron“ (SPS) werden fixed-target Strahlen üblicherweise vor der Extraktion mittels Phasensprung „gedreht“. Dadurch wird das longitudinale Profil oder die Energieverteilung des Strahls für das Experiment, für welches der Strahl verwendet wird, angepasst. Da dies eine der letzten Manipulationen ist, die durchgeführt werden, um die longitudinalen Eigenschaften des Strahls anzupassen, ist ein optimaler Phasensprung besonders wichtig. Daher werden in dieser Arbeit numerische Algorithmen zur automatischen Optimierung der Phasensprungeinstellungen entwickelt.

Zunächst wird der SPS SFTPRO-Cycle betrachtet, bei dem eine homogene Energieverteilung des Strahls angestrebt wird. Aufbauend auf Simulationen der longitudinalen Strahlendynamik mit BLonD, longitudinaler Phasenraumtomographie und Messungen des Strahlenverhaltens wird eine detaillierte Rekonstruktion der Teilchenverteilung des Strahls realisiert. Diese Rekonstruktion wird für verschiedene Einstellungen des Phasensprungs durchgeführt, sodass ein vollständiger Überblick über die Konsequenzen jeder Einstellung entsteht und eine optimale Energieverteilung ermittelt werden kann.

Schließlich wird der PS BigTOFEAST Cycle betrachtet, bei dem zwei “Bunches“ (TOF und EAST) bei unterschiedlichen Energien und Zeiten extrahiert werden müssen. Es werden zwei Phasensprünge studiert, wobei der erste zur Extraktion von TOF und der zweite zur Gegen-Rotation der EAST Bunch genutzt wird, nachdem sie durch den ersten Sprung gestört wurde. Auch für dieses Problem werden maßgeschneiderte numerische Simulationen entwickelt, getestet und schließlich verwendet, um einen Optimierer zu trainieren, der Bayes’sche Optimierung verwendet. Dieser Optimierer bestimmt erfolgreich physikalisch sinnvolle Phasensprungeinstellungen für beide Sprünge, und prognostiziert erhebliche Verbesserungen, wenn diese bestimmten Einstellungen im Beschleunigerbetrieb umgesetzt werden. Außerdem wird vorhergesagt, dass bei einer Erhöhung der Strahlenintensität die optimalen Phasensprungeinstellungen stark variieren, aber dennoch die ursprüngliche Bunch-Qualität beibehalten.

Acknowledgements

I am immensely grateful to both Alexandre Lasheen and Giulia Papotti for giving me the chance to work at CERN under their supervision. Both of them have supported me greatly throughout my studies and have always been happy to help with any questions and curiosities I posed to them. I especially thank Giulia for her help on the more practical aspects, such as measurements and accelerator operations, and Alexandre for sharing his deep knowledge of the theoretical side of accelerator physics.

I would also like to thank Elina Fuchs, who despite not being very familiar with the topic of this work, has nonetheless agreed to be my university supervisor and made my work at CERN and this thesis possible. Without her help, and her lectures at CERN, which I attended before starting my studentship, I believe all of this would not have happened.

A big thank you also goes out to everybody from my section at CERN, especially Simon Albright, Danilo Quartullo, Konstantinos Iliakis, Jake Flowerdew, and Bernardo Figueiredo.
Simon has always been kind and very proactive in sharing both his excitement and knowledge, especially of the tomography code used extensively in this thesis. His feedback and encouragement were invaluable.
Danilo helped a lot with his code for creating simulations for the SPS, and even though it was sometimes hard to digest, it was extremely extensive and a great help in getting started.
Kostis was great to collaborate with on the simulation code of BLonD, and without him and Danilo I would not have been able to create half as many simulations as I managed to do. So thank you both for being so helpful and great to work with!
The discussions Jake and I had on the PS, both with and without Alexandre, have also been great for finding new ideas or revising old ones. Thanks for the chats and for reading my thesis on such short notice, Jake! And finally, thanks to my office mate Bernardo for helping me find my place and meet all the people from the section and outside. Without him, I would not be friends and acquaintances with many of the people I know now, and life at CERN would not have been as pleasant as it was.

And to my friends elsewhere: to Kaan, Afrim, Fabian, Johan, Lena and Iola: you were always there for a chat, a fun game, or a deep discussion and everything in between. Thank you for being there for me, regardless of where I am and what I am doing, and thank you for cross-checking my overly detailed writing.

Last, but definitely not least, I would like to give the largest thanks to my mother and wife. Without the year-long support from my mother I would not be here, and her constant support was always a ray of sunshine, no matter whether the day was bright or dark. Thank you for doing everything for me, and letting me undertake this adventure!

And Selin, thank you for encouraging me to make this journey, without you I would not have even considered it. And no-one else would be able to take care of me and show this much love. Thank you for always being there, pushing me to take care of myself and constantly improve, and helping me shape my and our future. Thank you!

Contents

1. Introduction

CERN (*Organisation européene pour la recherche nucléaire*, formerly *Conseil Européen pour la Recherche Nucléaire*) is an international scientific organisation, comprising 23 member states. It operates the world's largest particle physics laboratory for collaborative research into high-energy particle physics, as well as nuclear physics. One of its significant recent discoveries is the observation of a particle compatible with the Higgs Boson, which confirmed the predictions of the standard model [1, 2]. This was accomplished by accelerating protons to near the speed of light in CERN's injector chain, consisting of one linear and three circular accelerators. These protons are successively accelerated to increasing energies in the injectors, until they finally collide in the Large Hadron Collider (LHC), the world's largest particle collider. The data from these collisions is then collected for a multitude of particle physics experiments, performing research on the fundamentals of matter.

However, all machines in the injector chain also deliver particle beams to their own experiments. The objectives of these experiments range from analysing neutron-nucleus interactions (n_TOF [3, 4]), over verifying particle decay statistics (NA62 [5]), to searching for possible dark matter candidates (NA64 [6]). Therefore, the optimal functioning of the entire accelerator complex is a primary objective of CERN [7], as only then the majority of these experiments can be carried out and produce statistically significant results.

1.1. CERN Accelerator Complex

The four injectors of CERN's accelerator complex accelerate various particles, with protons being the focus of this thesis. In the proton case, negative hydrogen ions are first accelerated through the LINAC4 up to 160 MeV, a linear accelerator responsible for increasing particle velocity to a significant fraction of the speed of light. Afterwards, protons are extracted from H^- ions by stripping their electrons, and the beam consisting of approximately 10^{13} protons is accelerated through a series of three synchrotrons, i.e. circular accelerators: the PS Booster (PSB), the Proton Synchrotron (PS) and the Super Proton Synchrotron (SPS), before arriving at the LHC with an energy of

450 GeV. However, a high quality beam is required not only at the LHC, but also at the other accelerators for delivery to their own experiments. This is the focus of this thesis, with delivery to the experiments at the East Area of the PS [8] and the North Area of the SPS [9] being considered herein.

Concretely, for the proton fixed-target experiments in the East and North Areas, the PS accelerates the protons from 2.8 GeV to approximately 24 GeV, while the SPS accelerates from 14 GeV to 400 GeV. After either acceleration, the protons are shot at stationary targets.

Besides protons, heavy ions are also being accelerated at CERN, with the ALICE detector at the LHC being dedicated to analysing their collisions. For example, lead ions are collided at ALICE to reproduce conditions similar to those shortly after the Big Bang [10]. There are also other, smaller experiments such as ISOLDE, which use protons from CERN's accelerators to create a variety of particles for study [11].

1.2. Beam Quality Improvements for Slow Extraction

To guarantee high quality experimental data and safe accelerator operation for North and East Area beams, extraction of a high number of protons with minimal particle losses is desired. This necessitates an optimal distribution of the particles in the longitudinal plane with respect to the beam's direction of travel, just before particle extraction. This, in turn, is achieved by various manipulations of the beam's particle distribution. The manipulation this thesis focuses on is a bunch rotation by means of phase jump, explained in detail in Chapter 2.

In the past, most beam manipulations were optimized by hand: one would devise a method or idea to improve beam quality, and then test the quality of the beam while continuously adjusting the settings until it was optimal. This approach has two main issues:

1. Optimizing by hand can only cover a low amount of possible settings. Therefore, it is possible that the optimizer will only find a local optimum, rather than a global

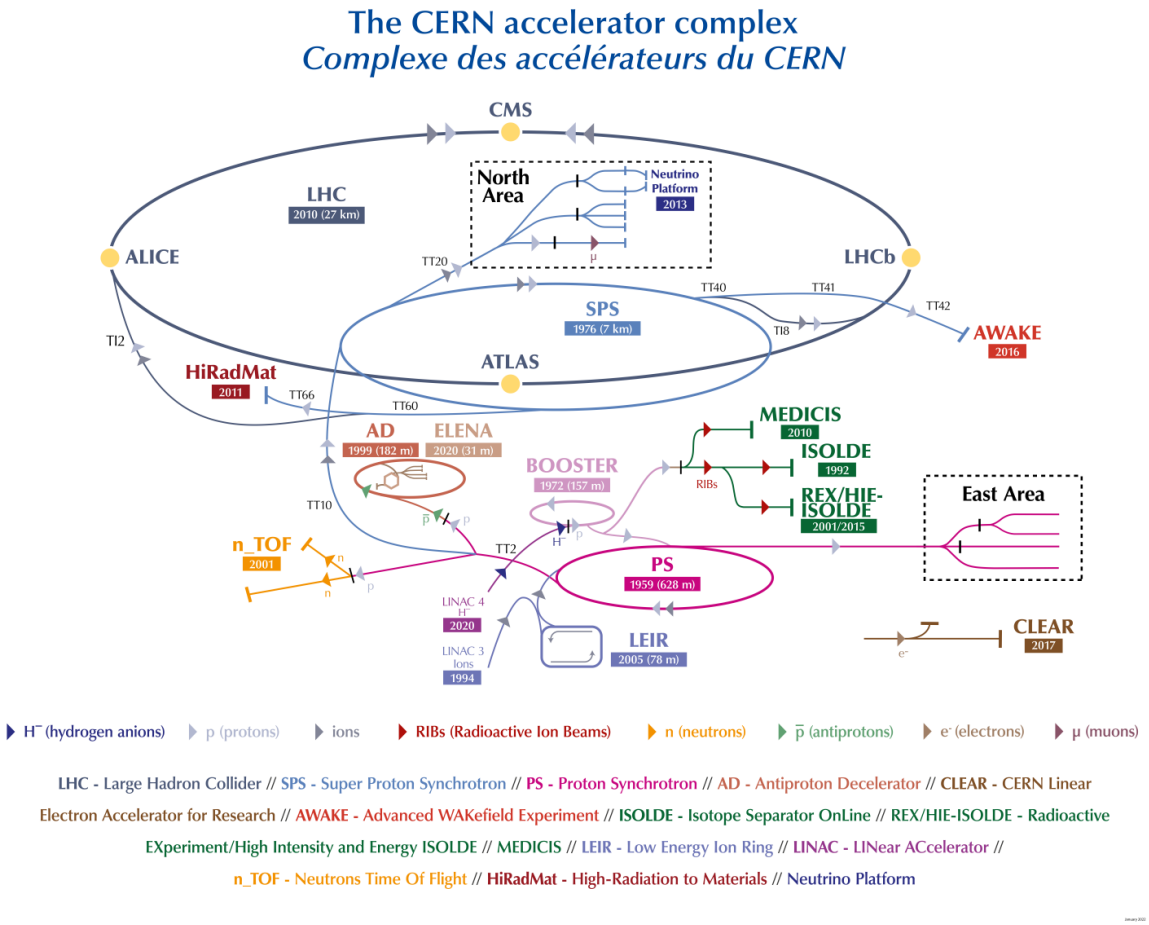

Figure 1.1.1: The CERN accelerator complex as of 2022, with the main proton beam starting at LINAC4, going through the PS Booster, the PS and the SPS, colliding in the LHC.
Source: [12]

one. Additionally, in a system with many settings to optimize, certain interactions might be overlooked, increasing the difficulty of even finding an optimum.

2. During these adjustments, the beam quality might be perturbed, and volatile. Therefore, time to optimize is limited and costly, which amplifies the problems stated above.

While this manual adjustment is invaluable to obtain a fundamental understanding of the problem, once it is obtained, theoretical models and simulations become necessary tools to fine-tune settings without consuming significant machine and personnel time. One can then test the predictions of the simulation by live measurements, improve the model and simulations, and repeat this process until the model is sufficiently accurate. This allows one to discard certain ideas quickly based on the model alone, which is

becoming more important as major projects such as the current High-Luminosity LHC [13] and the planned Future Circular Collider [14] shift manpower away from operation. Nevertheless, limited amounts of machine time remain crucial to iterate on and fully verify these models.

Such an iterative process is done in this thesis for the PS and SPS, with the aim of improving the longitudinal quality of the beam, focusing on settings necessary for optimal particle extraction to the nTOF, and East as well as North Area experiments. To this end, CERN's BLonD code is used for simulations of longitudinal beam dynamics throughout this work [15, 16].

2. Fundamentals of Longitudinal Beam Dynamics

This chapter studies the dynamics of synchrotron motion in the longitudinal plane, i.e. how a particle bunch inside a circular accelerator behaves as it is accelerated, or "stored", i.e. kept at a fixed energy inside the accelerator ring. After elaborating on the basics of longitudinal beam dynamics, bunch rotations by means of phase jump are discussed as a tool for optimizing the particle beam's time and energy distributions before extraction. Then, collective effects are covered, as they can affect the beam as well as phase jump quality significantly and therefore need to be considered in simulations for accurate predictions of real systems. Finally, beam feedback loops are covered to round-off the theoretical overview of beam dynamics and set the groundwork for optimizations performed at the SPS in Chapter 3 and the PS in Chapter 4.

2.1. Particle Motion in a Synchrotron

A synchrotron is a circular particle accelerator which increases the energy of charged particles while confining them to a constant circular orbit through the use of electromagnetic fields (see Fig. (2.1.1)). Electric fields $\vec{\mathcal{E}}$, generated by radio-frequency (RF) cavities, are used for acceleration. Magnetic fields $\vec{B}$, generated by dipole, quadrupole and higher order magnets, are used to maintain the particles on a circular and stable orbit, preventing them from diverging transversally [17]. Note that, by convention, acceleration will henceforth only refer to an increase in the particle momentum's absolute value, i.e. its energy, and not to the change of the momentum vector's direction.

Starting with the fundamentals, the motion of particles with charge q and velocity $\vec{v}$ is governed by the Lorentz force

$$\vec{F} = q(\vec{\mathcal{E}} + \vec{v} \times \vec{B}). \tag{2.1.1}$$

Therefore, the acceleration over a given path $\vec{\mathcal{C}}(t)$, with start and end times t_s and t_e respectively, amounts to an energy gain given by the line integral:

$$\delta E_{\text{accel}} = \int_{\vec{\mathcal{C}}(t)} \vec{F} \cdot \vec{ds} = q \int_{\vec{\mathcal{C}}(t)} \vec{\mathcal{E}} \cdot \vec{ds} + q \int_{\vec{\mathcal{C}}(t)} (\vec{v} \times \vec{B}) \cdot \vec{ds} = q \int_{\vec{\mathcal{C}}(t)} \vec{\mathcal{E}} \cdot \vec{ds}, \tag{2.1.2}$$

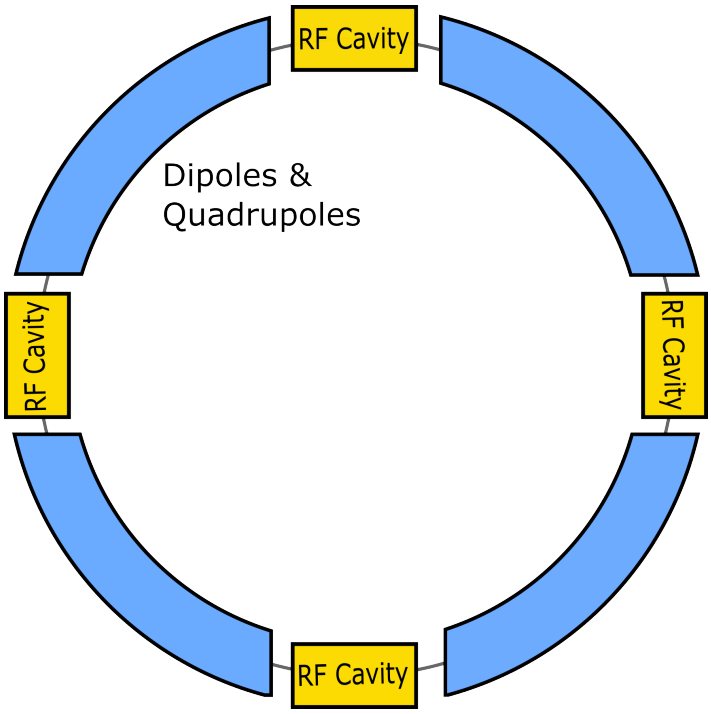

Figure 2.1.1: Simplified schematic of a circular accelerator. Note that sections with an RF cavity are straight and employ electric fields for particle acceleration, while sections with magnets are mainly used to keep the particle on a circular orbit with magnetic fields.

where the magnetic contribution vanishes due to the magnetic field not providing any work:

$$q \int_{\vec{C}(t)} (\vec{v} \times \vec{B}) \cdot \vec{ds} = q \int_{t_s}^{t_e} (\vec{v} \times \vec{B}) \cdot \frac{d\vec{C}(t)}{dt}\, dt = q \int_{t_s}^{t_e} (\vec{v} \times \vec{B}) \cdot \vec{v}\, dt = 0.$$

The centripetal force keeping the particles in orbit is, in turn, generated by the magnetic field. Assuming a perfectly circular synchrotron of radius ρ with magnetic fields perpendicular to the particle's velocity, and particles with mass m, $B = |\vec{B}|$ must therefore fulfil

$$F_{\text{Centripetal}} = \frac{mv^2}{\rho} = qvB = F_{\text{Lorentz}}.$$

This results in the condition

$$B\rho = \frac{p}{q}, \tag{2.1.3}$$

with $p = mv$ being the absolute value of the particle's momentum. Note that this

condition also holds in the relativistic case of $p = \gamma m v$.

Equation (2.1.3) shows that, as a particle accelerates and gains momentum, the magnetic field has to increase to keep it on a constant circular orbit. Therefore, a desired acceleration due to the RF cavities determines the necessary magnetic field over time. In practice, the opposite is usually the case: a maximum magnetic field strength due to technical limitations sets a limit on the particle's momentum and energy.

However, a synchrotron is never perfectly circular, as the magnets can not be placed at every point of the accelerator ring, and straight sections are necessary for the installation of equipment such as RF cavities. Nonetheless, these straight sections are assumed to contain negligible magnetic fields, and similarly, electric fields in curved sections are assumed to vanish. Therefore, Eq. (2.1.3) still holds for particles traversing through bending magnets with the bending radius ρ. Assuming all bending magnets to have the same ρ and neglecting errors due to magnet imperfections or misalignment, a bending radius ρ can hence be defined for the entire synchrotron. However, this bending radius is usually significantly smaller than the geometrical radius.

2.2. Acceleration and Energy Gain

While Eq. (2.1.3) imposes conditions based on the magnetic field, Eq. (2.1.2) describes how the particle gains energy and why RF cavities with time varying electric fields are necessary. Taking the path $\vec{\mathcal{C}}(t)$ to be the full accelerator ring, meaning the integral runs over a closed loop, $\vec{\mathcal{C}}(t_s) = \vec{\mathcal{C}}(t_e) := \vec{s}$, one obtains the energy gain per turn of the particle

$$(\delta E)_{\text{turn}} = q \oint_{\vec{\mathcal{C}}(t_s)}^{\vec{\mathcal{C}}(t_e)} \vec{\mathcal{E}} \cdot \vec{ds}. \tag{2.2.1}$$

The closed-loop integral of a time-independent electric field vanishes according to Maxwell's equations. Therefore, time-varying fields are required to accelerate particles in circular accelerators, and are provided in practice by RF systems. These generate a sinusoidal electric field, oscillating at an angular frequency ω_{rf}, which usually lies in the radio-frequency range, hence the name. Assuming the RF system is placed at a fixed

position in the ring, the provided electric field will be

$$\vec{\mathcal{E}(t)} = \vec{\mathcal{E}_0} \sin(\omega_{\mathrm{rf}} t + \chi_{\mathrm{rf}}), \tag{2.2.2}$$

with the amplitude $\vec{\mathcal{E}_0}$ and a phase offset χ_{rf}.

Consider a single RF cavity along a completely straight section with length l_{rf} parallel to the z-axis. Particles travelling with a velocity v, which is approximately constant in standard operation as the acceleration is small, $\delta E_{\mathrm{turn}}/E \ll 1$, will gain an energy per turn of

$$(\delta E)_{\mathrm{turn}} \overset{t=z/v}{=} q \int_0^{l_{\mathrm{rf}}} \mathcal{E}_0 \sin(\omega_{\mathrm{rf}} \frac{z}{v} + \chi_{\mathrm{rf}})\, dz.$$

The cavities in the SPS are Travelling Wave cavities [18], and can be adjusted such that the phase velocity of the RF waveform matches the particle speed. This means the particle experiences a constant phase

$$\hat{\varphi}_{\mathrm{rf}}(t_{\mathrm{arr}}) = \omega_{\mathrm{rf}} t_{\mathrm{arr}} + \chi_{\mathrm{rf}} \tag{2.2.3}$$

of the electric field as it passes through the cavity, with $\hat{\varphi}_{\mathrm{rf}}(t_{\mathrm{arr}})$ only depending on the time t_{arr} the particle arrives at the entrance of the cavity. Therefore, the above integral reduces to

$$\begin{aligned}(\delta E)_{\mathrm{turn}} &= q\mathcal{E}_0 \int_0^{l_{\mathrm{rf}}} \sin(\hat{\varphi}_{\mathrm{rf}}(t))\, dz = q\mathcal{E}_0 l_{\mathrm{rf}} \sin(\hat{\varphi}_{\mathrm{rf}}(t_{\mathrm{arr}})) \\ &= qV_{\mathrm{rf}} \sin(\hat{\varphi}_{\mathrm{rf}}(t_{\mathrm{arr}})),\end{aligned} \tag{2.2.4}$$

where $V_{\mathrm{rf}} = \mathcal{E}_0 l_{\mathrm{rf}}$ is the RF cavity voltage.

This cannot be done for Standing Wave cavities, such as the ones used in the PS. However, for a large circumference C, i.e. $l_{\mathrm{rf}} \ll C$, the above equation approximately holds [19, Eq. (2.12)]. As this approximation is valid for the PS, Eq. (2.2.4) is assumed to hold for both the PS and SPS, and therefore throughout this thesis.

Note that for particles to gain the same energy turn after turn, $\sin(\hat{\varphi}_{\mathrm{rf}}(t_{\mathrm{arr}}))$ has to assume the same value at each turn. Therefore, if a particle during revolution turn n

arrives at $t_{\text{arr}}^{(n)}$, and then in the next turn $n+1$ at $t_{\text{arr}}^{(n+1)}$, the following has to hold:

$$\begin{aligned} &\sin(\hat{\varphi}_{\text{rf}}(t_{\text{arr}}^{(n)})) = \sin(\hat{\varphi}_{\text{rf}}(t_{\text{arr}}^{(n+1)})) = \sin(\hat{\varphi}_{\text{rf}}(t_{\text{arr}}^{(n)} + T_{\text{rev}}^{(n)})) \\ \implies &\sin(\omega_{\text{rf}}^{(n)} t_{\text{arr}}^{(n)} + \chi_{\text{rf}}) = \sin(\omega_{\text{rf}}^{(n)} t_{\text{arr}}^{(n)} + \chi_{\text{rf}} + \omega_{\text{rf}}^{(n)} T_{\text{rev}}^{(n)}) \\ \implies &\omega_{\text{rf}}^{(n)} T_{\text{rev}}^{(n)} = 2\pi h \\ \implies &\omega_{\text{rf}}^{(n)} = h\omega_{\text{rev}}^{(n)}. \end{aligned} \tag{2.2.5}$$

Here, $h \in \mathbb{N}$ is called the harmonic number, determining the ratio between RF and revolution frequencies.
So for a given revolution time $T_{\text{rev}}^{(n)} = 2\pi/\omega_{\text{rev}}^{(n)}$ or frequency $\omega_{\text{rev}}^{(n)}$ at turn n, the RF frequency $\omega_{\text{rf}}^{(n)}$ has to be exactly an integer multiple of $\omega_{\text{rev}}^{(n)}$, and be adjusted to fulfil this condition turn by turn.

In practice, technological limitations on the magnets' ramp rate $\dot{B}(t)$ set a maximum momentum gain per turn $\dot{p}(t)$ through Eq. (2.1.3). Therefore, a maximum energy gain per turn is also imposed, as $\dot{E}(t) = \beta c\dot{p}(t)$. Based on this limitation, a target $(\delta E)_{\text{turn}}$ is chosen, which is realized by installing RF cavities with a matching voltage V_{rf}, programmed phase $\hat{\varphi}_{\text{rf}}$ and frequency ω_{rf} to accelerate the particles.

However, the problem becomes more complex when considering not one, but on the order of 10^{13} particles that compose an accelerator beam. Such a beam usually consists of multiple particle bunches, meaning groups of particles that are separated spacially. To fully describe the beam dynamics, one studies the dynamics of each bunch, i.e. the change of the particle distribution within the bunch over time. What drives these dynamics is the fact that most particles do not arrive exactly at the target time t_{arr}, causing oscillations of the distribution.

2.3. Longitudinal Equations of Motion

Now consider a particle bunch, as demonstrated in Fig. (2.3.1). The particles obey the equations outlined previously and are centred around a reference particle. This reference particle follows a design energy program, meaning it has precisely the desired target energy values $E_0^{(n)}$ at every revolution turn n. This directly determines all relevant quantities of the particle trajectory, i.e. a design momentum $p_0^{(n)}$, relativistic

velocity $\beta_0^{(n)} = v_0^{(n)}/c$ and therefore angular frequency $\omega_{\mathrm{rev},0}^{(n)} = \beta_0^{(n)} c/\rho$, alongside the period of revolution $T_{\mathrm{rev},0}^{(n)} = 2\pi/\omega_{\mathrm{rev},0}^{(n)}$. It also determines the necessary magnetic field $B_0^{(n)}$ via Eq. (2.1.3).

If the voltage of the RF system is fixed in advance, the energy program also defines the phase $\hat{\varphi}_{\mathrm{rf}}(t_{\mathrm{arr},0}^{(n)})$ necessary at the reference particle's arrival. Namely, Eq. (2.2.4) implies

$$E_0^{(n+1)} - E_0^{(n)} := (\delta E)_0^{(n)} = qV_{\mathrm{rf}} \sin(\hat{\varphi}_{\mathrm{rf}}(t_{\mathrm{arr},0}^{(n)})),$$

thus the so-called synchronous phase $\varphi_0^{(n)}$ is given by

$$\omega_{\mathrm{rf}}^{(n)} t_{\mathrm{arr},0}^{(n)} + \chi_{\mathrm{rf}} = \hat{\varphi}_{\mathrm{rf}}(t_{\mathrm{arr},0}^{(n)}) =: \varphi_0^{(n)} = \arcsin\left(\frac{(\delta E)_0^{(n)}}{qV_{\mathrm{rf}}}\right), \tag{2.3.1}$$

while $\omega_{\mathrm{rf}}^{(n)}$ is determined via Eq. (2.2.5).

However, any particle with a slightly different arrival time relative to the reference particle will see a different phase and therefore move on a different trajectory. Let the difference in arrival time between an arbitrary particle $t^{(n)}$ and the reference particle $t_0^{(n)} = \sum_{i=1}^{n} T_{\mathrm{rev},0}^{(i)}$ at revolution turn n be

$$\Delta t^{(n)} := t^{(n)} - t_0^{(n)}.$$

The difference in energy can be defined similarly as

$$\Delta E^{(n)} := E^{(n)} - E_0^{(n)}.$$

As seen in Fig. (2.3.1), these coordinates define a phase space, which fully characterises the longitudinal dynamics of the particle bunch, as will be elaborated on below.

To calculate the dynamics of the aforementioned coordinates, ΔE is studied first. To determine its dynamics, the phase at the arrival time of an arbitrary particle must be

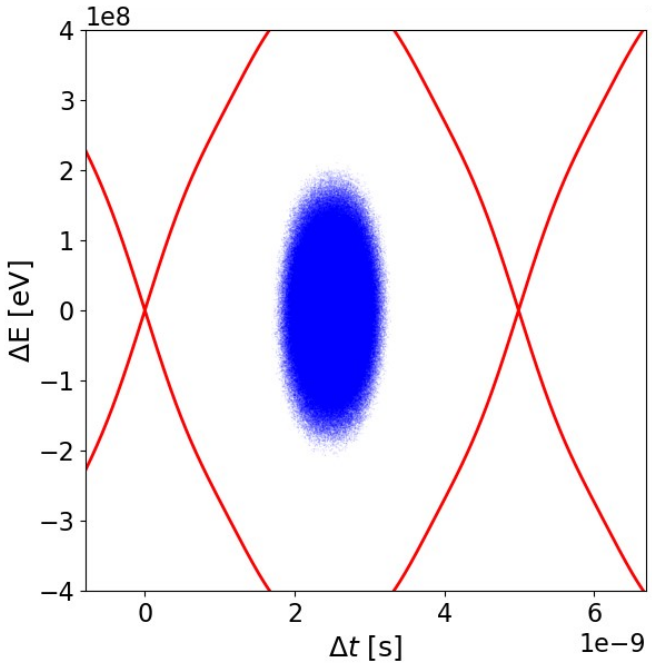

Figure 2.3.1: The phase space of a typical SPS bunch. Particles are coloured in blue. The time difference is shown on the x-axis, while the y-axis displays the energy difference. Note that the Δt coordinate on the x-axis is shifted such that the 0 lies on the left. The red envelope defines the separatrix, which will be discussed in Sec. 2.4.

considered:

$$\begin{aligned}\varphi(t^{(n)}) &= \int_0^{t^{(n)}} \omega_{\mathrm{rf}}(\tau)\, d\tau + \chi_{\mathrm{rf}}^{(n)} \\ &= \sum_{i=1}^{n} \omega_{\mathrm{rf}}^{(i)} T_{\mathrm{rev},0}^{(i)} + \omega_{\mathrm{rf}}^{(n)}(t^{(n)} - t_0^{(n)}) + \chi_{\mathrm{rf}}^{(n)} \\ &= \sum_{i=1}^{n} \omega_{\mathrm{rf}}^{(i)} T_{\mathrm{rev},0}^{(i)} + \omega_{\mathrm{rf}}^{(n)} \Delta t^{(n)} + \chi_{\mathrm{rf}}^{(n)},\end{aligned}$$

where $\omega_{\mathrm{rf}}(\tau)$ only changes after every turn due to the discretized energy gain, and $\omega_{\mathrm{rf}}^{(i)} T_{\mathrm{rev},0}^{(i)}$ is a multiple of 2π for every turn i due to Eq. (2.2.5). Therefore, the energy after an additional turn is

$$\begin{aligned}E^{(n+1)} &= E^{(n)} + \delta E^{(n)} = E^{(n)} + qV_{\mathrm{rf}} \sin(\varphi(t^{(n)})) \\ &= E^{(n)} + qV_{\mathrm{rf}} \sin(\omega_{\mathrm{rf}}^{(n)} \Delta t^{(n)} + \chi_{\mathrm{rf}}^{(n)}).\end{aligned}$$

Then the energy difference between the arbitrary and reference particle is

$$\begin{aligned}\Delta E^{(n+1)} &= E^{(n+1)} - E_0^{(n+1)} \\ &= (E^{(n)} + \delta E^{(n)}) - (E_0^{(n)} + \delta E_0^{(n)}) \\ &= \Delta E^{(n)} + qV_{\mathrm{rf}} \sin(\omega_{\mathrm{rf}}^{(n)} \Delta t^{(n)} + \chi_{\mathrm{rf}}^{(n)}) - \delta E_0^{(n)}.\end{aligned} \tag{2.3.2}$$

On the other hand, the time difference $\Delta t^{(n)}$ depends purely on the difference in revolution periods between the particles, implying

$$\Delta t^{(n+1)} = \Delta t^{(n)} + T_{\mathrm{rev}}^{(n+1)} - T_{\mathrm{rev},0}^{(n+1)} = \Delta t^{(n)} + T_{\mathrm{rev},0}^{(n+1)} \left(\left(1 + \frac{\omega_{\mathrm{rev}}^{(n+1)} - \omega_{\mathrm{rev},0}^{(n+1)}}{\omega_{\mathrm{rev},0}^{(n+1)}} \right)^{-1} - 1 \right). \tag{2.3.3}$$

The so-called frequency slippage $\omega_{\mathrm{rev}} - \omega_{\mathrm{rev},0} =: \Delta\omega_{\mathrm{rev}}$ in the numerator can be quantified by a machine parameter $\eta(\delta)$, determined by the configuration of magnets ("magnetic lattice") installed in the synchrotron. It defines how a difference in momentum relative to the reference particle $\delta = \Delta p/p_0 = \Delta E/(\beta_0^2 E_0)$ affects the particle orbit. Specifically, it quantifies how a particle with higher momentum is faster, but must also traverse a circular orbit of larger radius. Mathematically:

$$\frac{\Delta\omega_{\mathrm{rev}}}{\omega_{\mathrm{rev},0}} =: -\delta\eta(\delta) = -\delta(\eta_0 + \eta_1\delta + \eta_2\delta^2 + \mathcal{O}(\delta^3)). \tag{2.3.4}$$

For a small frequency slippage, $\Delta\omega_{\mathrm{rev}}/\omega_{\mathrm{rev},0} \ll 1$, or equivalently, a well centred bunch around the reference particle, $\Delta E/E_0 \ll 1$, taking only the first order in above equation is a valid approximation, yielding

$$\begin{aligned}\Delta t^{(n+1)} &\approx \Delta t^{(n)} + T_{\mathrm{rev},0}^{(n+1)} \left(\left(1 - \eta_0^{(n+1)} \frac{\Delta E^{(n+1)}}{(\beta_0^{(n+1)})^2 E_0^{(n+1)}} \right)^{-1} - 1 \right) \\ &\overset{\frac{\Delta E}{E_0} \ll 1}{\approx} \Delta t^{(n)} + \left(\frac{T_{\mathrm{rev},0}^{(n+1)} \eta_0^{(n+1)}}{(\beta_0^{(n+1)})^2 E_0^{(n+1)}} \right) \Delta E^{(n+1)}.\end{aligned} \tag{2.3.5}$$

These two Equations (2.3.2) and (2.3.5) define a dynamic map between turn n and $n+1$, fully describing the dynamics in longitudinal phase space. They show how a particle with a higher energy will, depending on the sign of η_0, arrive later or earlier during the next revolution turn. This difference in arrival time Δt will then change

the difference in energy ΔE in the next turn, and so on. Under the right conditions, this phase space dynamic creates a stable oscillation around the reference (also called synchronous) particle. This means a higher Δt reduces ΔE, which in turn reduces Δt, etc. (see Section 2.4).
The equations are also simple to implement numerically, where the kick (Eq. (2.3.2)) and then the drift (Eq. (2.3.5)) is applied to every simulated particle's coordinates, yielding the coordinates for the next turn. This is repeated, yielding the particle dynamics for the desired number of turns.

If multiple RF stations are to be considered, in theory the equations need to be applied for each RF station. So if there are two stations, one would have to calculate the change in coordinates due to the first station $\Delta E^{(n)}(1)$ and $\Delta t^{(n)}(1)$, and then due to the second, $\Delta E^{(n)}(2) = \Delta E^{(n+1)}$ and $\Delta t^{(n)}(2) = \Delta t^{(n+1)}$. These changes would depend on the system parameters $\omega_{\mathrm{rev},0}(t), \eta_0(t)$,..., which change over time and are different for the arrival times at the first and second RF stations. However, the approximation of a centred bunch $\Delta E/E_0 \ll 1$ made in deriving Eq. (2.3.5), in most cases also corresponds to slow acceleration, $\delta E_0/E_0 \ll 1$. For slow acceleration, the small change of the variables $\omega_{\mathrm{rev},0}, \eta_0$,... between the two RF stations is negligible. This allows to approximate the kicks due to the RF stations by a sum of kicks, all based on the parameters of the previous turn, which also summarizes the drifts similarly:

$$\Delta E^{(n+1)} \approx \Delta E^{(n)} + \sum_{k=1}^{N_{\mathrm{rf}}} qV_{\mathrm{rf},k} \sin(\omega_{\mathrm{rf},k}^{(n)} \Delta t^{(n)} + \chi_{\mathrm{rf},k}^{(n)}) - \delta E_0^{(n)}, \tag{2.3.6}$$

$$\Delta t^{(n+1)} \approx \Delta t^{(n)} + \left(\frac{T_{\mathrm{rev},0}^{(n+1)} \eta_0^{(n+1)}}{(\beta_0^{(n+1)})^2 E_0^{(n+1)}} \right) \Delta E^{(n+1)}, \tag{2.3.7}$$

where k numbers all N_{rf} RF stations with their own voltages $V_{\mathrm{rf},k}$, angular frequencies $\omega_{\mathrm{rf},k}$ and phase offsets $\chi_{\mathrm{rf},k}$.

Finally, by the same argument of slow acceleration and therefore only small changes turn by turn, transforming these discrete equations into continuous ones is a valid approximation. Assuming that variables over a revolution turn only change infinitesimally,

$\frac{\Delta E^{(n+1)} - \Delta E^{(n)}}{T_{\mathrm{rev},0}^{(n+1)}} \approx \frac{d(\Delta E)}{dt} =: \dot{\Delta E}(t)$ and analogously for $\dot{\Delta t}$, yields:

$$\dot{\Delta E}(t) = \frac{q}{T_{\mathrm{rev},0}(t)} \sum_{k=1}^{N_{\mathrm{rf}}} V_{\mathrm{rf},k} \sin(\omega_{\mathrm{rf}}(t)\Delta t + \chi_{\mathrm{rf},k}(t)) - \frac{\delta E_0(t)}{T_{\mathrm{rev},0}(t)}, \tag{2.3.8}$$

$$\dot{\Delta t}(t) = \left(\frac{\eta_0(t)}{(\beta_0(t))^2 E_0(t)} \right) \Delta E(t), \tag{2.3.9}$$

where all variables previously dependent on the turn number n now depend on the time t.

2.4. System Hamiltonian

The equations of motion describe a Hamiltonian system with the conjugate variables $(\Delta t, \Delta E)$. For an example of its behaviour under small excitations, see Appendix A. More generally, the full system Hamiltonian is given by integrating the continuous equations (2.3.8), (2.3.9):

$$\begin{aligned} H(\Delta t, \Delta E) &= \int \frac{d(\Delta t)}{dt}\, d(\Delta E) - \int \frac{d(\Delta E)}{dt}\, d(\Delta t) \\ &= \frac{\eta_0}{2(\beta_0)^2 E_0} \Delta E^2 + \frac{q}{T_{\mathrm{rev},0}} \sum_{k=1}^{N_{\mathrm{rf}}} \frac{V_{\mathrm{rf},k}}{\omega_{\mathrm{rf},k}} \cos(\omega_{\mathrm{rf},k}\Delta t + \chi_{\mathrm{rf},k}) + \frac{\delta E_0}{T_{\mathrm{rev},0}} \Delta t + C_H, \end{aligned} \tag{2.4.1}$$

where C_H is an integration constant, usually defined to set the minimum of the RF potential

$$U_{\mathrm{rf}}(\Delta t) := \frac{q}{T_{\mathrm{rev},0}} \sum_{k=1}^{N_{\mathrm{rf}}} \frac{V_{\mathrm{rf},k}}{\omega_{\mathrm{rf},k}} \cos(\omega_{\mathrm{rf},k}\Delta t + \chi_{\mathrm{rf},k}) + \frac{\delta E_0}{T_{\mathrm{rev},0}} \Delta t + C_H \tag{2.4.2}$$

to 0, $\min_{\Delta t}\{U_{\mathrm{rf}}(\Delta t)\} = 0$.

As this system is described by a Hamiltonian, two main consequences for the synchrotron motion follow:

1. The Liouville theorem holds, hence the volume enclosed by particle trajectories is constant.

2. Due to the Hamiltonian being independent of the system time, $\frac{dH}{dt} = \frac{\partial H}{\partial t} = 0$, it is itself a constant of motion, $H(\Delta t, \Delta E) = \text{const}$.

Using the second fact, an equation for the particle trajectories can be derived. Eq. (2.4.1) implies

$$\Delta E(\Delta t) = \pm\sqrt{\frac{2(\beta_0)^2 E_0}{\eta_0}(H(\Delta t, \Delta E) - U_{\text{rf}}(\Delta t))},$$

and since $H(\Delta t, \Delta E) = \text{const} = H(\Delta t_A, 0) = U_{\text{rf}}(\Delta t_A)$,

$$\Delta E(\Delta t) = \pm\sqrt{\frac{2(\beta_0)^2 E_0}{\eta_0}(U_{\text{rf}}(\Delta t_A) - U_{\text{rf}}(\Delta t))}, \tag{2.4.3}$$

with Δt_A being the Δt-amplitude of the phase space oscillation associated with the considered trajectory. Various trajectories and potentials for different values of acceleration are displayed in Fig. (2.4.1a) and Fig. (2.4.1b). Note that the x coordinate used in these figures is the particle phase $\varphi(\Delta t) = \omega_{\text{rf}}\Delta t + \chi_{\text{rf}}$, which relates the particles' arrival time offset Δt to the RF phase.

Evaluating this equation for the stable trajectory with the maximal time amplitude $\Delta t_A^{\max}$ yields the separatrix, which encloses all stable trajectories. $\Delta t_A^{\max}$ is defined by the position of the RF potential's smallest local maximum, $\min\{U_{\text{rf}}(\Delta\tau) \,|\, \Delta\tau \text{ maximizes } U_{\text{rf}}\} = U(\Delta t_A^{\max})$. By definition, any particles going beyond this maximal $\Delta t_A^{\max}$ have enough energy to leave the potential well, hence they no longer perform bounded, stable motion. Due to the first consequence mentioned above, the total area containing stable trajectories is constant. Therefore, to have a stable bunch of particles, they need to initially lie within the area defined by the separatrix. The separatrix, in turn, is defined by the system parameters in Eq. (2.4.3), evaluated at $\Delta t_A^{\max}$, therefore allowing one to predict the trajectories based on the chosen system parameters.

This area enclosed by the separatrix is called the RF bucket. Due to Liouville's theorem, particles "caught in the RF bucket", i.e. the ones within this area, move on stable trajectories, never leaving the bucket. Note that, in the special case of no acceleration, the bucket's Δt width is maximal, corresponding exactly to one RF period. Therefore,

the maximal bucket width is given by

$$T_{\mathrm{rf}} = \frac{1}{f_{\mathrm{rf}}}. \tag{2.4.4}$$

In conclusion, given the Hamiltonian in Eq. (2.4.1), as well as the equations of motion (2.3.8) and (2.3.9), the dynamics of a particle in longitudinal phase space can be calculated. This enables the determination of the necessary accelerator and RF parameters to capture a certain bunch of particles in a given bucket, or vice versa, to see how a certain bunch of particles behaves with given accelerator parameters.

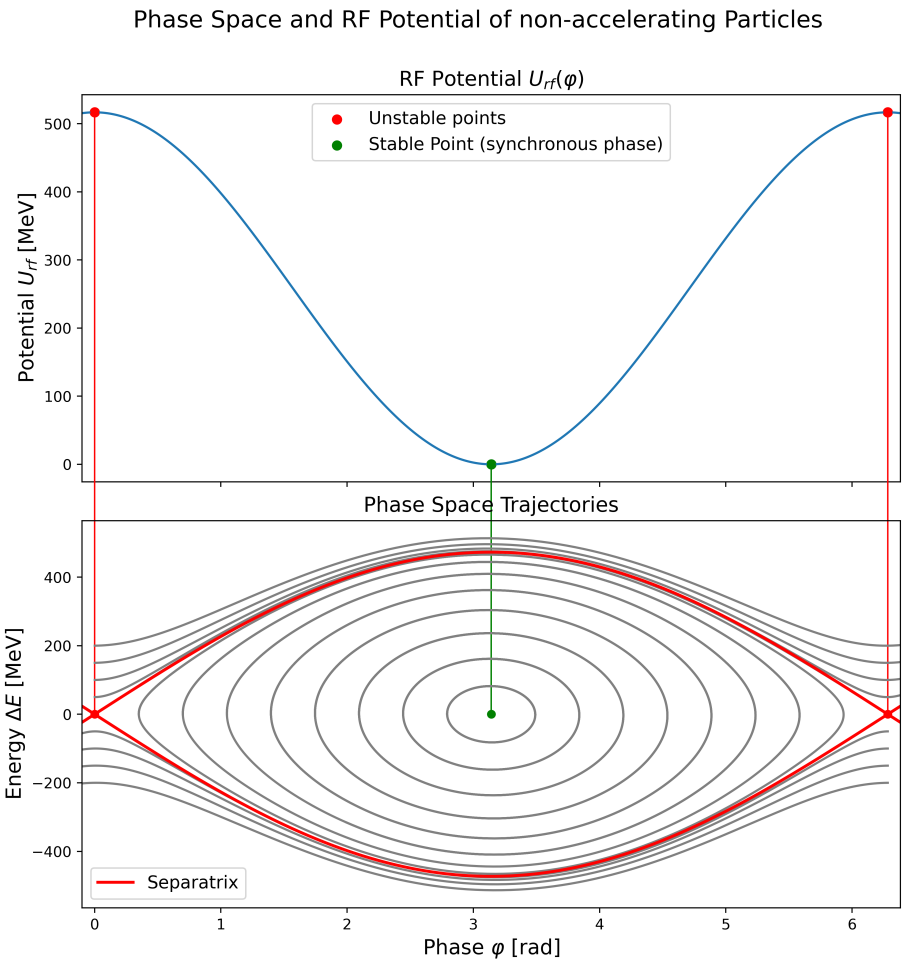

(a) The non-accelerating case. The minimum of the potential occurs at the synchronous phase φ_0, while the maxima yield the φ amplitude of the largest stable orbit and thereby $\Delta t_A^{\max}$ for the separatrix.

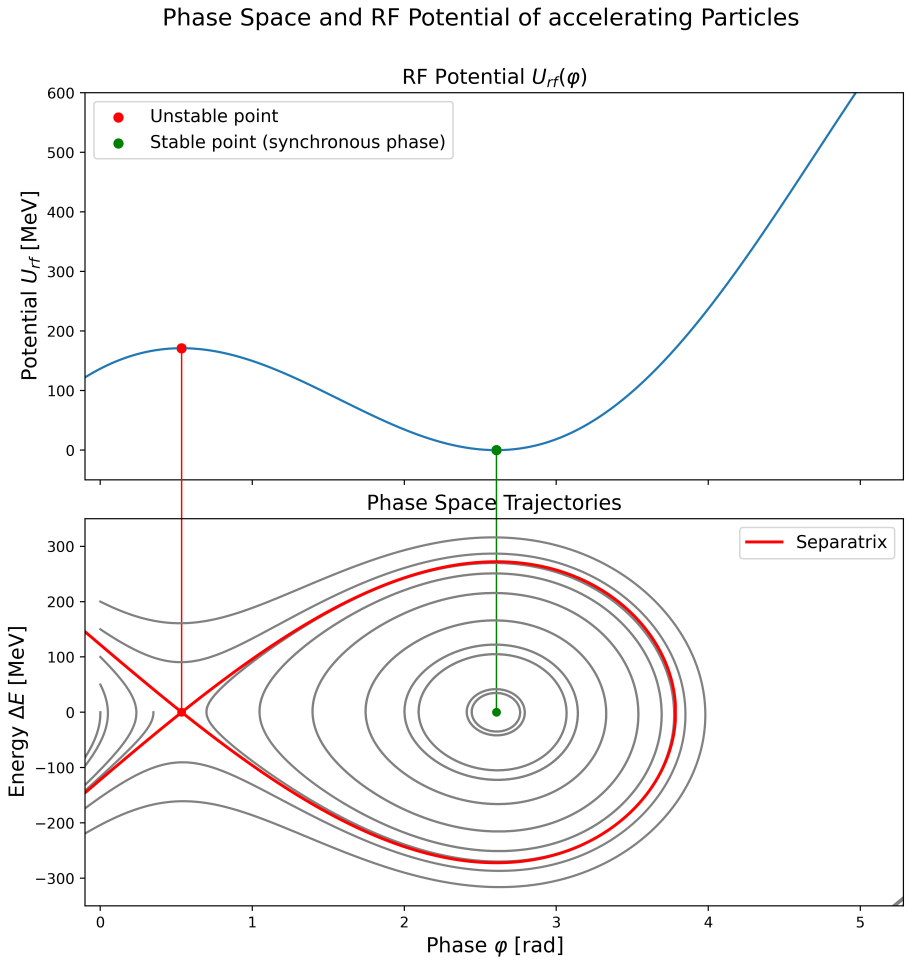

(b) The accelerating case. The area enclosed by the separatrix has shrunk due to deformations in the RF potential, displacing the maxima.

Figure 2.4.1: Two plots of the RF potential (top graph) and corresponding phase space trajectories (bottom graph) for a non-accelerating and an accelerating system.
Top graph: RF potential $U_{\mathrm{rf}}(\varphi)$ dependent on the RF phase $\varphi(\Delta t) = \omega_{\mathrm{rf}}\Delta t + \chi_{\mathrm{rf}}$.
Bottom graph: the associated phase space trajectories. The trajectories enclosed by the separatrix (red line) are stable, closed orbits, while the trajectories outside are unstable and particles there are eventually lost.

2.5. Time and Energy Distributions

Given an initial distribution of N_p particles with the same charge q in phase space, i.e. N_p sets of coordinates $(\Delta t_i, \Delta E_i)$, the distribution's evolution with time can now be determined with the tools of the previous section. In most cases, one is then interested in the projection of this phase space distribution. Projecting in either the Δt or ΔE coordinate gives the time and energy distributions $P(\Delta t), N(\Delta E)$, seen in Fig. (2.5.1).

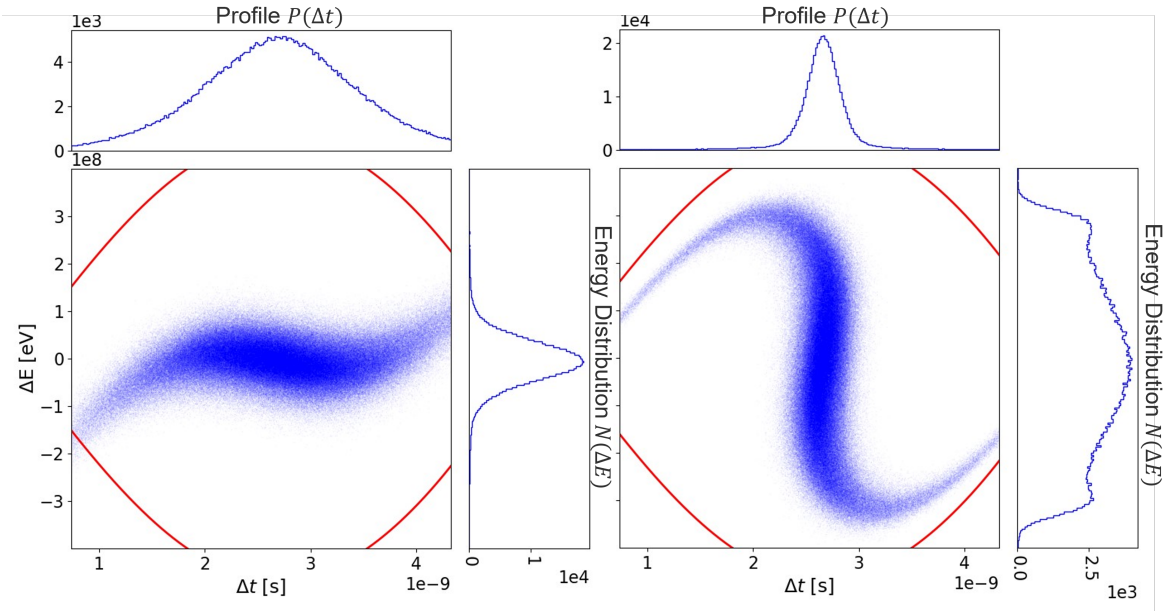

Figure 2.5.1: Phase space distributions of a bunch and their projections $P(\Delta t)$ and $N(\Delta E)$, at two different times.
On the left, the time distribution, or bunch profile, $P(\Delta t)$ is wide, extending over almost the full bucket marked by the red separatrix. Meanwhile, the energy distribution $N(\Delta E)$ is peaked.
On the right, exactly the opposite case can be seen: the energy distribution $N(\Delta E)$ is mostly flat, while the bunch profile $P(\Delta t)$ is peaked in time.

Specifically, the time distribution $P(\Delta t)$ is called the beam or bunch profile, depending on whether the whole beam or a single bunch is observed. This profile can be directly measured by observing the current flowing through a point of the beam pipe. On the other hand, the energy distribution is not commonly measured at CERN, and the infrastructure to do such measurements requires resources not available at time of writing. Therefore, numerical tools are instead used to reconstruct it.

Being able to reconstruct the energy distribution is important, as it plays a significant

role in the extraction method used for beams sent to the East [20] and North Area [21]: during the so-called slow extraction, particles with similar energies are extracted at the same time. Therefore, if one desires a constant particle stream with as little variation in number of particles extracted per second as possible, an energy distribution with a minimal slope is optimal.

Concretely, a small slope in the energy distribution can be compensated for by changing the extracted ΔE interval's size throughout the extraction process, as seen schematically in Fig. (2.5.2). However, this adjustment can only be performed gradually, and sharp peaks in the energy distribution will result in suboptimal slow extraction. Therefore, a wide energy distribution $N(\Delta E)$ with a minimal and mostly smooth gradient $N'(\Delta E)$ is desired.

Creating such a flat energy distribution with which the beam can be efficiently extracted is the main goal of this thesis, and is achieved by optimizing the manipulations performed on the beam's particle distributions.

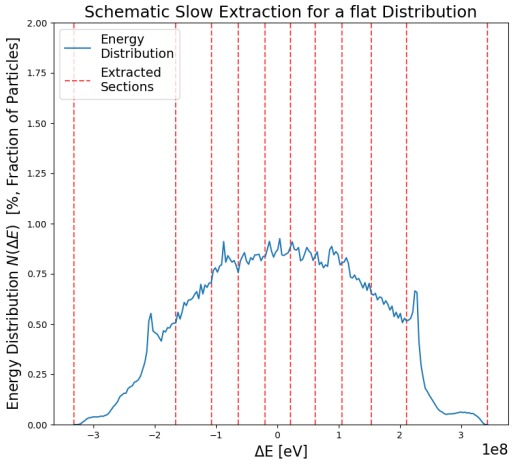

(a) Energy distribution for an extraction with low $N'(\Delta E)$. The interval sizes vary gradually over time, hence slow extraction is easier to perform.

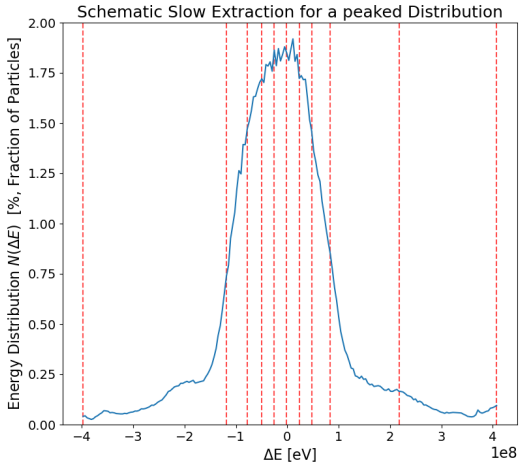

(b) Extraction with high $N'(\Delta E)$. Here, the interval sizes vary rapidly over time, meaning slow extraction would be performed suboptimally.

Figure 2.5.2: Schematic examples of slow extraction for a flatter (a) and more peaked (b) energy distribution. The intervals between 2 striped red lines represent 10 % of the total number of particles, illustrating how the ΔE interval size during slow extraction varies for a constant number of extracted particles.

2.6. RF Manipulations and Phase Jumps

Various methods for manipulating the bunch distribution exist, e.g. [22], but this thesis will concentrate on the technique of a bunch rotation by phase jump. This technique sets the RF phase to the unstable phase

$$\varphi_u := \varphi_0 - \pi$$

to stretch out the bunch and create either an energy distribution that is as flat and homogeneous as possible, or a sharply peaked profile. This is done in three steps:

1. First, the RF phase is set to the unstable phase, i.e. the phase at the separatrix' edge. For example, see the points marked in red in Figures (2.4.1a), (2.4.1b). The particle distribution will then be stretched out along the separatrix for a time τ_j, creating a distribution that is wider in phase space.

2. Afterwards, the RF is set back to the stable phase until the time τ_r. During this time, the bunch will move along the particle trajectories in the RF bucket and therefore rotate in phase space.

3. Finally, the RF is turned off at time τ_r, ideally when the energy distribution is flattest. This "freezes" the energy distribution, as (2.3.6) implies $\Delta E^{(n+1)} = \Delta E^{(n)}$ for no RF voltage and acceleration, i.e. $V_{\text{rf}} = 0, \delta E = 0$. Afterwards, the slow extraction of the bunch begins, extracting particles to the experiments over multiple seconds. Alternatively, if the phase jump in not performed to optimize (slow) extraction, $V_{\text{rf}} > 0$ may be maintained to perform further manipulations, such as a second phase jump, when the bunch reaches the desired shape in phase space.

Schematically, the process is shown in Figure (2.6.1).
As Δt and ΔE both grow exponentially for angles close to the unstable phase, the choice of τ_j must be done very finely, i.e. turn by turn. Meanwhile, the rotation back at the stable phase happens on the timescale of a synchrotron oscillation period $T_s = 2\pi/\Omega_s$, i.e. on the order of 10^2 turns, meaning this choice can be done less precisely. (See Appendix A for details on the concept of synchrotron oscillations and the synchrotron frequency Ω_s).

The goal now is to find the parameter set $S_{\mathrm{pj}} = (\tau_j, \tau_r)$, which yields the desired profile and energy distribution. For example, when a flat energy distribution is needed, a parameter set avoiding the formation of tails (i.e. the beginning of bunch "filamentation") as seen in Fig. (2.6.1d), will be preferred.

An additional complication are also collective effects, which will be covered in the next section. These are effects arising from particle interactions between themselves and the environment, and add an additional term to the equations of motion (2.3.6, 2.3.7). For phase jumps specifically, taking into account collective effects means that the unstable phase will not be exactly at $\varphi_u = \varphi_0 - \pi$, but at a slightly different position due to the RF potential maxima moving. Therefore, the jump amplitude φ_j, with $\varphi_u := \varphi_0 - \varphi_j$, is also a free parameter, and the parameter set to be optimized is $S_{\mathrm{pj}} = (\tau_j, \tau_r, \varphi_j)$. Hence, optimizing a phase jump to improve the quality of the beam is equivalent to optimizing this parameter set, based on the desired profile and energy distribution of the the beam.

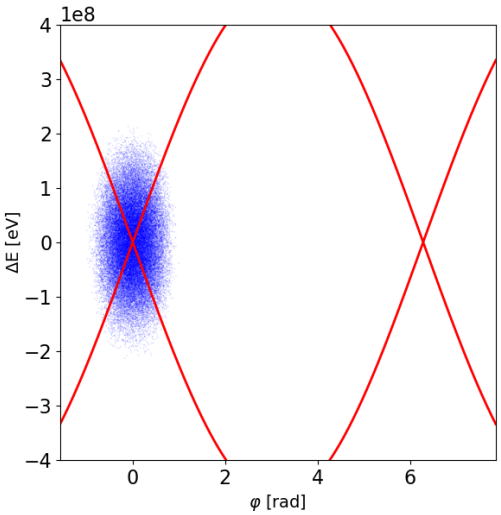

(a) Particle bunch at the unstable phase, i.e. the unstable fixed point of the Hamiltonian equations of motion.

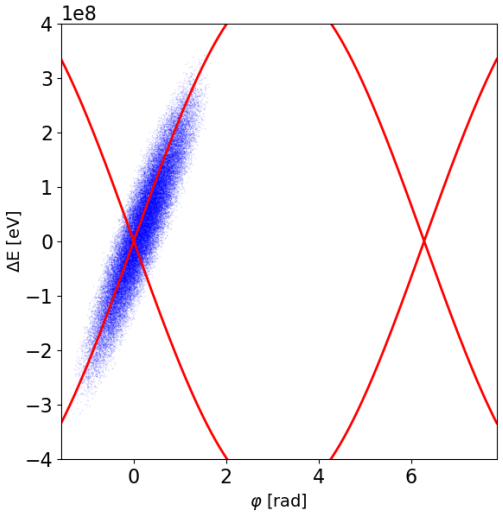

(b) Particle bunch being stretched out at the unstable fixed point for time τ_j.

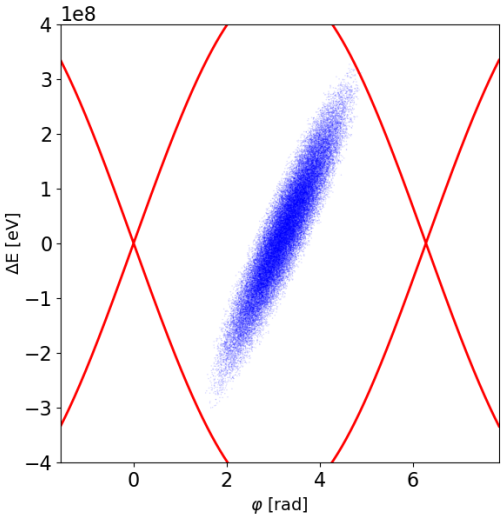

(c) The RF phase is set back onto the stable phase, putting the bunch in the middle of the bucket.

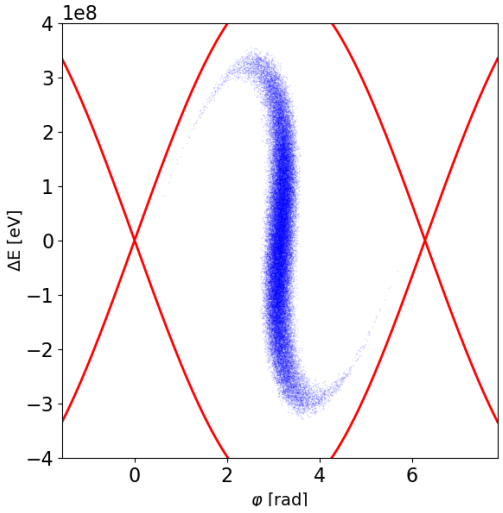

(d) The bunch being rotated in the bucket due to its shape and the equations of motion, until τ_r, when the energy distribution is flattest.

Figure 2.6.1: The phase space representation of a particle bunch during all three stages of a phase jump: The jump to the unstable phase (a) and the bunch being stretched out (b), the jump back to the synchronous phase φ_0 (c), and the corresponding rotation (d) as time advances.

2.7. Collective Effects

The electromagnetic interaction between the particles themselves, as well as with their environment, is also part of longitudinal beam dynamics and adds a term $\Delta E_{\mathrm{ind}} = qV_{\mathrm{ind}}$ to Eq. (2.3.6). V_{ind} represents the induced voltage and quantifies the additional energy gain or loss due to the interaction, meaning that the full longitudinal equations of motion become:

$$\Delta E^{(n+1)} = \Delta E^{(n)} + \sum_{k=1}^{N_{\mathrm{rf}}} qV_{\mathrm{rf},k} \sin(\omega_{\mathrm{rf},k}^{n} \Delta t^{(n)} + \chi_{\mathrm{rf},k}^{(n)}) - \delta E_0^{(n)} + qV_{\mathrm{ind}}^{(n)}, \tag{2.7.1}$$

$$\Delta t^{(n+1)} = \Delta t^{(n)} + \left(\frac{T_{\mathrm{rev},0}^{(n+1)} \eta_0^{(n+1)}}{(\beta_0^{(n+1)})^2 E_0^{(n+1)}} \right) \Delta E^{(n+1)}, \tag{2.7.2}$$

which produce a new Hamiltonian and RF Potential:

$$H(\Delta t, \Delta E) = \frac{\eta_0}{2(\beta_0)^2 E_0} \Delta E^2 + U_{\mathrm{rf}}(\Delta t), \tag{2.7.3}$$

$$U_{\mathrm{rf}}(\Delta t) = \frac{q}{T_{\mathrm{rev},0}} \sum_{k=1}^{N_{\mathrm{rf}}} \frac{V_{\mathrm{rf},k}}{\omega_{\mathrm{rf},k}} \cos(\omega_{\mathrm{rf},k} \Delta t + \chi_{\mathrm{rf},k}) + \frac{\delta E_0}{T_{\mathrm{rev},0}} \Delta t - \frac{q}{T_{\mathrm{rev},0}} \int V_{\mathrm{ind}}(\Delta t) d(\Delta t) + C_H. \tag{2.7.4}$$

This addition is significant at high intensities, affecting all aspects of beam dynamics by changing the shape of the RF potential and the position of its extrema. Importantly, this means that the previously defined synchronous phase $\varphi_0 = \arcsin(\delta E_0/(qV_{\mathrm{rf}}))$ no longer yields the stable phase. This also means that a phase jump by π no longer yields the unstable phase, which alongside other consequences of collective effects, contributes to errors in the phase jump.

To calculate these effects numerically, consider the longitudinal force that a witness particle experiences due to a source particle, as both traverse a section of the accelerator, such as an RF cavity.

Assume the particles' relative positions $\vec{r} - \vec{r}' = (x - x', y - y', z - z') =: (\Delta x, \Delta y, \Delta z)$ remain approximately constant while they traverse the section. Then, one can calculate the total energy change $\Delta E_p := qV_p(\vec{r} - \vec{r}')$ and corresponding voltage V_p the witness particle experiences after its passage: ΔE_p is given as the integral over the witnessed

Lorentz force F_z [23, Chapter 1]

$$qV_p(\vec{r}-\vec{r}') = \Delta E_p = \int_{\text{section}} F_z(\vec{r}-\vec{r}', s)\, ds =: -qq'w(\vec{r}-\vec{r}'), \tag{2.7.5}$$

with s being the particles' longitudinal centre of mass position in the section, q and q' being the witness and source particle charges, and $\vec{r}-\vec{r}'$ the distance between witness and source particle.

Given this so-called wake function $w(\vec{r}-\vec{r}')$, also referred to as the Green's function, the convolution with a general charge distribution ρ_q produces the total induced voltage:

$$V_{\text{ind}}(\vec{r}) = \int_{\mathbb{R}^3} w(\vec{r}-\vec{r}')\rho_q(\vec{r}')\, d^3\vec{r}'. \tag{2.7.6}$$

The beam in the accelerator extends significantly further in the longitudinal rather than the transversal directions (see Fig. (2.7.1)), meaning $\Delta x, \Delta y \ll \Delta z$. Therefore, the wake function can be Taylor expanded to first order around $\Delta x, \Delta y = 0$. As the RF cavity is usually transversally symmetric, meaning $w(x,y.z) = w(-x, -y,z)$, the first order term of the expansion vanishes, only leaving the part independent of $\Delta x, \Delta y$: $w(\vec{r}-\vec{r}') \approx w(z-z')$ [24].

Using $\Delta x, \Delta y \ll \Delta z$, the integration over $\mathbb{R}^3$ can be approximated as a line integral over z, yielding a simplified equation where the integration is now carried out over the one dimensional line density $\lambda(z)$ [24]:

$$V_{\text{ind}}(z) = \int_{\mathbb{R}} w(z-z')\lambda(z')dz'. \tag{2.7.7}$$

The line density λ_1 of a single bunch is usually either approximated as a Gaussian distribution, or the so-called continuous binomial distribution [25]:

$$\lambda(z) = \frac{N_p}{M}\left(1-4\left(\frac{z-z_0}{v\tau_l}\right)^2\right)^{\mu} = \frac{N_p}{M}\left(1-4\left(\frac{\Delta t}{\tau_l}\right)^2\right)^{\mu}, \tag{2.7.8}$$

with N_p being the number of particles in the bunch, M a normalization, $\Delta t = (z-z_0)/v$ the time difference relative to the synchronous particle and τ_l the full bunch length, i.e. the Δt-interval in which all particles of the bunch lie. Meanwhile, μ defines the

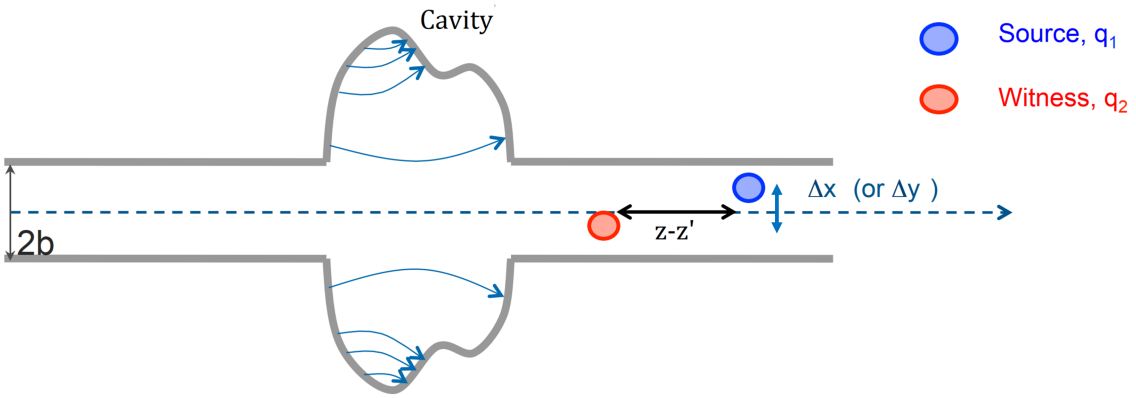

Figure 2.7.1: Schematic cavity where a witness particle (red) and electromagnetic source (blue) travel through. The source particle affects the trajectory of the witness as both travel through the cavity.
Source: adapted from [24]

.

sharpness of the bunch tails: $\mu = 1$ defines a parabolic bunch with no tails, while for $\mu \to \infty$ the distribution converges to a Gaussian distribution with infinitely long tails. While in this section a Gaussian bunch density is assumed for simplicity, real particle bunches are more accurately represented by Eq. (2.7.8), and this distribution will be used in Chapters 3 and 4. An example is given in Fig (2.7.2), with bunch parameters commonly occurring in the SPS.

To now calculate w, and thereby V_{ind}, one usually determines the system's response in frequency domain experimentally. This so-called impedance, i.e. the Fourier transform of w, is then:

$$Z(\omega) := \mathcal{F}[w(z)] = \frac{1}{c}\int_{\mathbb{R}} w(z) e^{\frac{-i\omega z}{c}}\, dz.$$

The corresponding inverse transform is:

$$w(z) := \mathcal{F}^{-1}[Z(\omega)] = \frac{1}{2\pi}\int_{\mathbb{R}} Z(\omega) e^{\frac{i\omega z}{c}}\, d\omega.$$

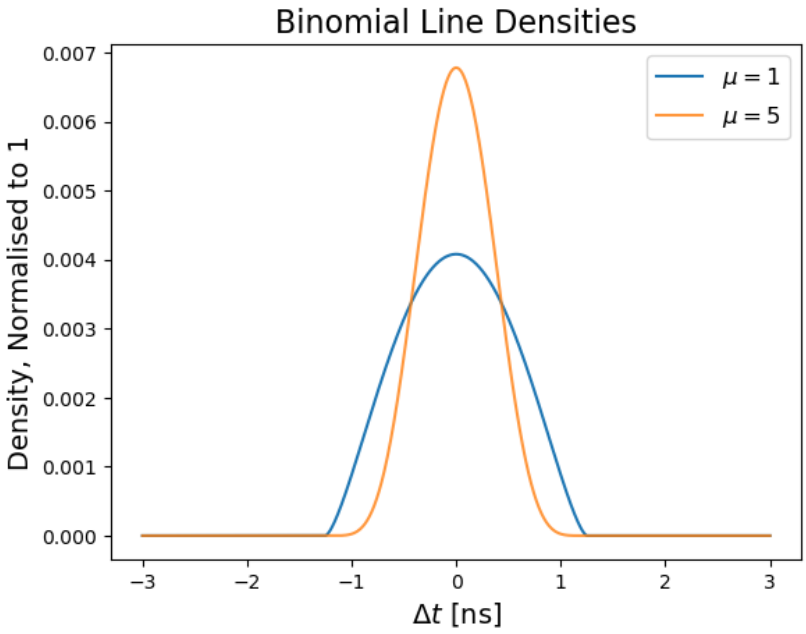

Figure 2.7.2: Binomial line densities λ for different μ, with a bunch length of $\tau_l = 2$ ns commonly occurring at the SPS. In blue, the bunch with $\mu = 1$ is parabolic, with the line density dropping off to 0 quickly and without tails, while for $\mu = 5$ the edges are smoother and the bunch becomes more similar to a Gaussian.

Therefore,

$$\begin{aligned} V_{\text{ind}}(z) &= \int_{\mathbb{R}} \frac{1}{2\pi} \int_{\mathbb{R}} Z(\omega) e^{i\omega \frac{z-z'}{c}} \lambda(z')\, d\omega\, dz' \\ &= \frac{1}{2\pi} \int_{\mathbb{R}} Z(\omega) e^{i\omega \frac{z}{c}} \int_{\mathbb{R}} \lambda(z') e^{-i\omega \frac{z'}{c}}\, dz'\, d\omega \\ &= \mathcal{F}^{-1}[Z \cdot c\mathcal{F}[\lambda]] \\ &= \mathcal{F}^{-1}[Z(\omega) \cdot c\hat{\lambda}(\omega)], \end{aligned} \tag{2.7.9}$$

where $\hat{\lambda}(\omega)$ is the Fourier transform of the line density, called the beam spectrum.

Note that the line density describes the beam across all space. In the case of circular machines, the beam passes by the same section of the accelerator at every turn, building up the induced voltage turn by turn. To take into account these multi-turn effects, one can approximate $\lambda(z)$ as periodic, with a period of the accelerator circumference:

$$\lambda(z) = \sum_{n=-\infty}^{\infty} \lambda_b(z - nC),$$

where λ_b is the line density of the beam during one turn and C is the ring circumference.

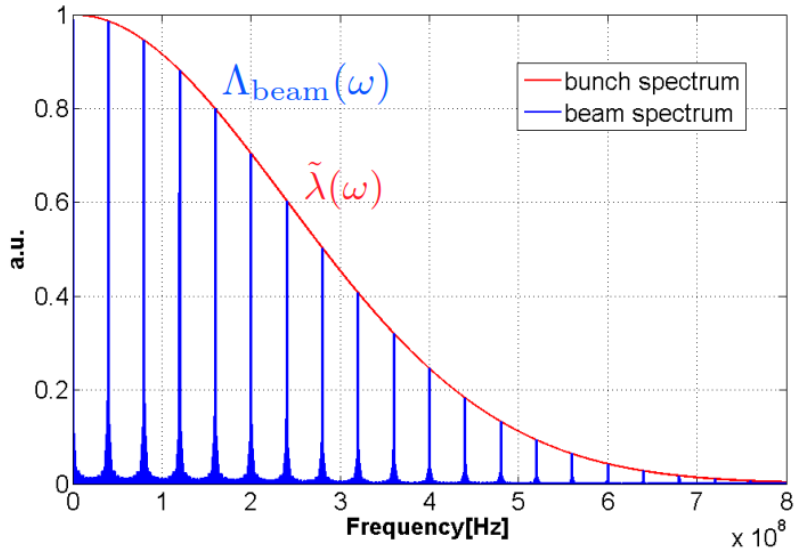

Figure 2.7.3: Schematic bunch and beam spectra, i.e. the Fourier transformed line densities of the bunch and beam. The bunch spectrum (red) envelops the beam spectrum (blue), which is a series of δ-peaks. How collective effects affect the beam is quantified by the beam spectrum, multiplied with the accelerator impedance $Z(\omega)$.
Source: adapted from [24]

.

This can also be written as

$$\lambda(z) = [\lambda_b * \sum_{n=-\infty}^{\infty} \delta(nC)](z),$$

where $*$ denotes the convolution. As

$$\mathcal{F}[\sum_{n=-\infty}^{\infty} \delta(z - nC)] = \frac{2\pi c}{C} \sum_{n=-\infty}^{\infty} \delta(z - n\frac{2\pi c}{C})$$

[26, p. 245-248], the Fourier transform then simply becomes

$$\hat{\lambda}(\omega) = \hat{\lambda}_b(\omega) \sum_{n=-\infty}^{\infty} \omega_0 \delta(\omega - n\omega_0), \tag{2.7.10}$$

with

$$\omega_0 = \frac{2\pi c}{C}. \tag{2.7.11}$$

Essentially, the beam spectrum is a series of delta peaks enveloped by the bunch spectrum, as shown in Fig. (2.7.3).

Therefore, by determining the impedance of the accelerator's components beforehand, as well as measuring the line density during a revolution turn by measuring the bunch profiles, the induced voltage is fully determined. To perform these calculations numerically, models of the impedance have been developed both for the PS [27] and SPS [28], and will be used throughout this thesis.

However, the error of these calculations and therefore the accuracy of the simulations depends on exactly how the (discrete) fast Fourier transform (FFT) is performed and how finely the data is discretized. To obtain accurate results for this thesis, a study of numerical errors and noise is performed in Appendix B.

2.8. Beam Feedback Loops

To ensure proper acceleration of the beam without losses, the particle's trajectories need to be kept within the RF bucket, i.e. the separatrix. Beam feedback loops are the tools used for this purpose. Concretely, the loops adjust the frequency of the RF system to force the beam's phase and radial position back to their desired values (see illustrations in Fig. (2.8.1)), after they are offset due to phenomena such as collective effects or misalignments of the installed magnets. This allowing stable acceleration despite commonly present operational imperfections.

There are three main feedback loop systems used in CERN's particle accelerators: the phase loop, the radial loop and the synchronization loop.
The former acts on very short timescales, on the order of revolution turns, to align the RF phase to the instantaneous synchronous phase, i.e. the actual phase of the beam φ_b. This ensures that particles are not lost from the RF bucket.
The latter two are mutually exclusive, and act on larger timescales, usually on the order of $100 - 1000$ revolution turns. Both are used to keep the beam's radial position at the desired value, e.g. in the middle of the beam pipe. This ensures the beam is not lost due to aperture limitations, i.e. due to particles colliding with the edges of the beam pipe, while minimally affecting the phase loop because these two loops work at significantly different timescales.

As stated, the phase loop acts on the timescale of revolution turns and is used to adjust the RF phase $\varphi_{\mathrm{rf}}^{(n+1)} = \omega_{\mathrm{rf}}^{(n+1)}\Delta t^{(n+1)} + \chi_{\mathrm{rf}}^{(n+1)}$ at turn $n+1$ by adjusting the RF frequency $f_{\mathrm{rf}}^{(n+1)}$. This adjustment is based on the phase deviation $\Delta\varphi^{(n)} = \varphi_b^{(n)} - \varphi_{\mathrm{rf}}^{(n)}$ between actual beam phase $\varphi_b^{(n)}$ and RF phase $\varphi_{\mathrm{rf}}^{(n)}$ at turn n. The function of the phase loop is illustrated schematically in Figure (2.8.1a). Concretely, the adjusted frequency is $f_{\mathrm{rf}}^{(n+2)} = f_{\mathrm{rf}}^{(n+1)} + \Delta f_{\mathrm{rf,PL}}^{(n)}$, with

$$\Delta f_{\mathrm{rf,PL}}^{(n)} = -G_{\mathrm{PL}} F_{\mathrm{PL}}(\Delta\varphi^{(n)}, \Delta\varphi^{(n-1)}, \dots), \tag{2.8.1}$$

where G_{PL} is the phase loop gain. It is normally chosen such that the RF phase is set to the beam phase within 1-10 revolution turns after a sudden deviation.

Additionally, the function F_{PL} is a filter applied to the measured phase deviation, usually chosen such that, in the frequency domain, it filters out low frequency components of $\mathcal{F}[\Delta\varphi]$, i.e. the components causing long-term phase shifts. This ensures that the phase loop does not try to counteract phenomena such as the synchronous phase shift due to collective effects, described in the previous section. As these phenomena change the equilibrium of the system, they would constantly re-establish themselves, which the phase loop would try to continuously counteract. This would cause a permanent and self-amplifying feedback loop, driving the RF frequency f_{rf} to deviate from the design frequency $f_{\mathrm{rf},0}$ enough for Eq. (2.2.5) not to hold, and the beam to be lost.

Even in correct operation however, f_{rf} will experience a slight offset from the design frequency over time due to the phase loop's frequency change $\Delta f_{\mathrm{rf,PL}}$. To ensure beam stability, this long-term drift must be corrected. This is the task of the radial or synchronization loop, which are used for the same purpose, but in different conditions.

The synchronization loop works by adjusting the measured RF frequency f_{rf} to the design frequency $f_{\mathrm{rf},0}$, usually calculated from the design energy E_0 and measured magnetic field B via Eq. (2.1.3)

$$f_{\mathrm{rf},0}(B, E_0) = h\omega_{\mathrm{rev},0} = h\frac{\beta_0 c}{\rho} = h\frac{qBc^2}{E_0}.$$

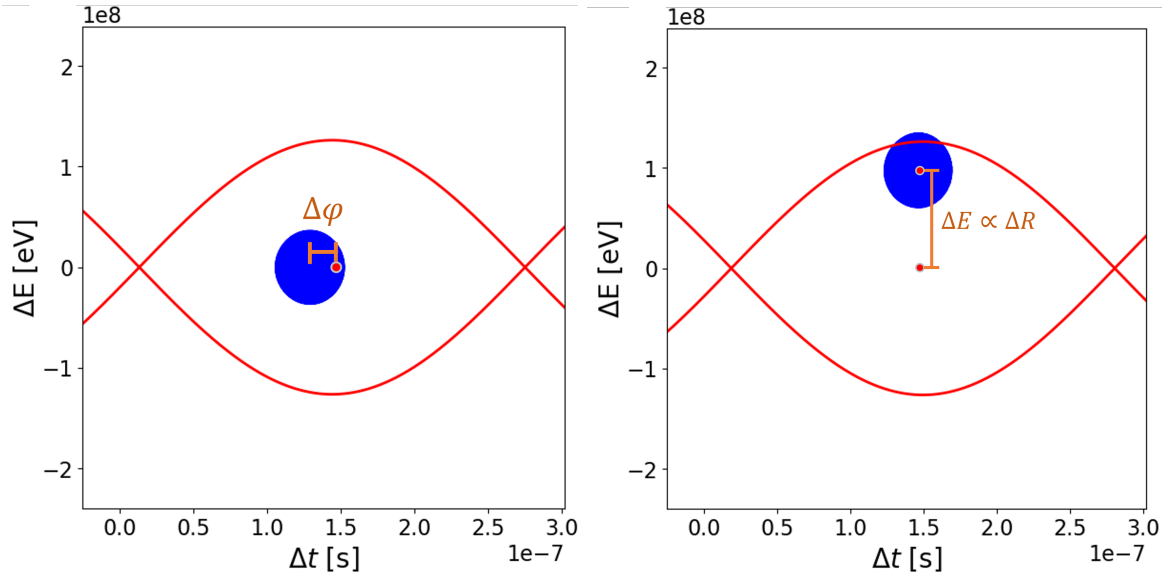

(a) A bunch whose average phase $\varphi_b = \omega_{\mathrm{rf}}\Delta t + \chi_{\mathrm{rf}}$ is offset from the centre of the bucket φ_{rf} by an offset $\Delta\varphi$. This offset will be detected by the phase loop, and corrected in 1-10 revolution turns.

(b) A bunch whose average radial position ΔR is offset from the target position, which corresponds to an offset in average ΔE from the centre of the bucket. This offset will be detected by the radial loop, and corrected in 100-1000 revolution turns.

Figure 2.8.1: Schematic illustrations of the longitudinal phase space for use cases of the phase loop (a) and radial loop (b). The synchronization loop acts analogously to the radial loop.

Therefore, based on the frequency offset $\delta f_{\mathrm{rf}}^{(n)} = f_{\mathrm{rf}}^{(n)} - f_{\mathrm{rf},0}^{(n)}$ from the design frequency, the synchronization loop adjusts the actual RF frequency $f_{\mathrm{rf}}^{(n+2)} = f_{\mathrm{rf}}^{(n+1)} + \Delta f_{\mathrm{rf,\,SL}}^{(n)}$ similarly to the phase loop:

$$\Delta f_{\mathrm{rf,\,SL}}^{(n)} = G_{\mathrm{SL}} F_{\mathrm{SL}}(\delta f_{\mathrm{rf}}^{(n)}, \delta f_{\mathrm{rf}}^{(n-1)}, \dots). \tag{2.8.2}$$

The gain G_{SL} is set such that the synchronization loop acts on timescales of $100 - 1000$ turns. The function F_{SL} also filters out high-frequency components of the offset $\mathcal{F}[\delta f_{\mathrm{rf}}^{(n)}]$, such as the frequency changes of the fast-acting phase loop. This ensures that these loops do not counteract each other, while slowly adjusting f_{rf} back to $f_{\mathrm{rf},0}$.

However, a problem arises during the so-called transition crossing, where the slippage factor $\eta(t)$ changes sign. When $\eta(t) \approx 0$, a small frequency offset causes large momentum offsets due to Eq. (2.3.3): $\Delta p = -\Delta\omega_{\mathrm{rev}}/(\eta\omega_{\mathrm{rev},0}p_0)$. Therefore, small measurement errors, e.g. errors in the measured magnetic field B, have a large impact:

They cause the calculated design frequency $f_{\mathrm{rf},0}(B)$ to be offset from the actual, physically optimal frequency, which induces a large momentum offset [29]. This impact is large enough that near transition, the beam will be lost to aperture limitations even due to expected measurement errors occurring in normal operation. Hence, if the beam being accelerated crosses transition, the accelerator used to do this should use a different beam feedback loop to re-establish the design frequency during acceleration.

The radial loop is commonly used for this purpose, as the radial offset ΔR of the beam from the middle of the beam pipe is related to the frequency offset by [19, Eq. (2.86)]

$$\frac{\Delta R}{\rho} = \frac{\gamma_0^2}{\gamma_{\mathrm{tr}}^2 - \gamma_0^2} \frac{\delta f_{\mathrm{rf}}}{f_{\mathrm{rf},0}}, \tag{2.8.3}$$

where $\gamma_t^2 = \frac{\gamma_0^2}{\eta_0 \gamma_0^2 - 1}$ is the Lorentz factor at transition.

Therefore, the radial loop acts based on the measured radial offset $\Delta R^{(n)}$ to bring f_{rf} back to $f_{\mathrm{rf},0}$, as illustrated in Fig. (2.8.1b). It is particularly sensitive at transition, where $\gamma_0 \approx \gamma_t$, and a small frequency offset δf_{rf} will immediately result in a large radial offset ΔR. As before, the frequency adjustment is performed as follows:

$$\Delta f_{\mathrm{rf,\,RL}}^{(n)} = G_{\mathrm{RL}} F_{\mathrm{RL}}(\Delta R^{(n)}, \Delta R^{(n-1)}, \dots). \tag{2.8.4}$$

And analogously to the synchronization loop, the radial loop acts on timescales of $100 - 1000$ turns, with F_{RL} filtering out high-frequency components in $\mathcal{F}[\Delta R]$, as to not counteract the phase loop.

3. Optimizations of fixed-target beams at the SPS

This chapter applies the knowledge from the previous chapter to optimize the phase jump currently used in the SPS Fixed Target Proton (SFTPRO) beam cycle. Here, a cycle is the sequence consisting of particle injection into the accelerator, the acceleration of these particles, their extraction, and finally the preparation for the next injection. The SFTPRO cycle is used for beams exploited by the North Area experiments, where a flat energy distribution improves the process of slow extraction [21], which in turn improves experimental data quality.

After presenting further details on the cycle and slow extraction, beam profiles for settings at and around the current operational phase jump settings $S^c_{\mathrm{pj}} = (\tau^c_j, \tau^c_r, \phi^c_j)$ are measured. These are then used to numerically reconstruct the corresponding energy distributions. Afterwards, an algorithm is developed and used to quantify the quality of the reconstructed distributions, which allows direct comparison between the results of various sets of settings S_{pj}. After the errors of this methodology are evaluated, the algorithm is used to define optimal settings S^o_{pj}. These are tested in operation by comparing numerically reconstructed distributions to those inferred from measuring the particles extracted at slow extraction, allowing a final conclusion.

3.1. General Information

The Machine Development (MD) beam cycle used for measurements mimics the SFTPRO cycle currently in operation. It takes two injections from the PS, where the second injection follows 1.2 seconds after the initial one. After this, the beam is accelerated from 14 GeV to 400 GeV over the course of 3 seconds. The phase jump is performed immediately after reaching the desired energy at the so-called “flat top” at 4.26 s, where no more acceleration takes place and the energy remains constant.

After the phase jump, the protons are debunched by shutting the RF off fully, i.e. $V_{\mathrm{rf}} = 0$. This means that the protons spread out longitudinally across the length of the beam pipe, after which slow extraction begins and the beam is sent to the North Area. Note that the debunching process has negligible impact on the energy

distribution, i.e. the energy distribution at the end of the phase jump is assumed to be equal to the one at the start of slow extraction.
As elaborated on in Sections 2.5 and 2.6, the phase jump itself is performed to widen the energy distribution $N(\Delta E)$ and reduce its slope $dN(\Delta E)/d(\Delta E)$. This makes extracting a constant number of particles per turn easier, improving experimental results.

Figure (3.1.1) depicts the beam momentum's evolution, i.e. the programmed momentum $p_0 \overset{p_0 c \gg mc^2}{\approx} E/c$, starting from the first injection in the SFTPRO cycle. Given this program, the beam intensity, and the accelerators structural parameters, all relevant parameters for beam dynamics at the flat top are calculated in Table (3.1.1).

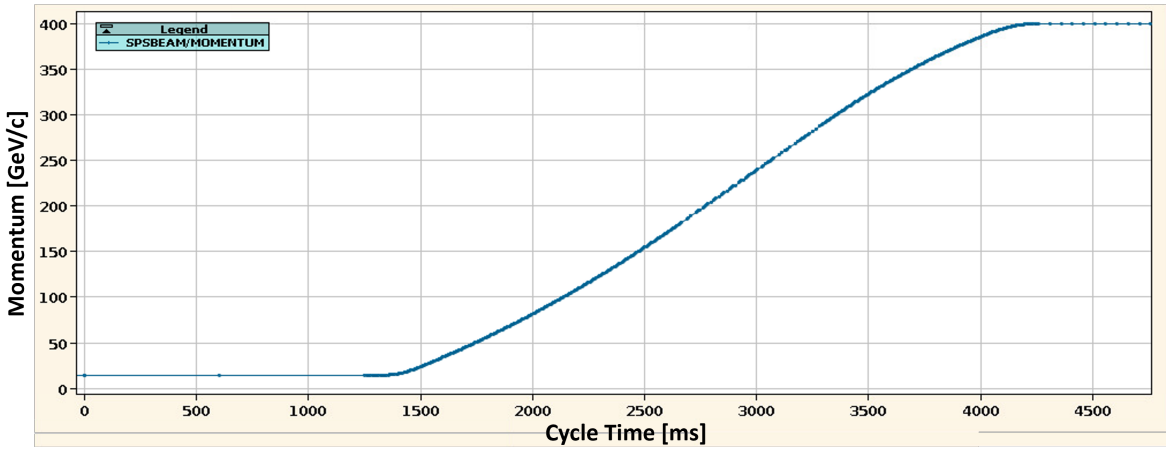

Figure 3.1.1: STFPRO momentum program, determining the beam's momentum for the entire duration of the STFPRO cycle. Acceleration begins at 1250 ms cycle time, then the flat top of constant momentum is reached at 4260 ms, after which the phase jump occurs, followed by slow extraction.
Taken on 21.06.2023.

MD Cycle Flat Top Parameters	
Parameter	Value
Reference energy E_0	400 GeV
Relativistic beta β_0	0.9999973
Reference momentum p_0	400 GeV/c
Intensity I	$4.5 \cdot 10^9$ protons per bunch
Circumference C	6911.5 m
Bending radius ρ	741.3 m
Slippage parameter η_0	0.00185
Revolution time T_{rev}	23.0545 μs
Synchrotron period T_s	$\approx 200 \cdot T_{\text{rev}}$
Harmonic number h	4620
Bucket length T_{rf}	4.9902 ns
Total 200 MHz voltage $V_{\text{rf,200}}$	6.974 MeV
Total 800 MHz voltage $V_{\text{rf,800}}$	0.6974 MeV

Table 3.1.1: MD cycle parameters used for measurements at the flat top, 4260 ms after injection. These parameters, except for T_s, are accurate to within at least six significant figures, and therefore more accurate than shown, hence no error is displayed.

3.2. Current and Examined Settings

Before the numerical optimizations presented herein, the optimal settings for the phase jump were determined manually while setting up the SPS for operation at the beginning of each year. Though the energy distribution cannot currently be measured directly due to the infrastructure necessary not being available, the shape of the beam profile is directly correlated to the shape of the energy distribution, as can be seen in Fig. (2.5.1): for a bunch after the phase jump, a strongly peaked profile corresponds to a flat energy distribution. Therefore, to optimize the phase jump, the settings yielding the highest profile peak for 2023 were manually determined to be the following:

The system of RF cavities is temporarily set to the unstable phase by a phase jump of $\phi_j^c = \pi$. This is maintained for $\tau_j^c = 26$ turns, after which the RF remains turned on for 80 turns until $\tau_r^c = 106$ turns. Thus, the operational settings are

$S^c_{\mathrm{pj}} = (\tau^c_j = 26, \tau^c_r = 106, \phi^c_j = \pi)$.

Theoretically however, a peaked profile does not have to correspond to the energy distribution with the largest width or the lowest gradient. Additionally, since the bunch rotates in longitudinal phase space (so called quadrupolar oscillations), there are multiple times at which the profile is peaked, as visible in Fig. (3.2.1). Concretely, the profile is peaked around half-integers of the synchrotron period T_s i.e. at $\tau_r \approx \frac{1}{2} \cdot T_s, T_s, \frac{3}{2} \cdot T_s, ...$ Physically, this is when the stretched out bunch has rotated by 180 degrees in phase space, meaning that it has rotated from one peaked state to the next. However, which of these profile peaks yields an optimal energy distribution is not immediately evident. Therefore, additional analysis is necessary to choose τ_r, but also τ_j, optimally.

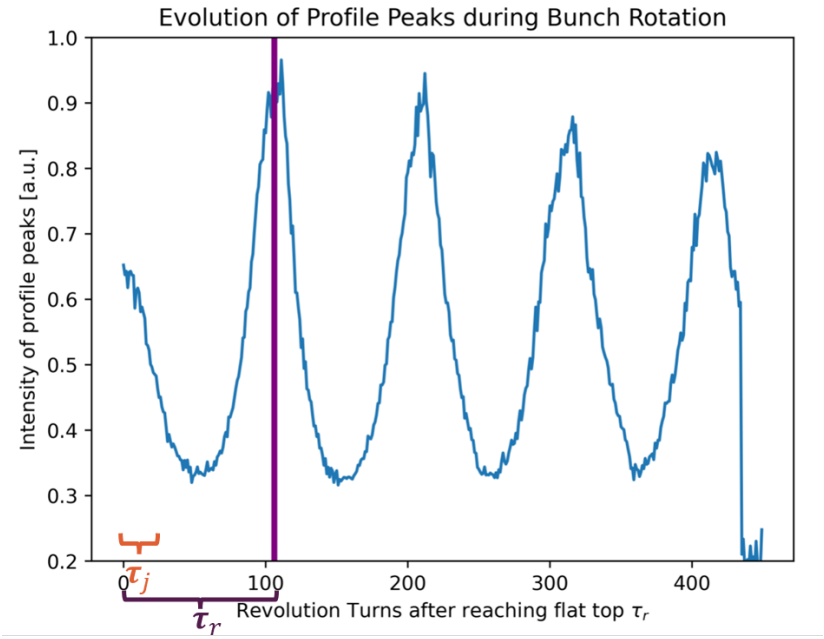

Figure 3.2.1: Profile peak intensities during a bunch rotation by phase jump for different τ_r for the MD cycle outlined in Table (3.1.1). The operational values for the phase jump start time τ^c_j and rotation duration τ^c_r are shown in orange and purple, respectively.

For this analysis, beam profiles were acquired for a duration of 450 turns after reaching the flat top, with phase jump durations of $\tau_j \in \{20, 22, 24, 26, 28, 30\}$ turns. The profiles were used to reconstruct the energy distributions for three intervals of $\tau_r \in J_{0.5}, J_1, J_{1.5}$. Here, $J_{0.5} = [75, 140]$ turns, $J_1 = [200, 250]$ turns and $J_{1.5} = [295, 345]$ turns correspond to the three peaks at $\tau_r \approx \frac{1}{2} \cdot T_s, T_s, \frac{3}{2} \cdot T_s$. To perform these measurements, the beam

was not extracted after τ_r, and instead sent to the beam dump after the observed 450 turns. This was done as RF needed to remain turned on to obtain the full measurements, while slow extraction necessitates $V_{\mathrm{rf}} = 0$ after τ_r, i.e. when particle extraction begins.

Meanwhile, the phase jump amplitude ϕ_j remained at $\phi_j^c = \pi$, as an offset in phase jump amplitude would result in an asymmetric bunch, amplifying undesired peaks in the energy distribution. This was confirmed by studying BLonD simulations for $\phi_j \in [0.8\pi, \pi]$. Therefore, $\phi_j = \pi$ will be used hereafter, and phase jump settings will be denoted as $S_{\mathrm{pj}} = (\tau_j, \tau_r, \phi_j = \pi) = (\tau_j, \tau_r)$, omitting ϕ_j.

3.3. Reconstruction and Analysis of Energy Distributions

The energy distributions were reconstructed from the measured profiles by use of longitudinal phase space tomography (see Appendix C), with tracking data supplied by BLonD simulations. This use of BLonD made it possible to take into account the phase jump itself, as well as beam feedback loops and collective effects via the corresponding feedback and impedance models.
Concretely, using the measured profiles and tracking data, reconstructions were performed over $T_{\mathrm{rec}} = 75$ revolution turns. All 6 separate reconstructions were then combined to span the full 450 turns for each measurement. $T_{\mathrm{rec}} \approx \frac{3}{8} \cdot T_s$ was chosen to be low compared to $T_s \approx 200$ turns, as the non-equilibrium dynamics during the phase jump result in significant errors if tomography is performed over a larger time span.

The BLonD simulations producing tracking data were initialized with a homogeneous particle distribution, and included the phase jump for all values of τ_j. They were performed with 1 bunch periodically repeated throughout the accelerator ring, simulating a full ring of $h = 4620$ bunches. The physical parameters used for the simulation are outlined in Table (3.1.1). Numerical parameters were determined in line with the noise analysis in Table (B.2.1), using $N_p = 7 \cdot 10^5$ macroparticles and $N_{sb} = 2000$ slices per bucket to compromise between obtaining sufficiently accurate results and low computer memory requirements. For further details, see Appendix B.

As the resulting energy distributions are never perfectly flat, and a certain slope in the distribution can be accounted for during slow extraction, an algorithm to evaluate a distribution's quality based on quantifiable criteria is used. The algorithm is specifically designed to analyse distributions with shapes near the ones expected during the bunch rotation, i.e. shapes which range from approximately rectangular to Gaussian. For this purpose, the algorithm performs the following steps.

1. First, the reconstructed energy distribution $N(\Delta E)$ is filtered based on a maximum gradient threshold, only selecting points below this threshold, and above a minimum value of the distribution itself. All other points are filtered out, creating a filtered distribution $\tilde{N}(\Delta E)$. This filters noise at points where the distribution is approximately 0, and models the fact that a small enough gradient can be accounted for in operation.

2. Second, the filtered distribution $\tilde{N}(\Delta E)$ is evaluated based on two figures of merit: width and height. The width is defined as $d = \Delta E_{\max} - \Delta E_{\min}$, where $\Delta E_{\max}$ and $\Delta E_{\min}$ are the ΔE values at the right and left edges of $\tilde{N}(\Delta E)$ respectively. The height is defined similarly as a difference between minimal and maximal values of the distribution, $h = \tilde{N}(\Delta E)_{\max} - \tilde{N}(\Delta E)_{\min}$. An example of this evaluation is shown in Fig. (3.3.1).

3. Finally, the distributions are compared based on their height and width values. For this purpose, a quality function is defined based on a weighted sum of normalized figures of merit,

$$Q(d,h,g_d,g_h) = \bar{d}g_d + \bar{h}g_h, \tag{3.3.1}$$

where $g_d > 0$ and $g_h < 0$, weighing height negatively and width positively. $\bar{d} = d_0/d_{0,\max}$ with $d_0 = (d - d_{\min})$, and $\bar{h} = h_0/h_{0,\max}$ with $h_0 = (h - h_{\min})$ are normalized such that $\bar{h}, \bar{d} \in [0, 1]$ by subtracting the minimal value of h or d in the set of all distributions which are being evaluated, and then dividing by the maximal calculated value. As such, Q is a relative quantity, only valid to compare between distributions as long as the total set of evaluated distributions stays the same. The distribution for which Q is maximal is then chosen as the optimal distribution of each set, where separate sets of distributions are considered for each value of τ_j and each τ_r-interval outlined in Section 3.2.

Concretely, the minimal distribution value chosen for this analysis was 0.2 % of the total number of macroparticles, as this filtered numerical noise from the tomographic reconstructions effectively. The gradient threshold was 0.95 %/(10^8 eV), chosen to be approximately 1.5 times the gradient threshold needed to accurately evaluate the energy distribution at S^c_{pj}. The weights were $g_d = 0.75$ and $g_h = -0.5$, valuing width over height. This was done, as h is partially parametrized by the gradient, which already influences the evaluation through the maximum gradient threshold.

Finally, note that the reconstructed energy distribution $N(\Delta E)$ is a probability density, and therefore normalized such that

$$\sum_{i=1}^{M} N(\Delta E_i) = 1, \tag{3.3.2}$$

where M is the amount of discrete ΔE values the distribution is evaluated at.

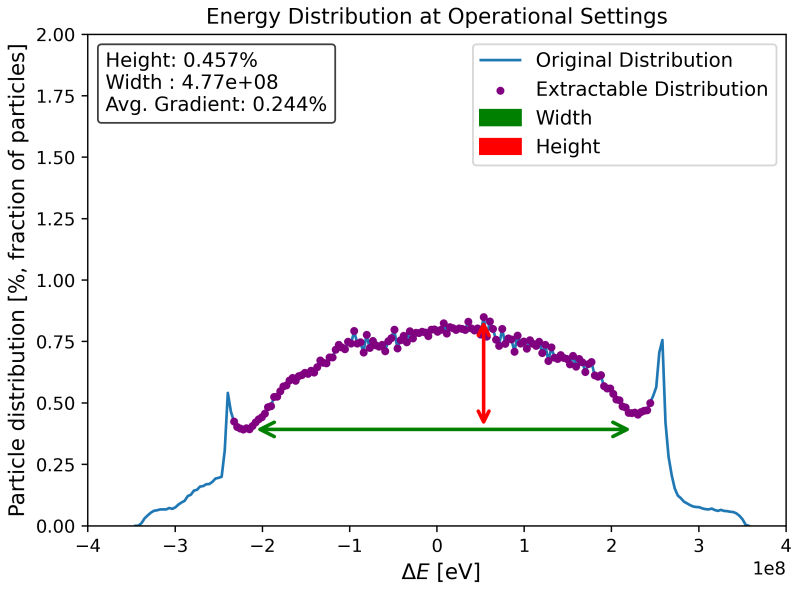

Figure 3.3.1: Example of an energy distribution evaluation near the current phase jump setup S^c_{pj}.
The light blue line is the reconstructed distribution, while the purple dots indicate the filtered distribution $\tilde{N}(\Delta E)$.
The height h and width d are marked with red and green arrows, respectively. Their values, alongside the average gradient of $\tilde{N}(\Delta E)$, are listed at the top left.

3.4. Reconstruction Accuracy

Before using this analysis method on measured data, the errors occurring due to the tomographic reconstruction should be mentioned. They are significant, as tomography is performed while the system is out of equilibrium after the phase jump. Figure (3.4.1) shows the average, normalized difference between measured profiles $P(X[i])$ and reconstructed ones $\overline{P}(X[i])$

$$\epsilon = \frac{1}{\max\limits_{1\leq i\leq L}\{P(X[i])\}}\frac{1}{L}\sum_{i=1}^{L}|\Delta P(X[i])|,$$

where $\Delta P(X[i]) = P(X[i]) - \overline{P}(X[i])$ is the profile difference and $X[i]$ are the L discrete Δt bins the profile is measured and evaluated at (for further detail, see Appendix C).

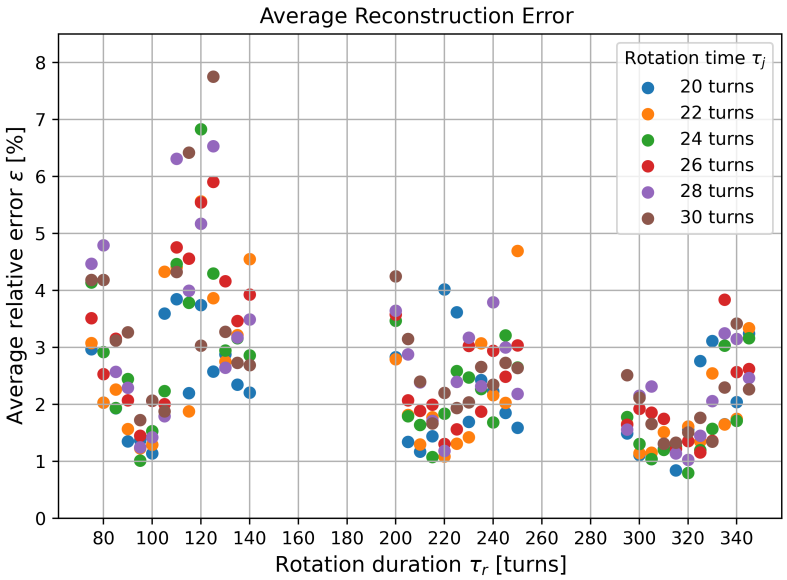

Figure 3.4.1: Tomographic error ϵ for different values of τ_j and τ_r. The different colours represent different values of τ_j, while τ_r is used as the x-axis. The error is acceptable overall, but particularly large for $\tau_r \in [110,125]$.

The errors at $\tau_r \in [110,125]$ stand out, with errors above 5 % and the maximum error of 7.75 % appearing in that interval. Outside this range, the tomographic error lies below 5 %, with no significant dependence on τ_j. Overall, ϵ also trends down as τ_j increases, due to the bunch slowly filamenting (e.g. Fig. (2.6.1d)) and returning to equilibrium as time passes. Analysing the error in more detail, Fig. (3.4.2) shows the deviation between measured and reconstructed profiles for $\tau_r \in [110,125]$.

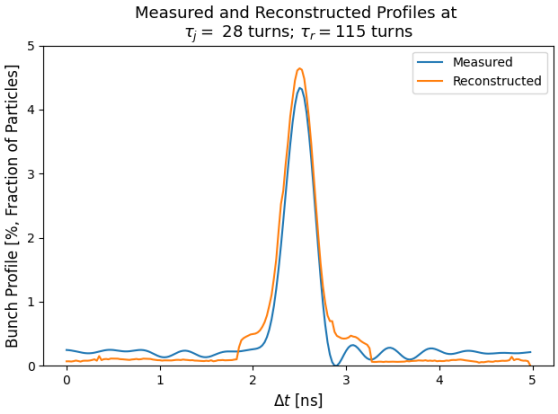

(a) $\tau_r = 115$ turns. The reconstruction has minimal errors, with a notable deviation at the peak's edges.

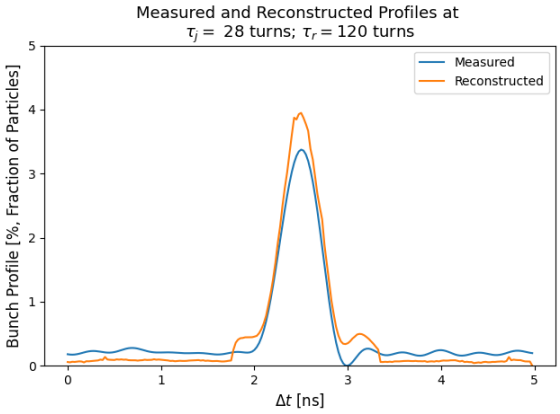

(b) $\tau_r = 120$ turns. The reconstruction remains mostly accurate, with deviations at the peak's middle and the edges.

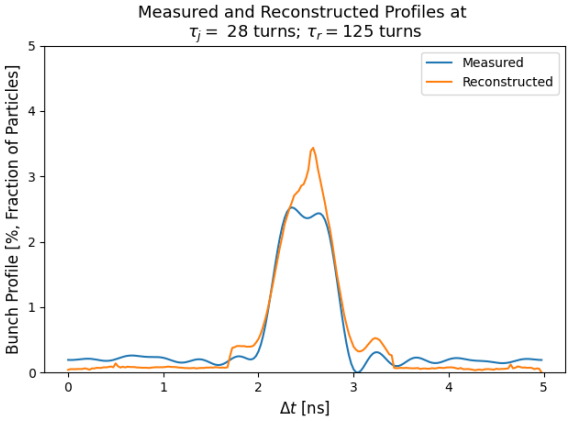

(c) $\tau_r = 125$ turns. The reconstruction struggles to follow the rapid change of the measured profile, which increases already present errors.

Figure 3.4.2: Measured (blue) and reconstructed (orange) profiles for $\tau_r = 115, 120, 125$ turns at $\tau_j = 28$ turns, where the error is maximal.

The reconstruction has difficulties following the rapid change from a peaked to a flatter profile, and adjusts to the change only slowly, causing the high error at lower rotation times. For higher values of τ_r, this error is less pronounced due to the transition from peaked to flat profile being slower, caused by the tails of the bunch being more pronounced as filamentation increases.

Additionally, the reconstructed profiles all have bumps at approximately $\Delta t = 2$ ns and $\Delta t = 3$ ns, when the measured profiles drop off to almost 0. This trend appears among most reconstructions, meaning the reconstructions tend to exaggerate profile

edge peaks. This trend of exaggerated profile edge peaks ripples through to the energy distributions shown in the following sections, causing notable deviations with respect to the observed, actual energy distributions of the beam.

Summarizing, the error lies below 5 % for $\tau_r \notin [110,125]$, which shows a decent, but faulty reconstruction due to the nonequilibrium dynamics after the phase jump, with possible exaggeration of the profile edge peaks. The profiles at $\tau_r \in [110,125]$ should however be viewed with additional scrutiny, as the error becomes significantly larger: the reconstructed profile lags behind the measured one, which can reflect a similar delay in the reconstructed energy distributions.

3.5. Results

To obtain an overview over the effects of both scanned parameters τ_j and τ_r, they are first evaluated separately by studying how the figures of merit h and d change. Concluding this analysis, an optimal parameter set $S^o_{\mathrm{pj}} = (\tau^o_j, \tau^o_r)$ is suggested based on those findings, and evaluated by comparing the reconstructed energy distributions at S^c_{pj} and S^o_{pj}.

3.5.1. Rotation Duration τ_j

To gain an initial understanding of the effect changing τ_r has, Fig. (3.5.1) shows distributions determined to be optimal via the algorithm outlined in Section 3.3. In the figure, τ_r is evaluated in the intervals $J_{0.5} = [75, 140]$ turns, $J_1 = [200, 250]$ turns and $J_{1.5} = [295, 345]$ turns. Meanwhile, the current value of $\tau_j = 26$ turns is fixed for all three distributions.

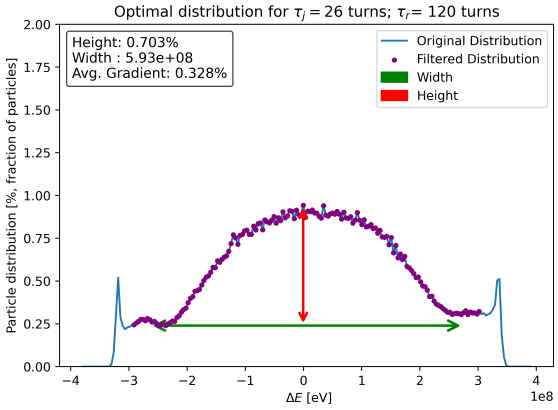

(a) Optimal distribution for $\tau_r \in J_{0.5}$. It is the widest, but has significant spikes at the edges.

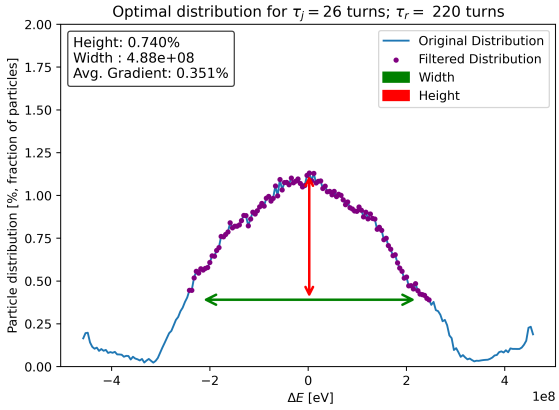

(b) Optimal distribution for $\tau_r \in J_1$. It is less wide than in (a), but has no edge spikes.

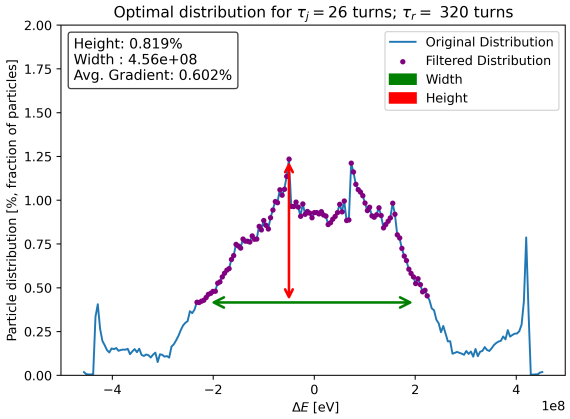

(c) Optimal distribution for $\tau_r \in J_{1.5}$. The distribution starts to become noisy and chaotic in the middle.

Figure 3.5.1: Tomographically reconstructed distributions, determined to be optimal via the algorithm in Section 3.3, for τ_r in the intervals $J_{0.5} = [75, 140]$, $J_1 = [200, 250]$ and $J_{1.5} = [295, 345]$. $\tau_j = 26$ turns is fixed.

As one can see, the distribution for $\tau_r \in J_{0.5}$, i.e. for $\tau_r \approx 0.5 \cdot T_s$, is widest and has the smallest average gradient. However, it also has significant spikes at the energy distribution edges, which would cause difficulties during slow extraction: the spikes would cause a rapid change in energy distribution, making the adjustments discussed in Section 2.5 difficult. Nonetheless, these spikes might be exaggerated compared to the actual distribution, being produced as reconstruction artefacts discussed in Section 3.4. Therefore, these settings remain promising.

As τ_r increases to around T_s, the distribution becomes less wide and higher, which is reflected in an increased average gradient. Overall, this is a worse result according to

the defined figures of merit h and d. However, the peaks at the edges also vanish. This might make it preferable over the distribution in Fig. (3.5.1a), if the peaks there are real and not an artefact of the reconstruction.

For $\tau_r \in J_{1.5}$, the distribution takes on a more erratic shape, as the bunch filaments and the resulting tails in phase space contribute noticeably to the distribution's shape. The spikes at the middle of the distribution are most likely due to these tails, while the spikes on the edges are most likely artefacts, as one would not expect them to be steeper than in Fig. (3.5.1a).

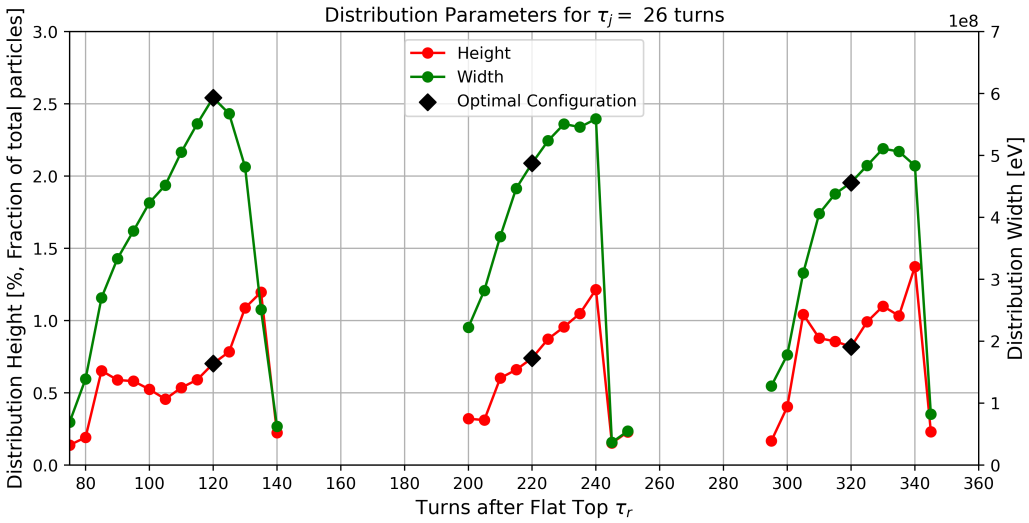

Figure 3.5.2: Widths $d(\tau_r)$ and heights $h(\tau_r)$ of the beam's energy distribution at extraction for varying values of τ_r and fixed $\tau_j = 26$. The optimal distributions in the intervals $J_{0.5}, J_1, J_{1.5}$ are marked with black diamonds.

However, these are hand-picked examples and a more general view is needed to find a global optimum. To obtain this general overview, the heights $h(\tau_r)$ and widths $d(\tau_r)$ of each distribution can be evaluated and displayed as functions of τ_r. This is done in Fig. (3.5.2), which confirms earlier observations: the widths trend down while the heights trend up as τ_r increases, and the distributions with maximal width d and minimal height h lie at $\tau_r \in J_{0.5}$. Concretely, the optimal and widest distribution appears at $\tau_r = 120$ turns, and was already shown in Fig. (3.5.1a).

3.5.2. Phase Jump Duration τ_j

The analysis from the previous subsection can now be extended to a scan of τ_j to observe its effects on the figures of merit. The results of this scan are shown in Fig. (3.5.3) for $\tau_j = 20, 26, 30$ turns. Increased widths and reduced heights are visible with increasing τ_j, most strongly present in the $\tau_r \in J_1$ interval.

For $\tau_j = 30$ turns, the maximal width in the $\tau_r \in J_1$ interval at $\tau_r = 245$ turns even exceeds the maximal width in the $\tau_r \in J_{0.5}$ interval at $\tau_r = 120$ turns. However, similarly to the examples before, the height at $\tau_r = 245$ turns is significantly higher than at $\tau_r = 120$ turns, and therefore the choice of $\tau_r = 120$ turns is still preferable.

Overall, increasing τ_j to 30 turns is preferable for any value of τ_r. At the preferred value of $\tau_j = 30$ turns, $\tau_r = 120$ turns appears optimal in terms of d and h. Therefore, the optimal settings based on this analysis are $S^o_{\mathrm{pj}} = (\tau^o_j = 30, \tau^o_r = 120)$.

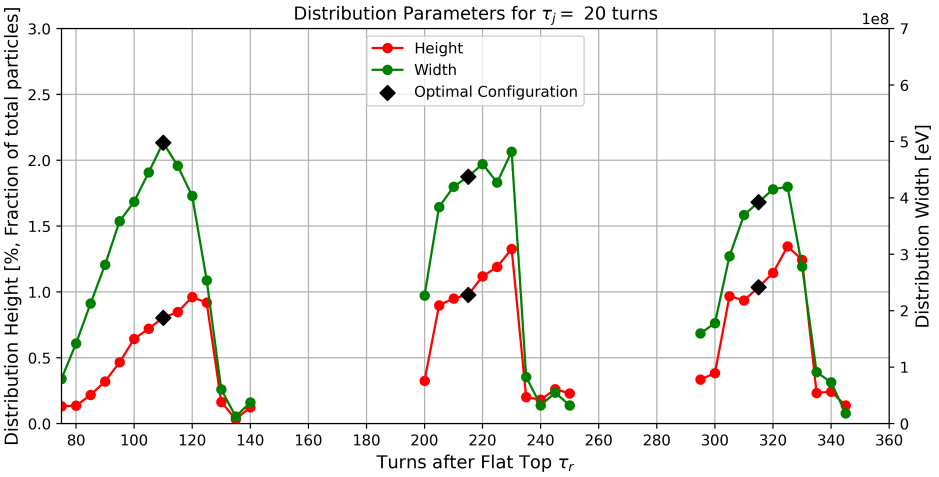

(a) Figures of merit for fixed $\tau_j = 20$ turns.

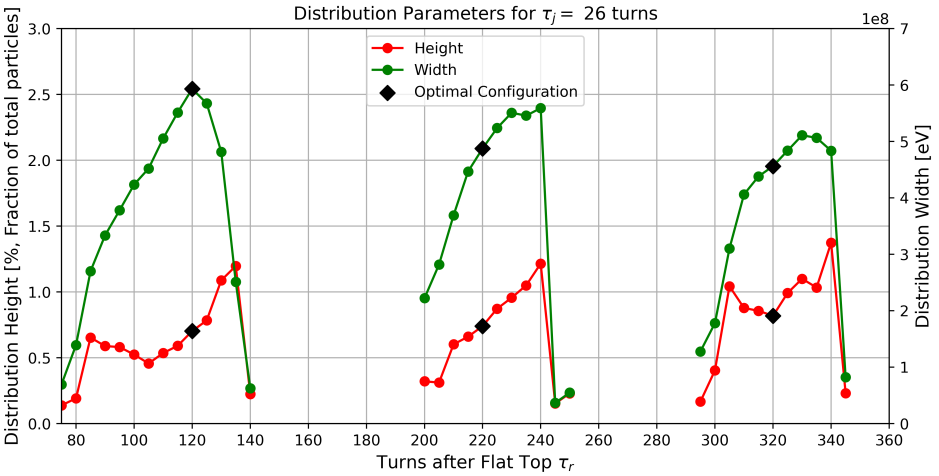

(b) Figures of merit for fixed $\tau_j = 26$ turns.

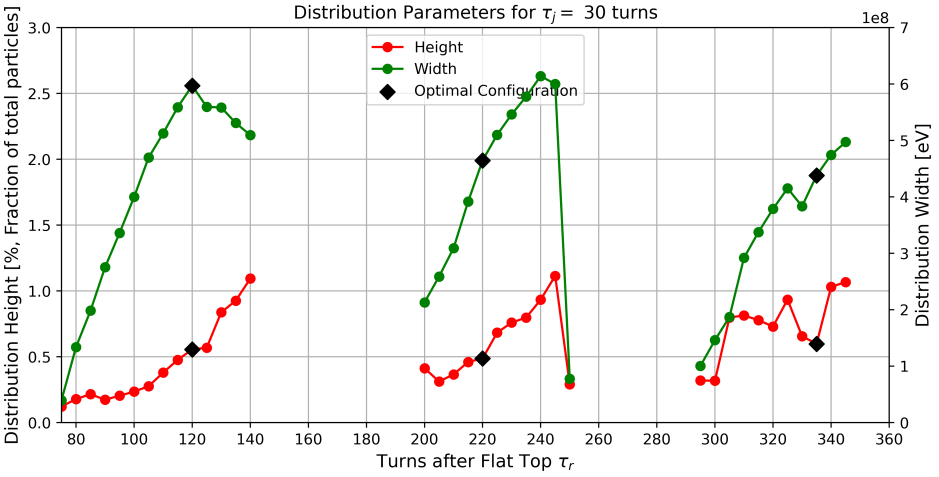

(c) Figures of merit for fixed $\tau_j = 30$ turns.

Figure 3.5.3: Widths $d(\tau_r)$ and heights $h(\tau_r)$ of the beam's energy distribution at extraction for fixed $\tau_j = 20, 26, 30$ turns and varying τ_r, with optimal distributions being marked with black diamonds for each τ_r interval. The distributions tend to have lower widths and larger heights with increasing τ_j.

3.5.3. Current and Suggested Settings

Figure (3.5.4) compares the reconstructions at the determined optimal settings $S^o_{\mathrm{pj}} = (30, 120)$ with the reconstruction at $S_{\mathrm{pj}} = (26, 105)$, closest to the current operational settings at time of writing, $S^c_{\mathrm{pj}} = (26, 106)$.

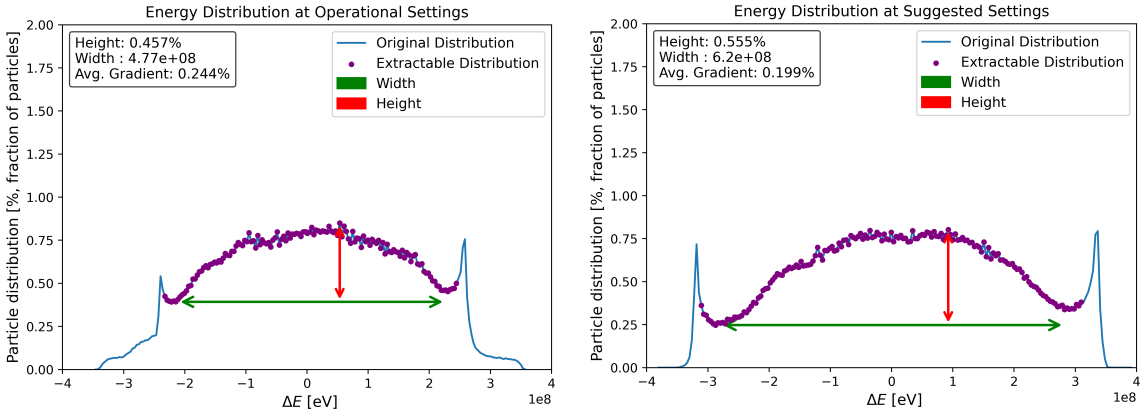

(a) Distribution at close to current settings $S_{\mathrm{pj}} = (26, 105)$.

(b) Distribution at suggested settings $S^o_{\mathrm{pj}} = (30, 120)$.

Figure 3.5.4: Comparison between the energy distribution at $S_{\mathrm{pj}} = (26, 105)$, closest to the current operational settings $S^c_{\mathrm{pj}} = (26, 106)$, and the suggested settings $S^o_{\mathrm{pj}} = (30, 120)$. The distribution at S^o_{pj} is significantly wider than the one at $S_{\mathrm{pj}} = (26, 105)$, making S^o_{pj} a preferable set of settings for optimal slow extraction.

The width d^o at S^o_{pj} increases by 27 % over the width d^c at $S_{\mathrm{pj}} = (26{,}105)$. However, the height h^o also increases by 21 % over h^c. But this increase in height is compensated for by the increase in width, as the average gradient at S^o_{pj} is lower. Therefore, S^o_{pj} is easier to adjust to at slow extraction. Overall, the distribution at $S^o_{\mathrm{pj}} = (30, 120)$ is hence preferable over the one at $S_{\mathrm{pj}} = (26, 105)$, especially if the edge spikes are just artifacts of the reconstruction.

3.6. Operational Implementation

The suggested settings $S^o_{\mathrm{pj}} = (30{,}120)$ were deployed on the operational STFPRO cycle with an intensity of $I \approx 4.76 \cdot 10^9$ ppb on 28.07.2023. Unlike in the MD cycle used for measurements, slow extraction was now performed, and the energy distributions inferred from the extraction process for both S^c_{pj} and S^o_{pj}. These inferred energy distributions were obtained by convolving the measured intensity from beam current transformers with the momentum adjustments done during slow extraction, using an

algorithm developed by F. M. Velotti [30].

Implementing the suggested settings S^o_{pj} had a positive impact on the energy distribution, as shown by the example in Fig. (3.6.1). Taking an average over 12 measurements, each acquired between 7:00-7:03 and 9:25-9:28 UTC, the height increased slightly from $h^c = 0.529\,\%$ to $h^o = 0.539\,\%$. Meanwhile, the width increased by 7.3 %, going from $d^c = 6.87 \cdot 10^8$ eV to $d^o = 7.38 \cdot 10^8$ eV. This decreased the average gradient from $0.366\,\%/(10^8$ eV) to $0.307\,\%/(10^8$ eV), therefore yielding a 16 % drop. Note that, to reduce noise for this evaluation, the inferred data was smoothed by taking a running average over 3 data points, amounting to 1.5 % of the total data points.

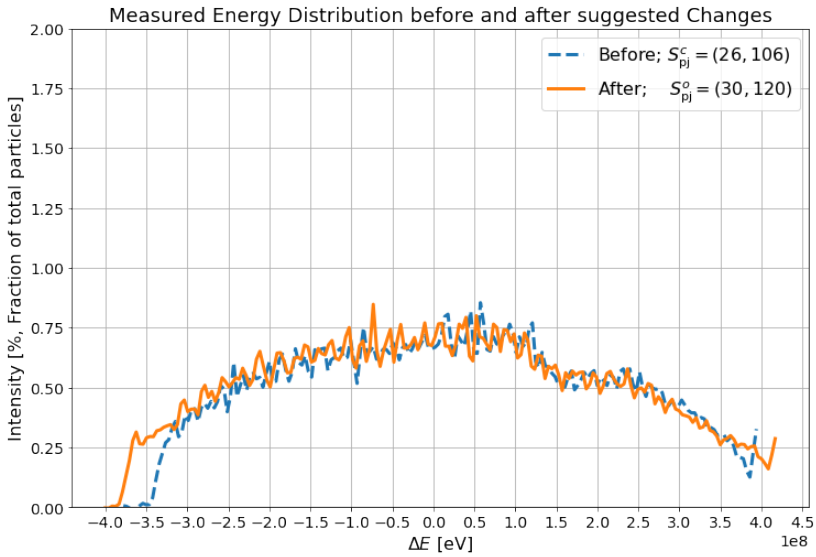

Figure 3.6.1: Energy distributions inferred from measurements of particles extracted during slow extraction for S^c_{pj} = (26,106) (blue, dashed) and S^o_{pj} = (30,120) (orange, solid). The change from S^c_{pj} to S^o_{pj} produces a minor, but noticeable improvement in the distributions' width.
Data was collected on the 28.07.2023 at 07:02:45 and 09:26:02 UTC respectively.

Though implementing S^o_{pj} improved the energy distribution at extraction, there is a significant deviation between expectation and observation: the predicted 27 % increase in width only amounted to 7.3 % in reality. To determine the cause of this, Figures (3.6.2a) and (3.6.2b) show a comparison between the reconstructed and inferred distributions.

In both cases, the reconstruction captures the middle part of the inferred distribution

well, however the spikes at its edges appear to be artefacts, as hypothesized previously. These spikes cause the edges, which are smooth in both measured cases, to be highly misrepresented. Therefore, the widths of the reconstructed distributions do not match reality, leading to the described deviation.

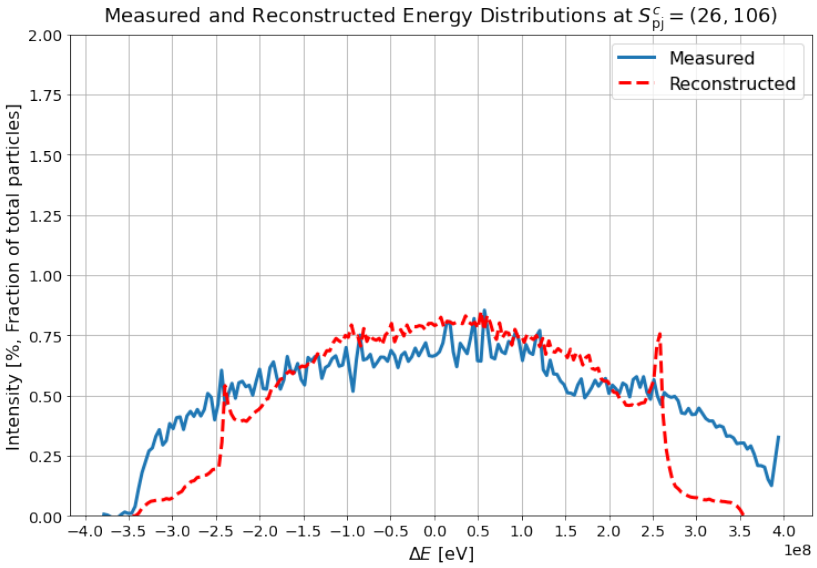

(a) Distributions at $S^c_{\mathrm{pj}} = (26, 106)$ (inferred) and $S_{\mathrm{pj}} = (26, 105)$ (reconstructed). Measured data taken at 07:02:45 UTC.

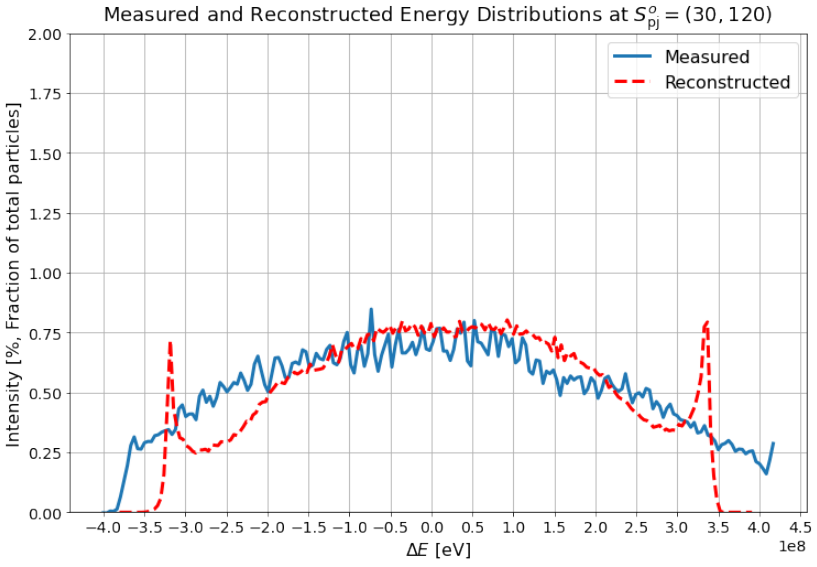

(b) Distributions at $S^o_{\mathrm{pj}} = (30, 120)$. Measured data taken at 09:26:02 UTC.

Figure 3.6.2: Comparison between reconstructed (red, dashed) and inferred (blue, solid) energy distributions before and after the implemented changes. While the distributions match around $\Delta E = 0$ MeV, a discrepancy between reconstructed and measured distributions is visible at their edges.

However, the general trend the reconstructed distributions show is accurate: the distribution becomes wider, slightly higher, and has a significant drop in average gradient due to the implemented changes. Despite the peaks being artefacts, the reconstructions can therefore still be used to aid in optimizing phase jump settings, as they capture the general beam dynamics during and after the phase jump well, and are able to predict how the distribution will behave as phase jump settings change.

3.7. Summary

The optimization of the phase jump in the SPS was successful, as the proposed setting improved the energy spread of the SFTPRO beam, and therefore became the new operational setting. Despite impactful errors of 1-8 % in the tomographic reconstructions needed to obtain the energy distributions, the analysis allowed a change in operational settings which yielded a 7.3 % increase in distribution width, while also significantly decreasing the average distribution gradient. Due to these errors however, the reconstructions systematically overestimate peaks at the distribution edges, and are not a reliable predictor of the exact shape of the energy distribution at extraction. Nonetheless, they model the general beam dynamics accurately, and can be used in the future to optimize the phase jump settings in the following years for the SFTPRO, or other cycles.

Based on this analysis, further study of the behaviour of the energy distributions at higher intensities is interesting, considering the ECN3 project, which aims to increase fixed target beam intensity [31]. Additionally, further fine-tuning of the tomography and BlonD tracking codes could be done to reduce the error of this analysis and increase its reliability. However, more complicated optimizations, including e.g. multiple phase jumps, necessitate tools other than tomography. These tools become necessary, as tomography can only be performed accurately and with reasonable runtime on short timeframes. Therefore, implementation of more complex optimization techniques not relying mainly on tomography is recommended to further increase the quality of slow extraction. One such technique is developed for the PS BigTOFEAST cycle in Chapter 4, and could be extended to the SPS SFTPRO in the future.

4. Optimizations of fixed-target beams at the PS

In the PS, more radical beam and RF manipulations are possible due to additional flexibility of the RF systems when compared to the SPS. This additional flexibility is, in part, a result of having to accommodating lower energy beams, with its maximal energies in the PS reaching approximately 24 GeV. The exploitation of this more flexible RF system allows delivery of beams to various destinations, such as the East Area and the n_TOF experiment. However, these destinations require different extraction techniques, which sometimes are performed in the same beam cycle, as different bunches target different experiments. This, in turn, entails more complex RF manipulations, producing more complex cycles and than in the SPS, and requiring more sophisticated optimization techniques.

Here, such a cycle, where the beam consists of two bunches extracted in two different ways, is investigated: the bunch with higher intensity is the neutron Time-of-Flight bunch (TOF), which is sent to the corresponding n_TOF experiment. The TOF bunch is also called "parasitic" [32], as this cycle is based on one which originally only contained the second, less intense bunch, called EAST, and sent to the East Area experiments. This parasitic TOF bunch was introduced to increase the total particle flux arriving at the n_TOF experiment while maintaining beam delivery to the East Area. Operationally, a higher intensity parasitic TOF bunch is therefore desired, as a higher flux to n_TOF in this parasitic scenario leads to less machine time needing to be dedicated to beam cycles only containing the TOF bunch. This freed up time then allows for additional flexibility in how beam is delivered to other experiments, reducing the likelihood of bottlenecks. However, while dedicated TOF cycles can reach bunch intensities of $> 800 \cdot 10^{10}$ protons, the parasitic TOF bunch intensity has only recently been pushed from $250 \cdot 10^{10}$ to $350 \cdot 10^{10}$ protons. Due to this desire to increase the parasitic TOF bunch intensity, this cycle with a parasitic TOF is called BigTOFEAST in operation.

While the EAST bunch in the BigTOFEAST cycle is extracted by means of slow extraction [20], fast extraction is used for the TOF bunch [33]. This means that the requirements for both bunches at extractions are different, even though they are

accelerated in the same cycle. Nonetheless, a bunch rotation by phase jump is performed for both before extraction. Therefore, in contrast with the SPS SFTPRO cycle, not one, but three phase jumps with different requirements have to be completed successively to properly extract both bunches. This chapter will focus on the optimization of the initial two phase jumps to limit the complexity of the problem. Nevertheless, the numerical optimization of these two phase jumps necessitates accurate PS impedance and feedback loop models, alongside a sophisticated optimizer, with the latter two being developed in this chapter.

First, the details of the BigTOFEAST cycle and initial beam quality concerns motivating this study are outlined. Afterwards, the current model of the PS beam phase and radial feedback loop controls for fixed-target beams is presented, as the feedback loops have a significant influence on the beam dynamics and quality in this cycle. To optimize the phase jump settings, three core components are then developed:
First, the feedback loop models are used to create a simulation, reproducing of BigTOFEAST beam's behaviour as accurately as possible. Then, a loss function is conceived based on key metrics, which defines a single figure of merit for quantifying phase jump quality in this cycle. Thirdly, an optimizer based on Gaussian processes is developed. This Gaussian Process Optimizer (GPO) uses the aforementioned simulations and loss function to scan the parameter space of phase jump settings efficiently, allowing automated and effective discovery of the optimal settings.
The output of the GPO is then verified by applying it to a simplified problem, after which the GPO is used to predict optimal settings for the BigTOFEAST cycle. To quantify this result, the beam behaviour and quality using these settings is analysed. Lastly, the GPO is used to probe bunch behaviour at higher intensities, establishing how intensity increases affect the bunch quality and particle transmission during the studied time frame.

4.1. BigTOFEAST Cycle Details

As shown in Fig. (4.1.1), the BigTOFEAST cycle accelerates particles from 2.8 GeV/c to 24 GeV/c (the second and final flat top), with an intermediate energy plateau at 20.3 GeV/c (the first flat top). The exact cycle parameters are listed in Table (4.1.1).

The first flat top between 725 and 730 ms cycle time (time after first injection) is used to extract the TOF bunch, which is more intense than the EAST bunch by an order of magnitude. The TOF bunch must be extracted with a comparatively low bunch length of $l_{\mathrm{T}} \approx 28$ ns and a short front tail [32], avoiding tails such as the one in Fig. (2.6.1d). Meanwhile, the EAST bunch is extracted with an energy of 24 GeV at the second flat top starting from 885 ms cycle time, and requires a flat energy distribution similar to the ones produced in Chapter 3, as it is slow extracted.

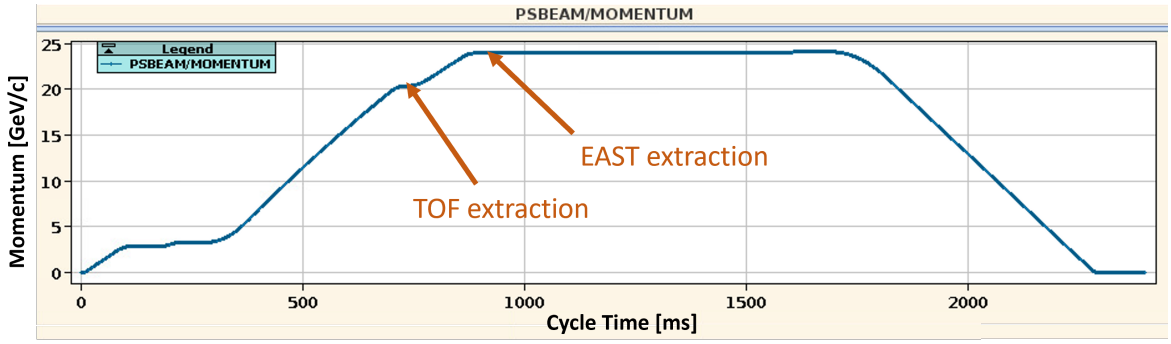

Figure 4.1.1: BigTOFEAST cycle momentum program in 2023. The first and second momentum plateaus (first and second flat top), used for TOF and EAST bunch extractions respectively, are labelled. This chapter will focus on the TOF extraction at the first flat top.

The process of extracting both bunches is complex, as both require a bunch rotation by phase jump prior to being extracted. In this process, the EAST bunch is affected by the first phase jump, used to extract the TOF bunch. The effects of this phase jump on the EAST bunch must be counteracted by a second phase jump after the TOF bunch is extracted. Then, the EAST bunch can be accelerated past the first flat top and finally be extracted by a third phase jump, tailored to widen and flatten its energy distributing at the second flat top. However, the EAST bunch's quality is significantly degraded after TOF extraction and subsequent counter phase jump, as seen in the right plot of Fig. (4.1.2): the EAST bunch starts to perform minor dipolar, and strong quadrupolar oscillations after TOF extraction. The dipolar oscillations are visible as oscillations in the mean Δt of the bunch, while the variation in particle density indicates quadrupolar oscillations. In phase space, these quadrupolar oscillations correspond to a stretched out, elliptical bunch rotating: a peaked profile becomes a

PS BigTOFEAST 1. Flat Top Parameters	
Parameter	Value
Reference energy E_0	20.32 GeV
Relativistic beta β_0	0.9989355
Reference momentum p_0	20.32 GeV/c
Circumference C	628.3 m
Bending radius ρ	70.079 m
Slippage parameter η_0	0.023286
Revolution time T_{rev}	2.098 μs
Harmonic number h	8
Bucket length T_{rf}	262.26 ns
Synchrotron Period T_s	$approx4$ ms $\approx 1900 \cdot T_{\text{rev}}$
Total 10 MHz voltage $V_{\text{rf},10}$	200 keV
Intensities $[I_T, I_E]$	$[355 \cdot 10^{10}, 28 \cdot 10^{10}]$ protons
TOF bunch extraction time T_{ex}	729 ms

Table 4.1.1: 2023 BigTOFEAST cycle parameters at the first flat top, at 725 ms cycle time. These parameters, except for T_s, are accurate to within at least six significant figures, and therefore more accurate than shown, hence no error is displayed.

wide one, which again becomes peaked after a time, and so on. Even after the counter phase jump, residual dipole and quadrupole oscillations are visible, reducing beam quality later at EAST extraction.

The degradation of the EAST bunch's quality occurs due to the first phase jump being tailored to extract TOF at a minimum bunch length with a short front tail of the bunch. During this initial phase jump, EAST bunch quality is a secondary priority. The second phase jump is then used to counter the degradation EAST experiences, however even a perfect second phase jump cannot compensate the first, suboptimal phase jump fully. This is due to the following factors, which complicate this process:

1. During the initial phase jump, the TOF bunch induces a voltage affecting the EAST bunch through long range wakefields. However, these collective effects are not present in the second phase jump, as TOF is already extracted at that time. Therefore, the EAST bunch experiences different forces during the two phase jumps, complicating corrections.

2. The extraction of the TOF bunch causes a discontinuity in the measurement of the beam's phase, which causes the middle of the RF bucket to be kicked away

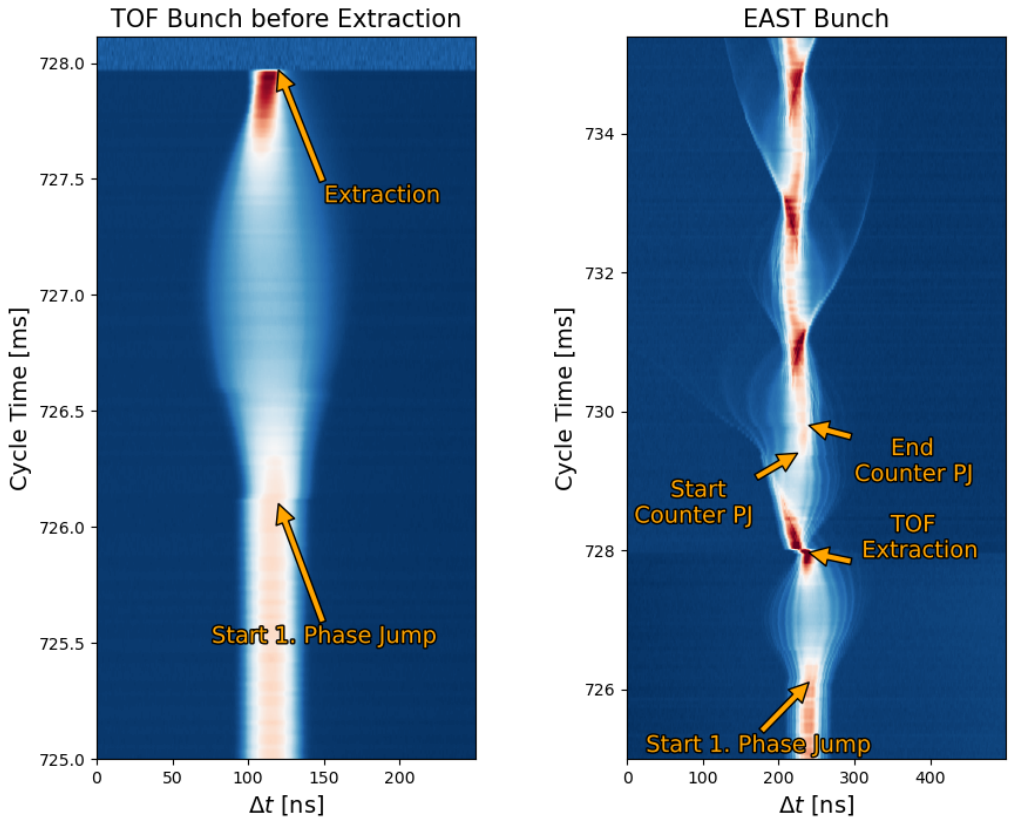

Figure 4.1.2: Measured waterfalls of the TOF and EAST bunches during TOF extraction at the first flat top. The x-axis shows the longitudinal position of the bunch's particles as the bunch evolves with time, shown on the y-axis. The colour signifies particle density, with blue signifying a low, white a medium and red a high density. Note that the axes and colour scales are different for both waterfalls, as bunch parameters differ significantly.

from the centre of the remaining EAST bunch by the beam phase feedback loop. This unintended RF phase kick induces bunch oscillations, whose negative effects on beam quality are amplified by the bunch rotating at this time due to the first phase jump.

3. The longitudinal beam dynamics during the phase jump are inherently nonlinear, as the particle bunch is far from the centre of the bucket. Therefore, the second phase jump used to counter-rotate EAST cannot do so perfectly, even under ideal conditions.

The goal of this chapter is to account for these complicating factors and optimize the settings of the two phase jumps, occurring at the first flat top. Table (4.1.2)

summarizes the parameter set S^m_{PS}. The "m" in this notation stands for "measured", as this is the parameter set used to take the measurement in Fig. (4.1.2), and determined purely by empirical optimization. The start times $\tau_{s,i}, i \in 1, 2$ are the cycle times when the phase jump begins, while the phase jump durations $\tau_{j,i}$ are how long it is maintained before jumping back to the stable phase. Also note that the first phase jump is not symmetric: the amplitude $\phi_{\uparrow,1}$ by which the phase is shifted when jumping to the unstable phase is different from the amplitude $\phi_{\downarrow,1}$ that is used to jump back to the stable phase afterwards. This is done to optimize the front tail of the TOF bunch and offset the effects of the aforementioned sources of quality degradation: the asymmetry in the phase jump created by the TOF extraction is compensated for by the beam not being at exactly the unstable phase during the phase jump, and not exactly at the synchronous phase afterwards.

PS BigTOFEAST Phase Jump (PJ) Parameters	
Parameter	Value
1. PJ start time $\tau_{s,1}$	726.1 ms
1. PJ duration $\tau_{j,1}$	0.465 ms
2. PJ start time $\tau_{s,2}$	729.4 ms
2. PJ duration $\tau_{j,2}$	0.4 ms
1. PJ forward amplitude $\phi_{\uparrow,1}$	152°
1. PJ backward amplitude $\phi_{\downarrow,1}$	176°
2. PJ forward amplitude $\phi_{\uparrow,2}$	180°
2. PJ backward amplitude $\phi_{\downarrow,2}$	180°

Table 4.1.2: Settings S^m_{PS} for the first and second phase jumps occuring at the first flat top of BigTOFEAST cycle. The values were taken in November 2023, before any optimization.

However, initial simulations show that both the voltage induced by the TOF bunch and the kick performed by the beam phase feedback loop have a visible, but minor effect on the quality of the EAST bunch. Neither effect can be identified as the main cause of the EAST bunch degradation, as simulations with and without these sources of error are highly similar. Instead, their interplay, the prioritization of TOF, and the fact that a bunch rotation by phase jump is not perfectly reversible due to nonlinear dynamics cause this degradation. Essentially, the longitudinal beam dynamics themselves and the initial focus on an optimal TOF bunch make it difficult to perform an optimal counter-rotation to the first rotation by phase jump.

Therefore, the already developed PS impedance model [27] is used and a model of the PS feedback loops is developed to accurate simulate these dynamics. These then serve as a tool to find optimal phase jump settings for the initial two phase jumps, optimizing both TOF and EAST bunch quality in parallel.

4.2. PS Beam Feedback Loops

While the PS impedance model was already developed beforehand, a model of the beam phase and radial feedback loops was created in the course of this thesis. This section aims to summarize that work, further detailed in [34], as a detailed model of the feedback loops is necessary for accurate simulations and to understand the beam's behaviour during the BigTOFEAST cycle.

Both the phase and radial loops are active in the BigTOFEAST cycle to stabilize the beam. As elaborated on in Section 2.8, both loops work by measuring the phase or radial offset, filtering it, and then inducing a frequency change proportional to the filtered measurement.

4.2.1. Phase Loop

The beam phase φ_b is measured by capturing the phase signal with a wideband pickup and then extracting its ω_{rf} component by downsampling. Numerically, this is modelled by calculating the beam phase via

$$\varphi_b := \arg\left(\hat{\lambda}(\omega = \omega_{\mathrm{rf}})\right) = \arg\left(\mathcal{F}[\lambda(\tau)](\omega = \omega_{\mathrm{rf}})\right) = \arg\left(\int_{\mathbb{R}} \lambda(\tau) e^{i\omega_{\mathrm{rf}}\tau}\, d\tau\right), \quad (4.2.1)$$

i.e. the phase of the beam spectrum $\hat{\lambda}(\omega_{\mathrm{rf}})$ at the RF frequency. In first order of a thin line density or beam profile $\lambda(\tau)$, meaning if $\lambda(\tau) > 0$ only for $\tau \in [\tau_a, \tau_b]$ with $\tau_b - \tau_a \ll \frac{1}{\omega_{\mathrm{rf}}}$, this is equivalent to the profile's centre of mass. Concretely, in approximation to first order,

$$\varphi_b = \arg(\hat{\lambda}(\omega_{\mathrm{rf}})) \approx \omega_{\mathrm{rf}} \frac{\int_{\mathbb{R}} \tau\lambda(\tau) d\tau}{\int_{\mathbb{R}} \lambda(\tau) d\tau},$$

giving an intuitive understanding of the beam phase as the phase corresponding to the beam's longitudinal centre of mass.

Note that Equation (4.2.1) explains the discontinuity of the beam phase measurement during TOF extraction, seen at the EAST bunch in Fig. (4.1.2): the beam profile has a discontinuity as the TOF bunch is extracted, causing a discontinuity in its Fourier transform and therefore in the measured beam phase. Speaking in more concrete, physical terms, the synchronous phase shift due to collective effects is different for both bunches due to their different shapes and intensities. This means that the synchronous phase of the TOF bunch φ_b^T, which dominates the beam phase measurement due to TOF being 10 times more intense, is different than that of the East bunch φ_b^E. This causes the discontinuity in φ_b, as it jumps from $\varphi_b \approx \varphi_b^T$ to $\varphi_b = \varphi_b^E$ during TOF extraction.

Given the measured beam phase φ_b, the RF phase φ_{rf} and their difference $\Delta\varphi^{(n)} = \varphi_b^{(n)} - \varphi_{\mathrm{rf}}^{(n)}$ at turn n, the frequency adjustment induced by the phase loop is then calculated via

$$\begin{aligned} \Delta f_{\mathrm{rf,PL}}^{(n)} &= -G_{\mathrm{PL}} \Delta\varphi_f^{(n)} \\ &= -G_{\mathrm{PL}} \left[g_b(\Delta\varphi^{(n)} - \Delta\varphi^{(n-1)}) + g_a \Delta\varphi_f^{(n-1)} \right], \end{aligned} \tag{4.2.2}$$

with g_a, g_b being adjustable filter parameters. The filter applied to calculate $\Delta\varphi_f^{(n)}$ is therefore a high-pass filter, which filters DC phase changes, e.g. phenomena like the synchronous phase shift, where the synchronous phase itself changes by an approximately constant value. If these phenomena were not filtered, the loop would try to counteract them but fail, as the phase shift would constantly re-establish itself. Therefore, the loop would induce a constant RF frequency change, leading to complete beam loss. The filter's frequency response is demonstrated in Fig. (4.2.1).

4.2.2. Radial Loop

The radial offset ΔR is measured by using a collection of beam position monitors (BPM), which measure the current induced in the beam pipe by the beam's passage. Sets of BPMs are placed radially around various longitudinal positions in the beam

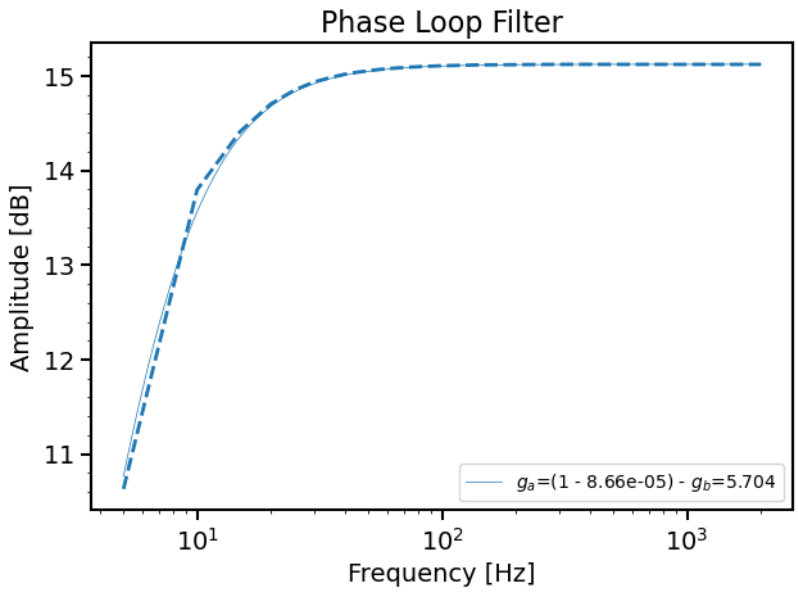

Figure 4.2.1: Frequency response of the phase loop filter for filter parameters used throughout this thesis. The filter removes low-frequency components of the signal, ensuring the phase loop does not correct for constant synchronous phase shifts.

pipe, allowing accurate beam position measurement through averaging the BPMs readouts [29].

Numerically, the average radial offset is determined through the beam's average ΔE. Based on [19, Eq. (2.86)], the relation is

$$\Delta R = \frac{1}{\beta_0^2 E_0 \gamma_t^2} \Delta E.$$

This is used, as no transversal beam dynamics are simulated in BLonD, meaning that there is no way to directly determine the (transversal) radial offset.

With this $\Delta R^{(n)}$ during turn n, the applied filter to calculate the frequency correction is

$$\begin{aligned} \Delta f_{\mathrm{rf,RL}}^{(n)} &= G_{\mathrm{RL}} \Delta R_f^{(n)} \\ &= G_{\mathrm{RL}} \left[(1-\alpha) \Delta R^{(n)} + \alpha \Delta R_f^{(n-1)} \right]. \end{aligned} \tag{4.2.3}$$

ΔR_f is the filtered radial offset, and α is again a parameter of the radial loop filter, determining its exact behaviour as a low-pass. As shown in Fig. (4.2.2), it filters

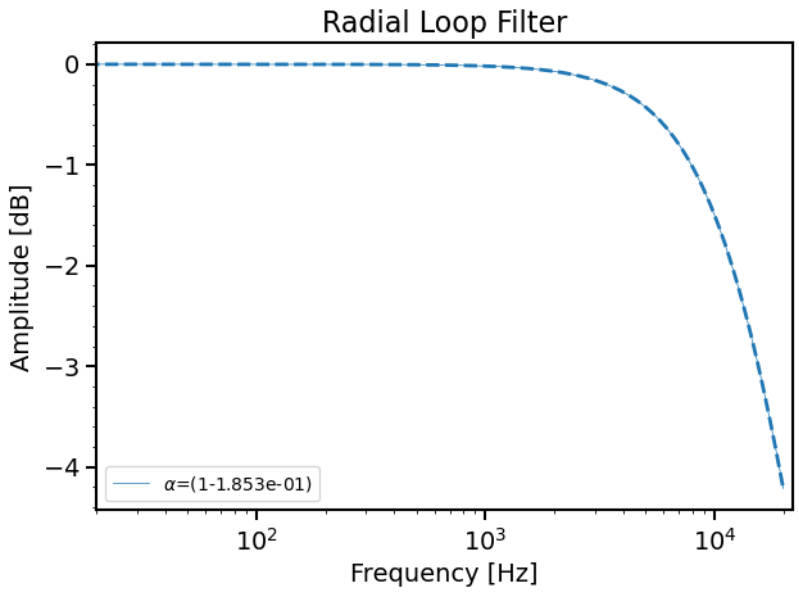

Figure 4.2.2: Frequency response of the radial loop filter for the settings used throughout this thesis. The filter removes high frequency components, ensuring that the radial loop does not interfere with the phase loop.

high frequency components as to not interfere with the phase loop. However, the phase loop operates most prominently at the synchrotron frequency, which is the natural frequency of the particle's, and therefore beam's, phase oscillation. Hence, one must note that in reality, the synchrotron frequency for the BigTOFEAST cycle is $\Omega_s/2\pi = 1/T_s \approx 250$ Hz, which is not filtered by the radial loop filter in Fig. (4.2.2). This is a known problem in the feedback loop controls of the PS, and to be remedied in the future.

Nonetheless, with both of these models, the gain parameters could be determined by comparing measurement and simulation [34]. They are

$$G_{\mathrm{PL}} = (9.4 \pm 0.2)\ \mathrm{kHz} \qquad G_{\mathrm{RL}} = (1.03 \pm 0.07)\ \mathrm{kHz/mm}.$$

This finalizes the beam phase and radial feedback loop models and allows their use in simulation to optimize the cycle's phase jumps.

4.3. Optimizer Creation

To perform the optimization of the phase jumps of the two phase jumps performed at the first flat top of the BigTOFEAST cycle, three components are developed. First, the

quantities determining bunch quality, and hence the quality of the optimization, are defined. These are then used to define a loss function, allowing efficient search of the optimal parameters in the parameter space spanned by possible values for the phase jump settings in Table (4.1.2). This loss function is finally used to create a Gaussian Process Optimizer (GPO) (see Appendix D for mathematical details), which scans the parameter space and suggests new, improved settings for both phase jumps.

4.3.1. Quantifying Phase Jump Quality

As described in Section 4.4, the bunch length of the TOF bunch towards the end of the simulation is captured accurately, while the EAST quadrupole oscillation amplitudes constitute an upper limit for the actual oscillations in the machine. This allows the TOF bunch length before extraction and EAST quadrupole oscillation amplitudes to be used as two meaningful metrics of phase jump quality. An additional key metric for the n_TOF experiment is the TOF front tail length, where a short tail is beneficial. In detail:

1. A short front tail length g_T is strongly desired for the TOF bunch. Specifically, the value of g_T is determined by calculating the length of the Δt-interval containing the first 2.5 % of particles of the TOF bunch. The measured value of $g_T = 3.8$ ns provides a reference to define a unitless and normalised metric for tail shortness $\Gamma_T = \frac{g_T}{3.8\text{ ns}}$, with smaller Γ_T indicating shorter tails and therefore better bunch quality.

2. A short TOF bunch length l_T at extraction is also desired for the TOF bunch. Here, $l_T = 28$ ns was achieved in measurement, however slight variations of the bunch length are always present operationally. Therefore, this metric is used to simply keep the bunch length within (28 ± 2) ns by setting the associated parameter to

$$Q_T(l_T) = \begin{cases} \frac{l_T}{1\text{ ns}} - 30, & \text{if } l_T > 30 \text{ ns} \\ 0, & \text{if } l_T \in [26, 30] \text{ ns} \\ 26 - \frac{l_T}{1\text{ ns}} & \text{if } l_T < 26 \text{ ns}. \end{cases}$$

3. The amplitude of quadrupole oscillations A_E of the EAST bunch can be used as a metric for how much the bunch is perturbed after both phase jumps. It

can again be normalised by the amplitude $A_E = 28$ ns observed in measurement, yielding $Q_E = \frac{A_E}{28\text{ ns}}$. Higher Q_E indicates stronger oscillations and a bigger bunch perturbation, which again implies worse phase jump settings.

However, note that Γ_T, Q_T and Q_E would be 0 if there was no beam. Therefore, without further precautions, the optimal phase jump settings would be those where all the particles are lost and none extracted. To prevent this, the particle losses of the TOF $L_T = \frac{N_{L,T}}{N_T}$ and EAST $L_E = \frac{N_{L,E}}{N_E}$ bunches are considered. Here $N_{L,T/E}$ are the number of particles lost for the TOF and EAST bunches respectively, i.e. the particles that move outside the RF bucket anytime the RF is not set to the unstable phase for the phase jumps. Meanwhile, $N_{T/E}$ is the total amount of particles the TOF and EAST bunches started the simulation with.

However, most losses do not occur directly in the simulated timeframe, but during the re-acceleration of the EAST bunch, which is not simulated due to runtime constraints. To account for these losses at acceleration from the first to the second flat top, the calculation of losses in the last 1000 turns of the simulation considers an accelerating bucket, with an acceleration of $\delta E = 25$ keV/turn. This corresponds to the average acceleration during the steepest section of the energy/momentum ramp from first to second flat top.

Similarly to the quality metrics, L_T and L_E are normalized to a reference value of 0.07, and higher values indicate higher losses and worse phase jump settings.

Taking into account all five metrics, the loss function is finally defined as

$$\mathcal{L} = w_1 Q_T + w_2 \Gamma_T + w_3 Q_E + w_4 L_T + w_5 L_E, \tag{4.3.1}$$

where w_i are weights quantifying the importance of each metric. Larger values indicate worse bunch quality for all five metrics making up the loss function, hence the optimal and target value of $\mathcal{L}$ is 0. Note that this is a very simple, linear loss function, which could be further improved by modifying or adding terms to emphasize certain metrics or smoothen $\mathcal{L}$, simplifying the process of finding a minimum for the GPO.

Here, this simple loss function is chosen for an initial analysis and proof of concept of the GPO, and the weights are used to determine the importance of each metric. They are chosen to be:

$$\begin{aligned} w_1 = 10 \quad w_2 = 1 \quad w_3 = 1 \\ w_4 = 2 \quad w_5 = 0.5. \end{aligned} \tag{4.3.2}$$

The high w_1 ensures that the TOF bunch length stays within $l_T \in [26, 30]$ ns. TOF losses are also avoided as much as possible, even over EAST losses, as TOF is an order of magnitude more intense. An additional consequence of this choice is that Γ_T and Q_E are weighted equally: the main metrics of quality for the TOF and EAST bunch are considered to be equally important as a baseline for further study. This setup results in a loss of $\mathcal{L} = 0.231$ for the simulation with the reference values in Table (4.1.2), shown in Section 4.4.

4.3.2. Creating the Optimizer

The GPO uses Gaussian processes to estimate the previously defined loss function $\mathcal{L}$ with a minimal number of evaluations (see Appendix D for mathematical details). Evaluation of $\mathcal{L}$ entails the simulation of both phase jumps, analogous to the simulations carried out in Section 4.4, hence the number of evaluations must be minimal to ensure runtimes on the order of days. For this, the simulation is simplified.

The main simplification is the reduction of time given to the feedback loops to establish equilibrium between themselves before the phase jumps begin: In Section 4.4, 60000 turns are used, while for the GPO only 1000 turns are used to reduce the runtime by an order of magnitude. This is the most efficient simplification, since the error incurred is minor relative to the runtime gain, as determined in Subsection 4.4.2.

A further simplification is the reduction of the parameter space. Of the parameters outlined in Table (4.1.2), only the first six are considered. The amplitudes of the second phase jump are fixed to $\phi_{\uparrow,2} = \phi_{\downarrow,2} = 180°$, as the EAST bunch does not require an asymmetric energy distribution. Hence, it should not require an asymmetric phase

jump, unless the asymmetries induced by the first jump's $\phi_{\uparrow,1}$ are not corrected for by the return amplitude $\phi_{\downarrow,1}$).

All the other six parameters are allowed to vary, resulting in the parameter set $S_{\mathrm{PS}} = (\tau_{s,1}, \tau_{j,1}, \tau_{s,2}, \tau_{j,2}, \phi_{\uparrow,1}, \phi_{\downarrow,1})$. To further limit the parameter space however, they are only allowed to vary in small intervals around the initial values. Concretely, the parameter intervals defining the size of the six dimensional parameter space are listed in Table (4.3.1).

Time Parameter	Interval in ms	Interval in turns, relative to Table (4.1.2)
$\tau_{s,1}$	$[725.68, 726.52]$	$[-200, 200]$
$\tau_{j,1}$	$[0.423, 0.507]$	$[-20, 20]$
$\tau_{s,2}$	$[729.07, 729.70]$	$[-156, 144]$
$\tau_{j,2}$	$[0.296, 0.628]$	$[-50, 109]$
Amplitude Parameter		Interval
$\phi_{\uparrow,1}$		$[140°, 180°]$
$\phi_{\downarrow,1}$		$[\phi_{\uparrow,1} - 30°, \phi_{\uparrow,1} + 30°]$

Table 4.3.1: Parameter space of the Gaussian Process Optimizer (GPO), which is constrained to improve GPO performance. The intervals specifying turn values refer to how many revolution turns that parameter may deviate from the reference value in Table (4.1.2).

The GPO is initialized with a Matérn kernel (see Appendix D, Eq. (D.3.1)), using length scales equal to half of the parameter-space-interval length of the corresponding parameter. The GPO then functions as outlined in Figure (4.3.1):

1. The GPO suggests ten different sets of parameters S_{PS}. The first ten parameter sets the optimizer analyses when it is initialized are manually chosen to contain the reference parameter set, alongside physically interesting cases, such as a symmetric first phase jump, or extreme values at the edges of the parameter space. In successive iterations, the GPO determines the ten most promising sets based on prior results.

2. Simulations are performed of the ten suggested S_{PS} in parallel, modelling the dynamics of the TOF and EAST bunch.

3. The bunch quality for both bunches is evaluated and the loss calculated. This result is used to adjust the GPO, more specifically the hyperparameters of the Gaussian process kernel, and suggest new S_{PS}.

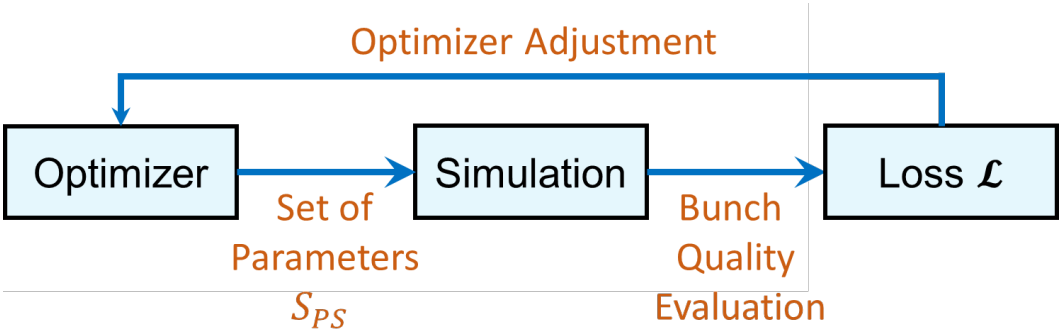

Figure 4.3.1: Schematic functionality of the GPO.

This iterative procedure ensures that the GPO continuously improves, successively increasing its probability of finding a minimum of $\mathcal{L}$. To increase the likelihood of this minimum being the global one, the GPO chooses the suggested parameter sets based on one of three so-called acquisition functions, chosen randomly for each iteration. Hence, by using this optimizer to evaluate only promising sets of parameters, the exploration of the 6-dimensional parameter space is expected to be performed significantly faster compared to brute force methods, such as a grid search.

4.4. Optimizer Verification

Before utilizing the GPO, the validity of the simulations it uses, its runtime and finally the validity of the GPO itself needs to be tested. First, the parameters chosen for the underlying simulations and the resulting accuracy are shown, with simulations reproducing measurements accurately. After this is confirmed, concerns about the runtime of the GPO are analysed and a simplification to resolve them is devised. The consequences of this simplification are discussed, after which the operation of the GPO itself can finally be verified. This is done by testing the GPO in a theoretically predictable scenario without collective effects and relaxed TOF bunch quality requirements. The results of this GPO run are then compared with predictions, and final conclusions are drawn on the validity of GPO.

4.4.1. Simulation Accuracy

To test the simulations underlying the GPO, a comparison between simulations and measurements of the BigTOFEAST cycle between 726 ms and 735 ms cycle time, taken on the 10.11.2023, is performed and shown in Figures (4.4.1), (4.4.2) and (4.4.3). These BLonD simulations are performed with 10^6 macroparticles and a cutoff frequency of $f_{\max} = 80$ MHz, following Tab. (B.2.2). This ensures that each simulation can be performed in a reasonable timeframe of 1-2 hours while including the impedance contributions from the main 10 and 20 MHz cavities. These settings will be used for all simulations going forward. The simulations also include the feedback models described in Section 4.2, and the impedances as determined in [27].

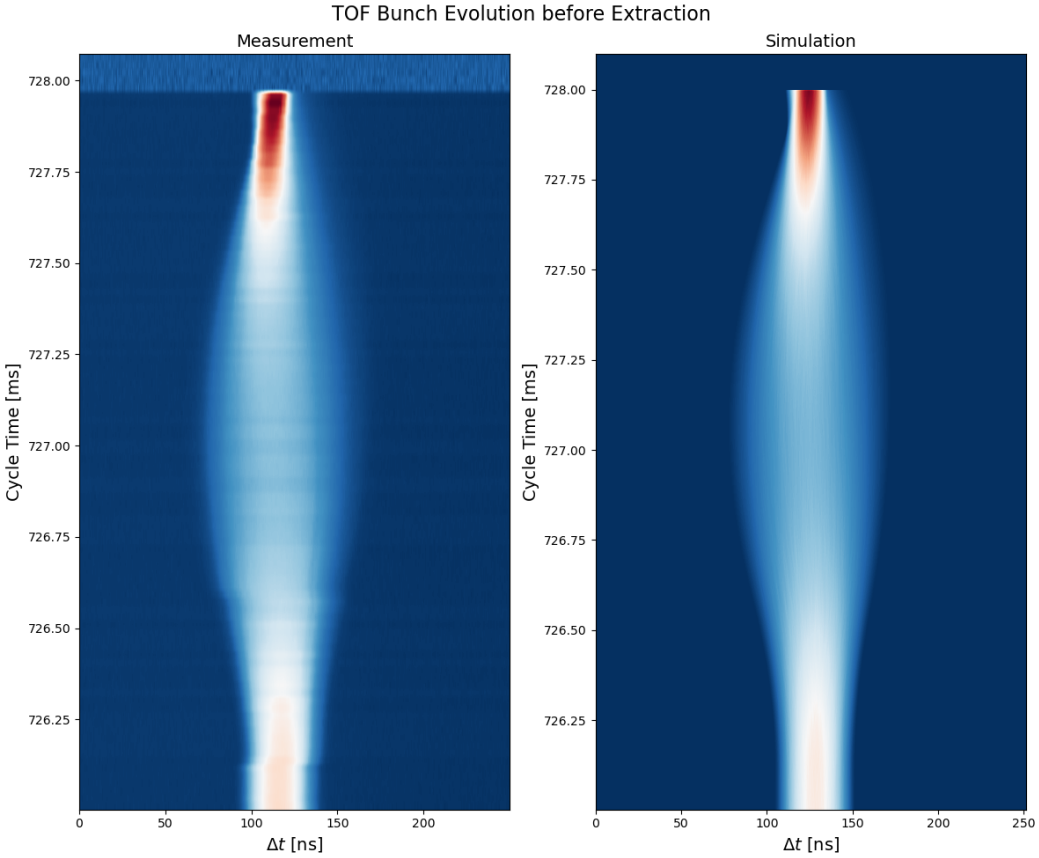

Figure 4.4.1: Measured and simulated waterfall of the TOF bunch profile before extraction, between 726 ms and 728 ms cycle time.

Figure (4.4.1) compares the measured waterfall of the TOF bunch to the simulated one. Here, the simulation captures the dynamics accurately and both waterfalls look almost identical.

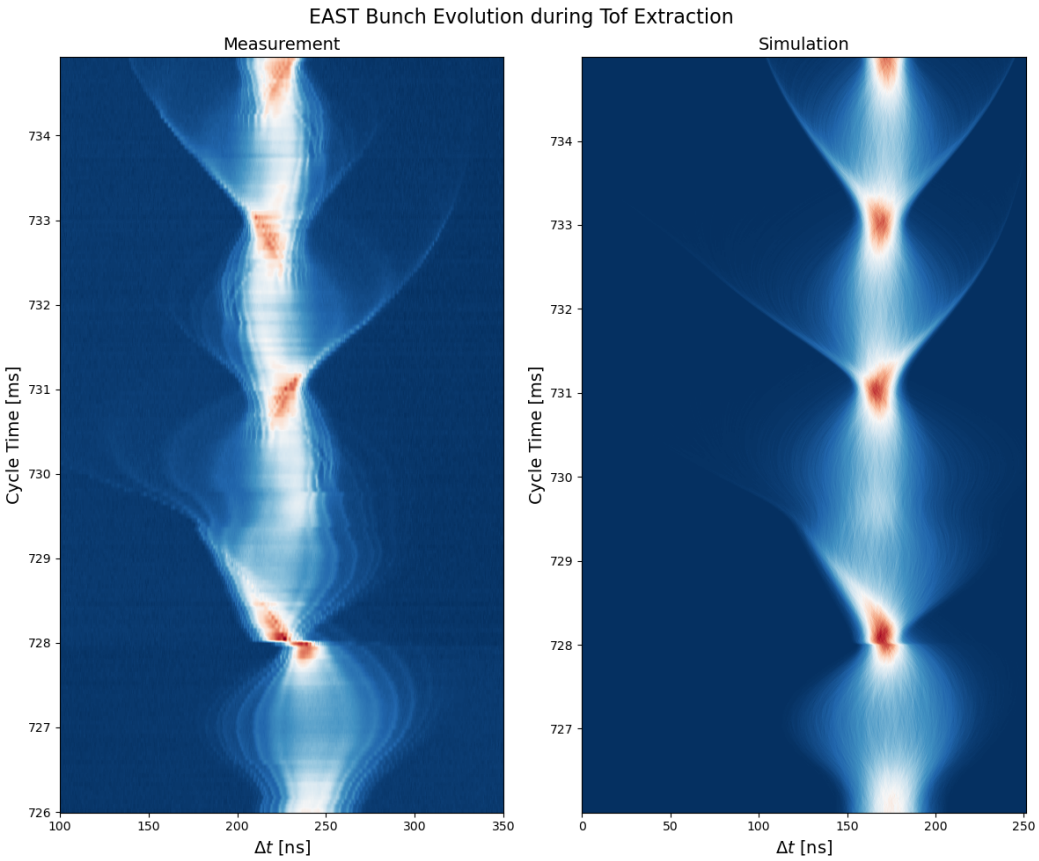

Figure 4.4.2: Measured and simulated waterfall of the EAST bunch profile during TOF extraction, between 726 ms and 728 ms cycle time. The simulation reproduces details of the measured bunch evolution accurately.

Figure (4.4.2) shows the EAST bunch under the same conditions. Here, a deviation is visible at 728 ms cycle time, where the phase glitch at extraction is corrected for. This is done as an attempt to improve beam quality, however, as stated in Section 4.1, it does not affect the evolution of the bunch majorly. Nonetheless, the waterfalls match well, and even the visible "hairs" of the bunch, produced by filamentation and the quadrupole oscillations, are reproduced accurately in the simulation.
The correction itself is done by shifting the measured beam phase manually at extraction. The shifted beam phase is calculated as $\tilde{\varphi}_b = \varphi_b - (\varphi_b - \varphi_{\mathrm{EAST}}) = \varphi_{\mathrm{EAST}}$, i.e. by subtracting the difference between the full beam phase, and the phase of only the EAST bunch φ_{EAST}. This corresponds to the difference between measured beam phase immediately before and after extraction, and the correction almost fully removes the phase glitch.

Overall, the bunch lengths of both bunches are captured with an average relative

error between measurement and simulation lower than 14 %. Figure (4.4.3) shows the evolution of the bunch lengths and the absolute errors. Especially during the time when the bunches are shortest, the error is smaller: the error at TOF extraction is 5.4 % or approximately 1.5 ns, and the average error of the EAST bunch length is 13.7 % , or 8.3 ns. Therefore, the TOF bunch length is captured accurately in simulation, while the EAST bunch length is slightly overestimated towards the second half of the cycle. Nevertheless, even smaller features, such as the small plateau where the EAST bunch length stays approximately constant around 730 ms cycle time, are captured accurately.

The deviations between measurement and simulation are most likely caused by the interplay of the beam with the feedback loops: in the simulation, this dynamical system where the phase and radial loop are both acting and adjusting the RF frequency in opposite directions does not have enough time to reach equilibrium. Namely, at the beginning of a simulation, the beam is slightly offset from equilibrium values due to it not being perfectly matched to the RF bucket, alongside collective effects. The loops' reaction to any offset of the beam phase from the equilibrium values is a dampened oscillation in the induced frequency offset. This means both the beam's phase and radial positions oscillate, with the oscillation requiring time to dampen out.

In the simulation shown, the loops are only given 1000 turns to equilibrate. However, the timescale of this dampening is on the order of 125 ms, i.e. approximately 60000 turns. This is very costly to perform in simulation, but is given in measurement due to the observation starting at 725 ms cycle time.

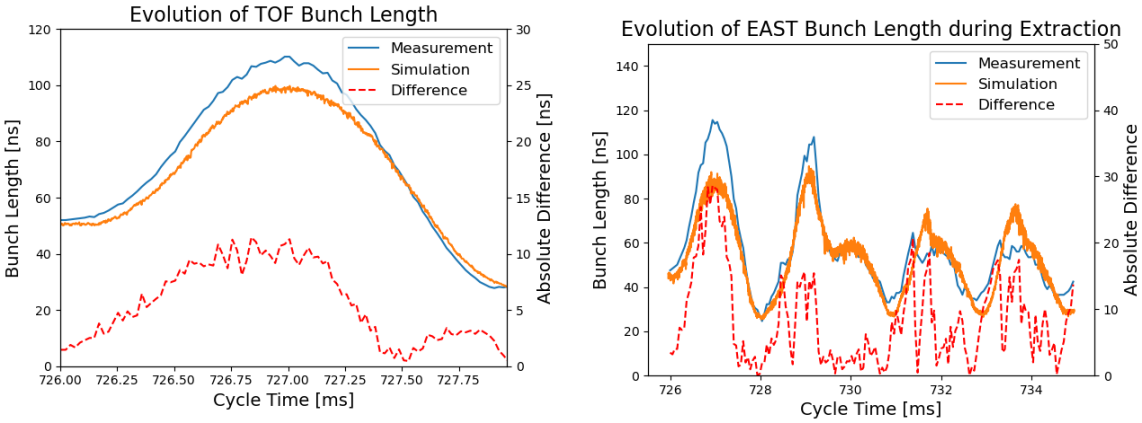

(a) Evolution of the TOF bunch length for 2 ms before extraction at 728 ms cycle time.

(b) Evolution of the EAST bunch length between 726 and 735 ms cycle time.

Figure 4.4.3: Bunch lengths of the TOF (left) and EAST (right) bunch determined in measurement and simulation. The absolute difference between measurement and simulation is marked in red, showing that the bunch lengths are reproduced accurately at TOF Extraction for the TOF bunch, and slightly overestimated at the end of the simulation for the EAST bunch. Please note the different scales of both axes.

In conclusion, the simulations have non-negligible deviations to measurements, but capture even finer details accurately. Especially the TOF bunch length near extraction is captured accurately, despite two phase jumps being performed in the observed timeframe. This allows the simulations to produce meaningful statements for one of the key bunch quality metrics of the TOF bunch. Additionally, the more chaotic dynamics of the EAST bunch are reproduced accurately, as shown by e.g. the matching "hairs" in both simulated and measured waterfalls.

Meanwhile, the residual quadrupole oscillations of the EAST bunch are slightly overestimated. Therefore, evaluating these quadrupole oscillations in the simulation may not yield the actual values in the machine, but the resulting values can still be used to set upper limits on the oscillation amplitude. This upper limit provides a meaningful figure of merit for evaluating the phase jumps' effect on the quality of the EAST bunch after TOF extraction, as it measures how strongly the EAST bunch is perturbed. Overall, this simulation is an effective tool to judge the quality of the two phase jumps for different settings, but further accuracy could be gained by increasing the number of equilibrium turns in the simulation.

4.4.2. Error due to Deviation from Loop Equilibrium

Although the number of equilibrium turns is an important parameter as seen above, increasing the number of equilibrium turns from 1000 to 60000 would increase the runtime of the simulations from 1-2 hours to 1-2 days. This is unacceptable, especially considering that the GPO will require at least on the order of 10^1 iterations. This is manageable when each iteration requires 1-2 hours, but not 1-2 days, as each optimization would take on the order of a month. Therefore, reducing the number of equilibrium turns is necessary.

To study the effect of this simplification, 11 simulations are performed with 60000 and 1000 equilibrium turns, respectively. They show that reducing the equilibrium turns introduces only minor errors for all metrics, aside from the TOF tail length g_T.
More specifically, the 11 simulations are performed with random parameter sets S_{PS}. The metrics outlined in Subsection 4.3.1 are then evaluated for each simulation, after which the deviation between the simulation with 60000 equilibrium turns, and the one with 1000 turns, is calculated. Table (4.4.1) lists these determined average, absolute errors.

TOF tail length error ϵ_g	2 ns
TOF bunch length error ϵ_l	0.4 ns
EAST oscillation amplitude error ϵ_A	2.09 ns
TOF losses error ϵ_{L_T}	0
EAST losses error ϵ_{L_E}	0.01

Table 4.4.1: Average errors in the metrics used, incurred from reducing the number of equilibrium turns in the simulation from 60000 turns to 1000. The error is minor for all metrics aside from the TOF tail length.

Relative to the reference values listed in Subsection 4.3.1, the errors of the TOF bunch length and EAST oscillation amplitude are 1.4 % and 7.4 % respectively. These are minor errors when compared to the runtime savings of an order of magnitude gained from the simplification.
Meanwhile, the error in the EAST losses relative to the reference value is 14.2 %, but

considering the low intensity of the EAST bunch, the absolute value of ±1 % losses is small enough where such an increase in particles lost would not significantly impact the beam cycle or machine operation.
The error in the TOF losses is 0, as none of the simulations had any losses incurred for the TOF bunch. This is simply due to the fact that the parameter space is small, and most parameters sets do not result in TOF losses. Therefore, if a parameter set incurring TOF losses is investigated, an additional simulation with 60000 equilibrium turns should be performed to verify the result.
Similarly, the error in the TOF tail length necessitates the verification of this metric: relative to the reference value, the error is above 50 %. Therefore, while increasing the number of equilibrium turns of the simulations used by the GPO would be too costly in runtime, all final parameter sets suggested by the GPO can still be verified to reduce this error. Verification is done by performing additional simulations with 60000 equilibrium turns and calculating the bunch quality metrics based on them, rather than using simulations with only 1000 equilibrium turns for the final evaluation.

4.4.3. Optimizer Verification

To finally verify the GPO's results themselves, it is tested in a scenario without collective effects and relaxed TOF quality requirements for a total of 50 iterations. Namely, the weights in Eq. (4.3.2) are changed to

$$\begin{aligned} w_1 &= 1 \quad w_2 = 0 \quad w_3 = 5 \\ w_4 &= 2 \quad w_5 = 5, \end{aligned} \tag{4.4.1}$$

with $w_1 = 1$ and $w_2 = 0$ meaning that the TOF bunch length is deprioritized and the TOF front tail length completely ignored for loss calculations. Meanwhile, the EAST quadrupole oscillation amplitude and losses are prioritized. Essentially, the EAST bunch is given priority over the TOF bunch in the optimization, while removing the additional complications stemming from collective effects.

With these changes, the optimization of the EAST bunch is expected to be the optimizer's priority. The optimization will also being easier for the GPO due to TOF not impacting EAST through collective effects, meaning a simplified shape of the loss

function. Therefore, a well performing optimizer is expected to reduce the EAST bunch's quadrupole oscillations and losses to a negligible level, while only slightly impacting the TOF bunch.

In this setup, the GPO yields the parameter set

$$S^v_{\mathrm{PS}} = \begin{pmatrix} \tau_{s,1} = 726.0986 \text{ ms}, & \tau_{j,1} = 0.4322 \text{ ms}, \\ \tau_{s,2} = 729.5520 \text{ ms}, & \tau_{j,2} = 0.3797 \text{ ms}, \\ \phi_{\uparrow,1} = 140.55°, & \phi_{\downarrow,1} = 161.59° \end{pmatrix}, \tag{4.4.2}$$

with "v" standing for "verification". This verification parameter set S^v_{PS} results in the metrics shown in Table (4.4.2) when used in a simulation with 60000 equilibrium turns.

Phase Jump Metrics

Metric	S^m_{PS}	S^v_{PS}
l_T [ns]	27.84	29.40
g_T [ns]	3.54	3.54
A_E [ns]	51.67	14.92
L_T [%]	0	0
L_E [%]	7	0.3

Table 4.4.2: Bunch quality metrics produced by the reference settings S^m_{PS}, compared to settings S^v_{PS}, produced without accounting for collective effects and with relaxed conditions on the TOF bunch. A significant reduction in EAST losses L_E and quadrupole oscillation amplitude A_E is visible, without significant degradation in the other metrics, as expected.

The table shows a significant reduction of the EAST quadrupole oscillation amplitude A_E and losses L_E, while increasing the TOF bunch length l_T and not changing the tail length g_T. This is the result expected, and the success of the overall optimization can be verified in Fig. (4.4.4): The TOF bunch is slightly longer at extraction but does not undergo any major changes. Meanwhile, the EAST bunch quadrupole oscillations are clearly dampened and the outgoing "hairs" are less populated. Essentially, the evolution of both bunches appears to be similar to the one observed with S^m_{PS}, but the counter-rotation by the second phase jump is more impactful, which leads to improvements in EAST bunch quality. However, the EAST bunch still performs quadrupolar oscillations, even though in this simplified their elimination was the main

priority. Surprisingly, the TOF front tail length also does not degrade, although it was not a targeted metric in this simplified setup. This indicates that the simple, linear loss function has unexpected consequences, which should be investigated in the future.

More explicitly, the comparison between S^m_{PS} from Table (4.1.2) and the newly produced S^v_{PS} shows that the phase jump asymmetry remains similar, however the initial phase jump is less drastic due to the reduction of $\phi_{\uparrow,1}$ from 152° to 140.55°. The second phase jump's start time is then significantly delayed from $\tau_{s,2} = 729.4$ ms to $\tau_{s,2} = 729.5502$ ms, corresponding to a delay of 113 turns. These changes to both phase jumps reduce the initial EAST bunch quality degradation and ensure an impactful counter-rotation with the second phase jump. However, the large phase jump asymmetry is again surprising, as this indicates the TOF front tail length is optimized for, when it should not be in this simplified setup.

Overall, the GPO produces the expected results and successfully predicts significant improvements in EAST bunch quality with minor TOF quality degradation when neglecting collective effects and deprioritizing TOF. However, questions about unintended consequences of the simple, linear loss function of the GPO remain, as it appears to optimize the TOF front tail length through an asymmetric first phase jump, although this should not be a target metric in this simplified setup. Hence, the GPO can produce settings yielding significant improvements, but further adjustments to the loss function are recommended to remove unexpected behaviour. Additionally, to fully prove the GPO's accuracy, direct measurements are necessary in the future.

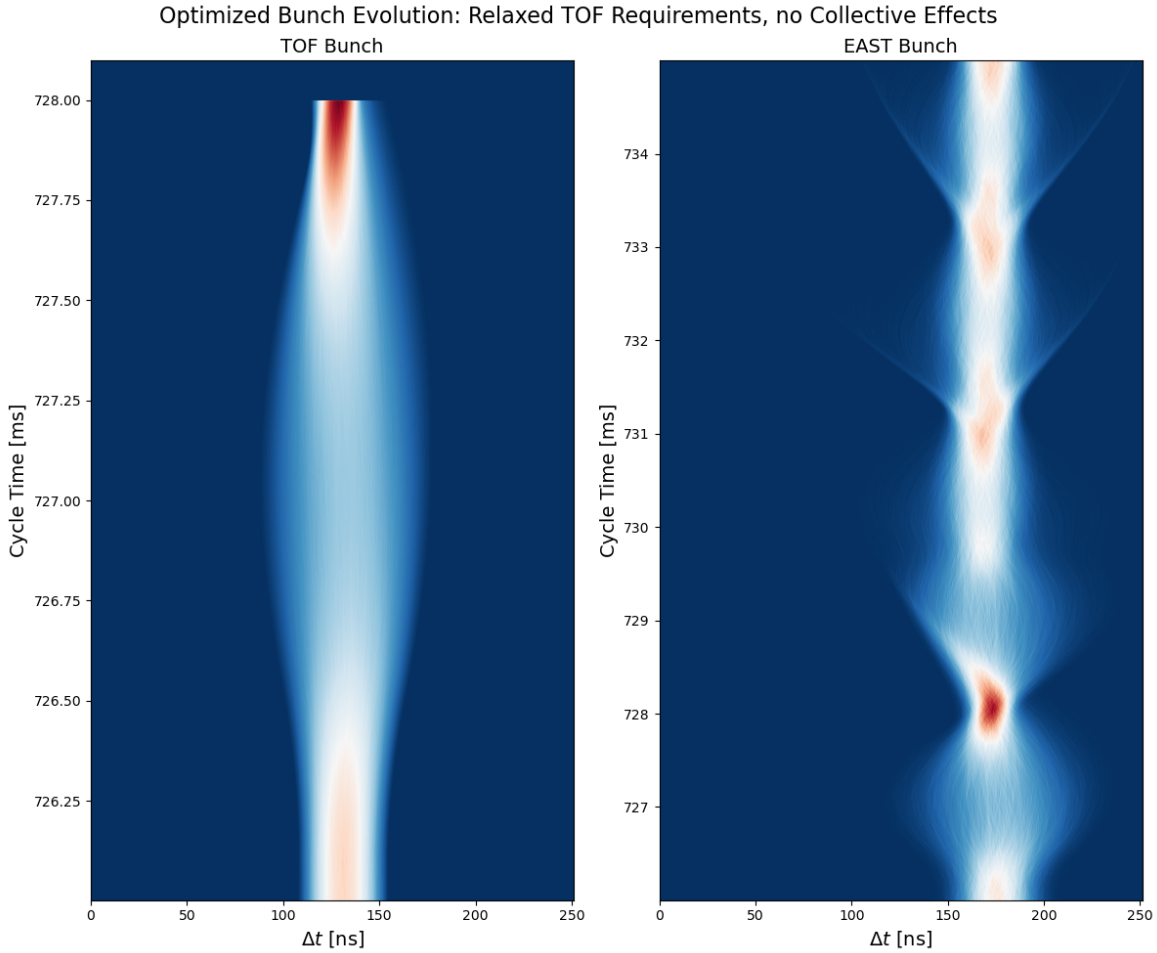

Figure 4.4.4: Waterfall of the TOF and EAST bunches at the optimal settings S^v_{PS} produced by the GPO in a scenario with relaxed TOF bunch quality requirements and no collective effects.

4.5. Results

With the GPO verified, all requirements stated in Subsection 4.3.1 are imposed, and the full impedance model is included to recreate the operational dynamics as accurately as possible. The bunch quality created with the resulting parameter set is then compared to the quality produced with the reference parameters in Tab. (4.1.2), allowing final conclusions about the worth of the GPO and possible improvements.
As a second use-case, the GPO is run with increased beam intensity while keeping all other conditions the same, which is done to study the intensity limitations of the BigTOFEAST cycle in the PS.

In all cases, the GPO is run with the simulation settings stated in Subsection 4.4.1 and 1000 equilibrium turns, simulating the dynamics between 726 ms and 735 ms cycle time. This timeframe includes both the phase jump for TOF extraction and the subsequent phase jump for counter-rotation, but does not include the re-acceleration or extraction of the EAST bunch. The GPO performs a given number of iterations, with each iteration consisting of 10 simulations for different parameter sets S_{PS}.

4.5.1. Optimization of BigTOFEAST Phase Jump Parameters

As the first application of the GPO to an operational cycle, an optimal parameter set S^o_{PS} ("o" for "optimized") with minimal loss $\mathcal{L}$ is determined for the PS BigTOFEAST cycle, taking into account both PS feedback loops and impedance models. To evaluate the impact of this optimization, the loss $\mathcal{L}$ of the simulation performed with S^o_{PS}, suggested by the GPO, is compared to a simulation with the reference parameters S^m_{PS}.

Initially, to verify proper functioning of the GPO when including collective effects, its convergence is studied. Using the GPO as outlined in the beginning of this section, and with 50 iterations, the minimal loss of each iteration should converge to a loss plateau after a certain iteration. Figure (4.5.1) shows the convergence properties of the GPO, plotting minimal loss against iteration number and a linear fit of this data.

Though the data does not have a linear dependency, the loss slightly trends down with the iteration number, with the slope of the linear fit m indicating

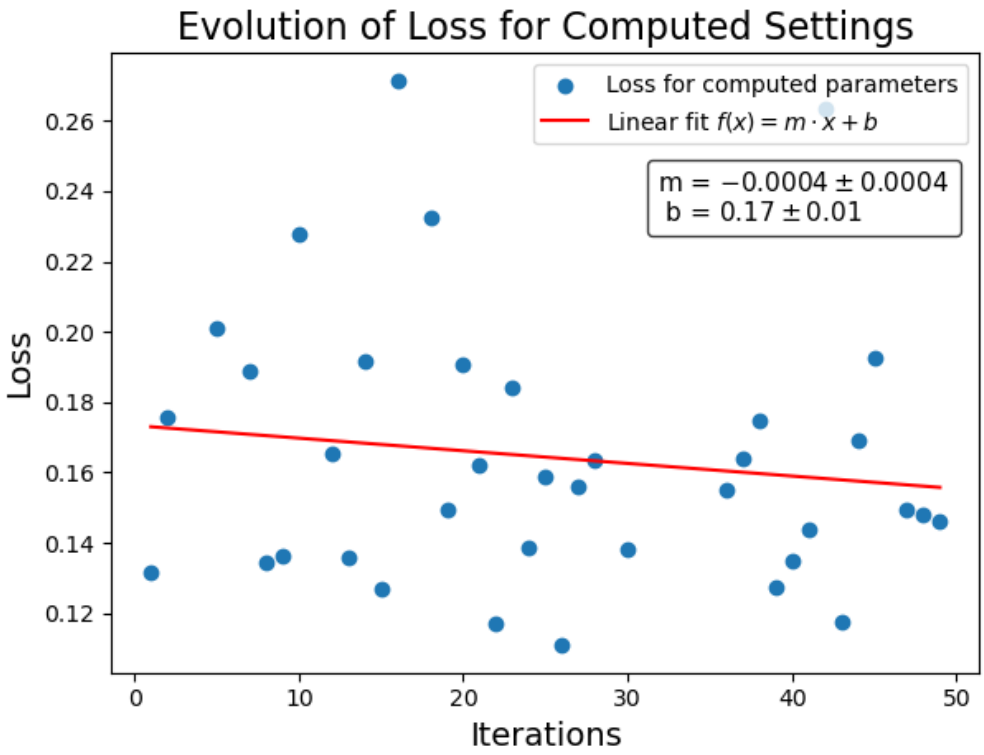

Figure 4.5.1: Evolution of the loss $\mathcal{L}$ calculated by the GPO as a function of the iteration number for 50 iterations. The GPO's $\mathcal{L}$ drops until approximately iteration 30, after which it appears to plateau.

that the loss drops by $m = -0.0004$ every iteration. However, as m is small and $m = 0$ is within the error bounds of the fit, this trend is minor. Nonetheless, the loss visibly trends down until 30 iterations, after which no further reduction of loss is achieved: the optimizer reaches convergence after this point. Therefore, a small quantity of iterations performed already yields results close to the best achievable results, with an increase in iterations only yielding minor to no improvements.

Overall, this performance indicates the GPO is most time-efficient at a low number of iterations, but can be used for longer periods of time to obtain truly optimal results at significant costs in runtime.

At iteration 26, the optimal parameter set

$$S^o_{\mathrm{PS}} = \begin{pmatrix} \tau_{s,1} = 726.0147 \text{ ms}, & \tau_{j,1} = 0.4532 \text{ ms}, \\ \tau_{s,2} = 729.372 \text{ ms}, & \tau_{j,2} = 0.4112 \text{ ms}, \\ \phi_{\uparrow,1} = 157.20^\circ, & \phi_{\downarrow,1} = 150.97^\circ \end{pmatrix} \tag{4.5.1}$$

is attained, with an incurred loss of $\mathcal{L} = 0.111$. Compared to the original parameter set S^m_{PS} in Table (4.1.2), notable changes are a significantly reduced phase jump asymmetry $\phi_{\uparrow,1} - \phi_{\downarrow,1} = -6.23^\circ$ and a much earlier initial phase jump at $\tau_{s,1} = 726.0147$ ms, as well as an increase in second phase jump start time $\tau_{s,2}$.
Essentially, the initial phase jump appears to require more significant changes to become less disruptive for the EAST bunch when compared to the settings under relaxed conditions in Eq. (4.4.2). The second phase jump is adjusted similarly, with an increased $\tau_{s,2}$ despite the reduced $\tau_{s,1}$ showing that the delay between first and second phase jump grows much larger in this setup as well.

To reduce error, the simulation is rerun and evaluated with 60000 equilibrium turns for both S^o_{PS} and S^m_{PS}. The resulting bunch quality metrics in Table (4.5.1) indicate a successful optimization. Although the loss for S^o_{PS} has risen from $\mathcal{L}^o = 0.111$ to $\mathcal{L}^o = 0.125$ when simulating with 60000, rather than 1000 equilibrium turns, it still constitutes an improvement over the original parameter set's loss of $\mathcal{L}^m = 0.231$. This increase in $\mathcal{L}^o$ is mainly due to the inaccuracy of the TOF tail length acquisition when performing simulations with 1000 equilibrium turns, as mentioned in Subsection 4.4.2.

Phase Jump Metrics

Metric	S^m_{PS}	S^o_{PS}
$\mathcal{L}$	0.231	0.125
l_T [ns]	27.84	27.72
g_T [ns]	3.54	3.91
A_E [ns]	51.67	18.49
L_T [%]	0	0
L_E [%]	7	0.4

Table 4.5.1: Bunch quality metrics for simulations performed with the reference and optimized settings S^m_{PS} and S^o_{PS}, respectively. A_E and L_E are significantly decreased, however the TOF front tail length g_T also increases notably.

The most significant difference between the resulting metrics is the significant reduction in EAST losses L_E and oscillation amplitude A_E for S^o_{PS}, at the cost of an increase in TOF tail length g_T over S^m_{PS}. Notably, S^o_{PS} produces an A_E that even surpasses the best measured value of $A_{E,\mathrm{meas}} \approx 28$ ns. Nonetheless, considering the errors between simulation and measurement shown in Section 4.4, this result still needs to be verified by measurements of the cycle with S^o_{PS}.

Studying the significant difference in metrics between S^m_{PS} and S^o_{PS} in more detail, the EAST bunch evolution for both cases is depicted in Figures (4.5.2) and (4.5.3). They indicate that the bunch behaves similarly in both cases, with the bunch in the optimized case suffering similar, but damped negative effects.

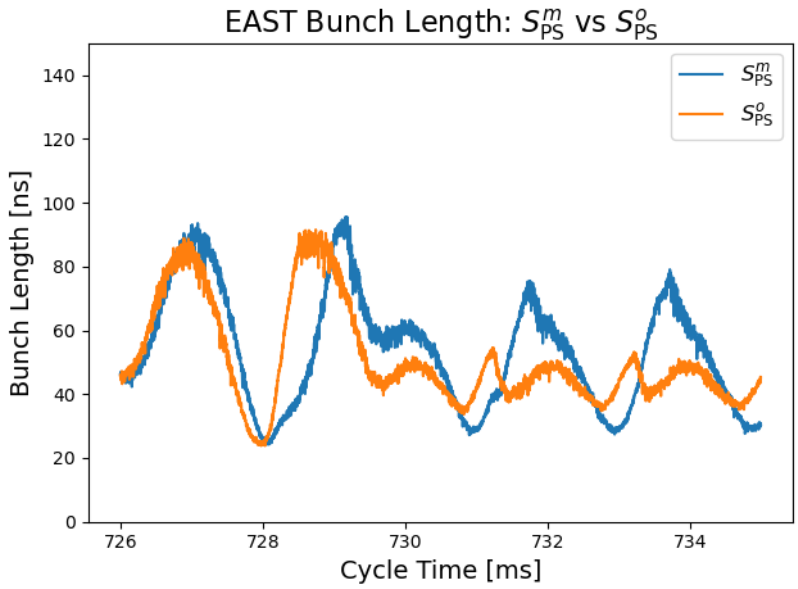

Figure 4.5.2: Evolution of the EAST bunch lengths produced by simulations with the reference parameters set S^m_{PS} (blue) and the optimized one S^o_{PS} (orange). The quadrupole oscillation amplitude A_E is significantly dampened for S^o_{PS}.

Here, this is due to the significantly reduced phase jump asymmetry, resulting in a much smaller excursion of the EAST bunch's centre of mass and reduced quadrupole oscillations. This is mainly visible at 728 ms in Fig. (4.5.3), where the bunch in the optimized case does not perform as strong of an excursion to the left. Compared to the relaxed conditions in Subsection 4.4.3, the reintroduced TOF bunch quality requirements force the initial phase jump to be more disruptive for EAST with

$\phi_{\uparrow,1} = 157.20°$ being larger than before, which is compensated for with the reduced phase jump asymmetry present in S^o_{PS}.

The smaller EAST bunch perturbation at 728 ms then allows for a cleaner second phase jump to counter-rotate the bunch, as is visible around 729.4 ms in Fig. (4.5.3). The improvement in the second phase jump's quality, similarly to Subsection 4.4.3, then produces a significant reduction in the amplitude A_E of the residual quadrupole oscillations, portrayed in Fig. (4.5.2). It also results in minimal losses, as the significantly less populated "hairs" of particles far from the centre of the bunch indicate that fewer particles lie close to the separatrix, while more are captured in the centre of the bucket.

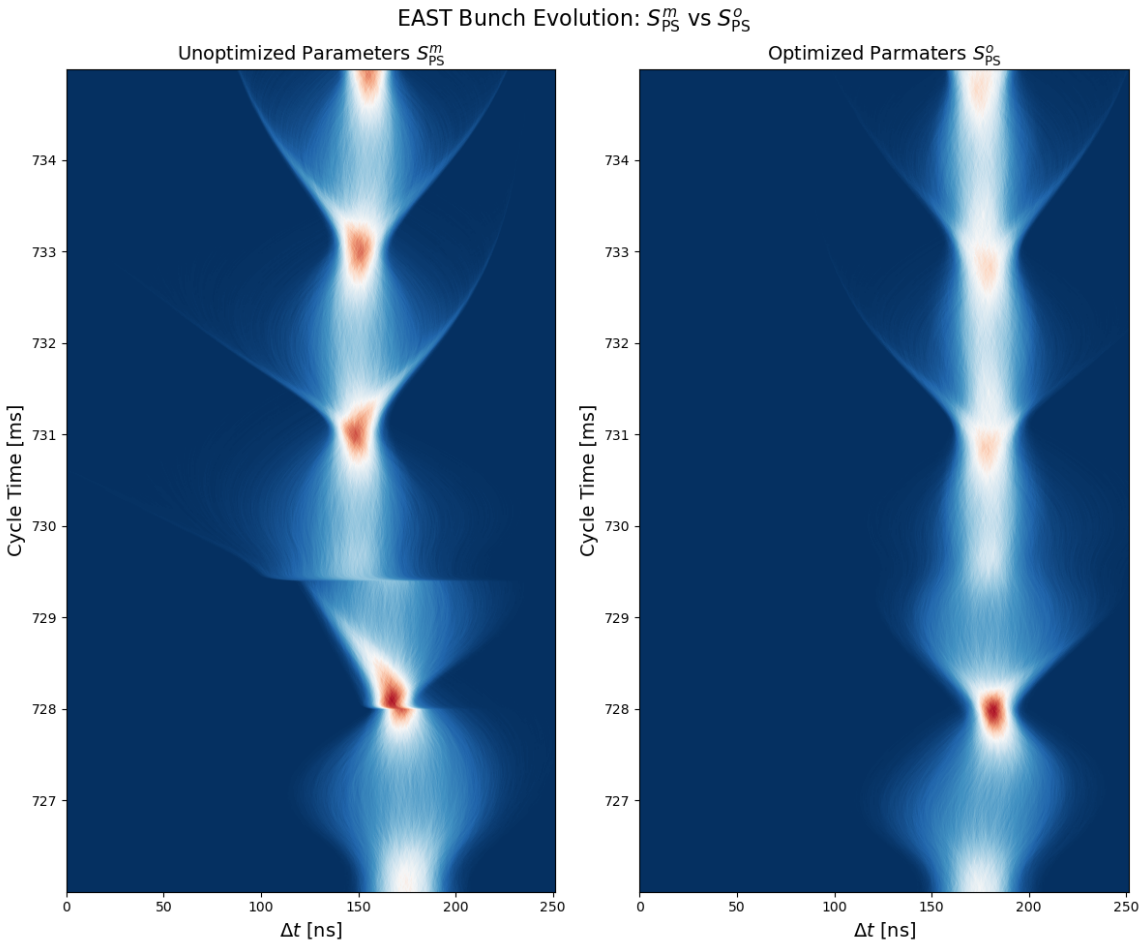

Figure 4.5.3: Waterfalls of the EAST bunch produced by simulations with the reference parameters set S^m_{PS} (left) and the optimized one S^o_{PS} (right). The EAST bunch quality degradation is visibly reduced for S^o_{PS}.

However, these EAST bunch quality improvements come at the cost of the TOF front tail length, as the reduced phase jump asymmetry and changes to the start time $\tau_{s,1}$ also impact TOF. Figure 4.5.4 shows that in the optimized case, the TOF bunch is extracted later than optimal, while also being more symmetric than for S^m_{PS}. This leads to the increase of the front tail length g_T shown in Table 4.5.1. Nonetheless, the bunch length remains below the target of 28 ns, fulfilling the imposed and primary target for TOF. If the increase in the secondary target of TOF tail length proves problematic in operation, the GPO's weights can also be adjusted to find a solution with shorter g_T, at cost to the other bunch quality metrics.

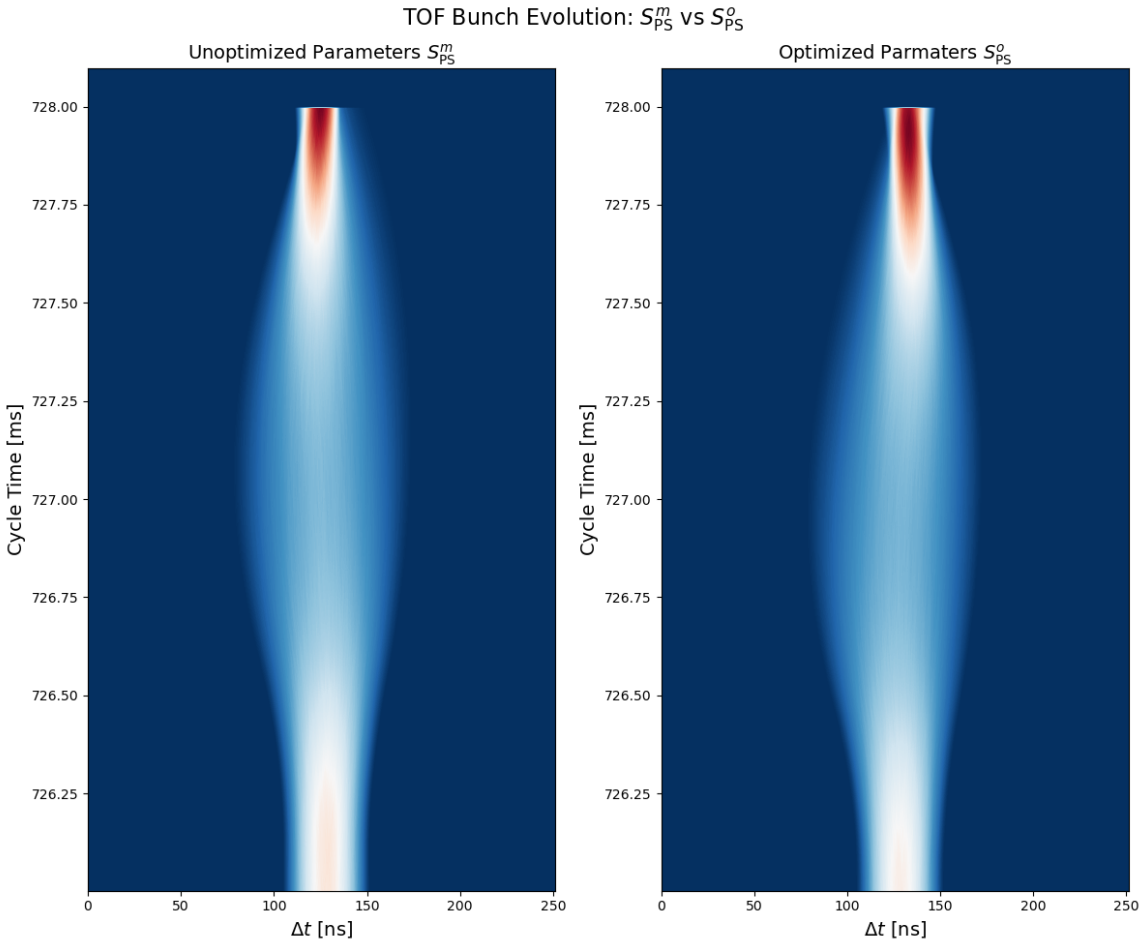

Figure 4.5.4: Waterfalls of the TOF bunch produced by simulations with the reference parameters set S^m_{PS} (left) and the optimized one S^o_{PS} (right). The bunch appears to be extracted later than optimal for S^o_{PS}.

Overall, the GPO yields a parameter set S^o_{PS}, which improves the EAST bunch quality significantly at the cost of an elongation of the TOF tail length. Therefore, it shows

promise in being able to aid with finding an optimal parameter set during e.g. beam commissioning, possibly yielding significantly better results than the manually determined parameter set S^m_{PS}. The runtime of approximately a day to produce these results further suggests the GPO's use in beam commissioning or when needing to set up the phase jumps after a change in cycle or machine parameters. However, these are still theoretical results, and the errors demonstrated in Section 4.4 mean that improvements shown here will not necessarily translate to exactly the same kind of improvements in the actual cycle.

4.5.2. Intensity Limitations

In view of making the PS more flexible, studying the behaviour of the PS BigTOFEAST cycle at higher intensities is relevant. As stated in Section 4.1, increasing particle flux delivered to the n_TOF experiment with the parasitic TOF bunch in the BigTOFEAST cycle would free up time for other beam cycles in the PS by reducing the amount of dedicated TOF beam cycles necessary. Hence, determining the intensity limitations under which acceptable radiation safety and bunch quality can still be maintained, while producing optimal TOF and EAST bunches; is particularly important from an operational point of view.

As the intensity in the simulations used by the GPO is easily adjustable, this task becomes simple to perform with the developed optimizer: to evaluate intensity limitations, the GPO is used to find the optimal parameters for a given intensity with a maximal TOF bunch length of 30 ns, while a focus is laid on minimal losses. TOF tail length and EAST oscillation amplitude are also still optimized, however losses take precedence, as they are the most important parameter for accelerator operation and safety.

To accomplish this, the weights defined in Eq. (4.3.2) are changed to

$$\begin{aligned} w_1 &= 50 \quad w_2 = 1 \quad w_3 = 1 \\ w_4 &= 10 \quad w_5 = 10. \end{aligned} \tag{4.5.2}$$

This heavily penalizes the GPO for going above the maximal TOF bunch length and

for any incurred losses, while reducing the relative importance of the TOF tail length and EAST quadrupole oscillation amplitude.

Performing a total of four optimizations, with 30 iterations each, and for TOF bunch intensities of $I_T \in \{350, 500, 650, 800\} \cdot 10^{10}$ protons, produces the Tables (4.5.2) and (4.5.3). Note that the intensity of the EAST bunch is fixed to $I_T/10$ for each optimization.

I_T [10^{10} protons]	$\phi_{1,\uparrow}$	$\phi_{1,\downarrow}$	$\tau_{s,1}$ [ms]	$\tau_{j,1}$ [ms]	$\tau_{s,2}$ [ms]	$\tau_{j,2}$ [ms]
350	144.12°	130,42°	726.029	0.451	729.355	0.329
500	148.90°	164.06°	726.149	0.428	729.699	0.361
650	154.48°	152.08°	726.094	0.432	729.378	0.401
800	148.92°	136.56°	726.117	0.428	729.502	0.451

Table 4.5.2: Settings determined to be optimal for minimizing particle losses while maintaining TOF bunch lengths $l_T < 30$ ns, for four different bunch intensities. The EAST bunch intensity is always set to a tenth of the TOF bunch intensity, $I_E = I_T/10$.

I_T [10^{10} protons]	l_T [ns]	g_T [ns]	A_E [ns]	L_E [%]	$\mathcal{L} \cdot 100$
350	28.29	4.20	24.28	0.12	2.9822
500	28.73	3.41	30.07	0.19	3.1064
650	28.29	3.80	22.05	0.28	3.0445
800	29.40	4.33	22.27	0.08	2.8500

Table 4.5.3: Bunch quality metrics from simulations performed for different intensities with the optimized settings in Tab. (4.5.2). TOF losses L_T remain at 0 % for all settings.

In detail, Table (4.5.2) shows that the optimal settings for different intensities vary strongly: a change in intensity changes the behaviour of the loss function $\mathcal{L}$ significantly, shifting the locations of the minima. Therefore, the GPO predicts that an increase in intensity will degrade bunch quality metrics at settings optimized for the original intensity. However, optimal settings for the new intensity may be found, for which the bunch quality barely degrades, as seen in Table (4.5.3).

The table shows the bunch quality metrics for all four parameter sets, and the loss $\mathcal{L}$ remains approximately the same for all intensities, only shifting slightly due to slightly different ways each optimization run scans the parameter space. For all four cases, the GPO manages to find settings with negligible EAST losses $L_E < 0.3$ % (TOF losses remain at $L_T = 0$ % for all settings), while maintaining a bunch length close to

28 ns. Only g_T and A_E fluctuate for different intensities, where the GPO finds different tradeoffs, either reducing TOF front tail length in return for an increase in EAST quadrupole oscillation amplitude or vice versa. This happens due to these two metrics being highly deprioritized with the chosen weights (see Eq. (4.5.2)).

In conclusion, the GPO predicts that an intensity increase will not result in significant degradation of the bunch quality due to the first two phase jumps before extraction. Therefore, this section of the BigTOFEAST cycle should pose no bottleneck for intensity increases. This is highly significant operationally, as increasing the parasitic TOF bunch intensity to the same intensity used for the TOF bunch in dedicated beam cycle would allow all dedicated cycles to be replaced by the parasitic ones, i.e. BigTOFEAST.
This would significantly increase particle flux to the East Area, while also increasing the overall efficiency of the PS, and therefore the entire injector complex measurably. However, an increase in intensity will impact other sections of the cycle, with additional bunch degradation expected, especially during transition crossing, where η_0 switches sign. This will result in different bunch shapes at the start of the first flat top, i.e. different initial conditions for the simulations used herein. This change will likely impact the bunch quality metrics considered negatively, hence a higher intensity will result in worse bunch quality nonetheless. However, the GPO itself would likely still be able to find settings yielding degraded, although optimal quality metrics under these worsened initial conditions, as this would only necessitate a minor change in the initial conditions of the simulations used by the GPO.

4.6. Summary

Overall, the GPO proves to be a sensible tool when scrutinized theoretically: It produces the expected outcomes in simplified scenarios and physically sensible results under more complicated conditions. It also converges within approximately 30 iterations, meaning an optimization requires approximately 1.5 days of runtime using cluster computing services such as CERN's HTCondor [35]. However, further developments of the underlying loss function $\mathcal{L}$ are necessary to guarantee ideal GPO operations, and measurements are required to fully verify the GPO's results,

Using optimized phase jump settings for the operational BigTOFEAST cycle, a significant reduction in EAST bunch quadrupole oscillation amplitude A_E and losses L_E is predicted by the GPO at the cost of minor TOF tail length g_T increase: g_T increases by 10 %, while the EAST quadrupole oscillation amplitude A_E and losses L_E drop to 36 % and 6 % of their original values, respectively.
If these predictions are verified in operation, the GPO would therefore allow for major beam quality improvements for BigTOFEAST. The GPO would also be a powerful tool for further fine-tuning of the cycle if quality requirements are changed, and could be further developed for use in other operational cycles, such as the SFTPRO in Chapter 3.

Additionally, an increasing intensity is expected to significantly shift the optimal settings for the BigTOFEAST cycle, necessitating adjustment of the phase jump settings. Nonetheless, the GPO predicts that new, optimal settings producing similar quality results with negligible losses for both TOF and EAST can be found, as long as both bunches are brought to the first flap top without significant additional degradation due to the intensity increase. Otherwise, further adjustments will be necessary.

Both of these predictions will be tested during the initial startup of the PS in 2024. The results of these tests will be incorporated in the GPO development, with a focus laid on integration into operational use, if successful. On the other hand, if the predictions are proved incorrect, these results will be used to refine both the simulations and the optimization algorithm used by the GPO.

5. Conclusion and Outlook

Overall, both optimizations at the PS and SPS are performed successfully. At the SPS, the optimizations performed on the SFTPRO cycle with the help of measurements and tomographic reconstructions are able to produce a 7.3 % increase in energy distribution width. While this methodology produces good results, they are not as impactful as predicted, showing that the methodology does not reproduce the measured energy distributions fully accurately. Rather, the method captures the general trend of the energy distribution's evolution during a phase jump. The results could be further improved by e.g. using this method in conjunction with empty bucket channelling [36] or updating and reassessing the transfer function of used measurement equipment. Additionally, better integration of BLonD into the longitudinal tomography code could be developed to speed up the optimization process.

For the PS, the development of the GPO is also a success. The simulations used for optimization reproduce measurements in fine detail, and the GPO is able to provide physically sensible theoretical improvements to the BigTOFEAST cycle. In current operation, the GPO predicts that the degradation of the EAST bunch can be significantly reduced, lowering EAST losses to approximately 6 % of the nominal value. Additionally, EAST quadrupole oscillations could be reduced to 36 % of the nominal value, while having a relatively minor negative impact on the TOF bunch, raising front tail length by 10 %.
Additionally, the GPO predicts that the extraction process is not a major bottleneck when considering intensity increases, as optimal settings minimizing particle losses can be found for intensities up to $800 \cdot 10^{10}$ protons for TOF and $80 \cdot 10^{10}$ protons for EAST. This is highly significant operationally, as this would allow replacement of dedicated TOF beam cycles with parasitic BigTOFEAST cycles, measurably increasing flexibility and efficiency of the PS. However, these settings vary strongly for different intensities, necessitating significant adjustments of the phase jump settings for each chosen intensity. Given that initial bunch conditions at the first flat top will also change for different intensities, both operational adjustments and re-runs of the GPO will likely be necessary in all cases when optimizing extraction. However, the current results predict that this should be possible without significant beam degradation at

extraction.

To continue development of the GPO, the testing of its suggested, optimized settings on the operational cycle is the immediate next step. If this test proves the accuracy of the GPO's predictions, then the models developed by the GPO could be further refined and be used as operational tools, streamlining the process of manually adjusting phase jump settings. Additionally, if simulations accurately reflecting the dynamics in the SPS are integrated into the GPO, it could also be used to refine the SPS phase jump settings. Then, both methodologies from Chapters 3 and 4 could be compared against each other.

If the test shows that the GPO is inaccurate, further work in detailing the PS beam feedback loops and impedance model will be necessary to increase the accuracy of underlying simulations. In either case, further adjustments of the optimization process of the GPO, such as more detailed development of the loss function or refinements of the trade-off between exploration and exploitation during the optimization could also improve its performance.

Bibliography

[1] S. Chatrchyan et al., "Observation of a new boson at a mass of 125 GeV with the CMS experiment at the LHC", Physics Letters B **716**, 30–61 (2012).

[2] G. Aad et al., "Observation of a new particle in the search for the Standard Model Higgs boson with the ATLAS detector at the LHC", Physics Letters B **716**, 1–29 (2012).

[3] *N_tof - The neutron time-of-flight facility at CERN*, `https://ntof-exp.web.cern.ch/` (visited on 08/14/2023).

[4] E. Chiaveri et al., "Status and perspectives of the neutron time-of-flight facility n_tof at CERN", EPJ Web of Conferences **239**, Publisher: EDP Sciences, 17001 (2020).

[5] *NA62*, `https://home.cern/fr/science/experiments/na62` (visited on 08/14/2023).

[6] *NA64*, `https://home.cern/fr/science/experiments/na64` (visited on 08/14/2023).

[7] CERN, *Convention for the Establishment of a European Organization for Nuclear Research — CERN Council*, Sept. 2023, `https://council.web.cern.ch/en/content/convention-establishment-european-organization-nuclear-research`.

[8] E. Montbarbon et al., "The CERN East Area Renovation", Nuclear Instruments and Methods in Physics Research Section B: Beam Interactions with Materials and Atoms **461**, 98–101 (2019).

[9] D. Banerjee et al., "The North Experimental Area at the Cern Super Proton Synchrotron", `10.17181/CERN.GP3K.0S1Y` (2021).

[10] *ALICE*, `https://home.cern/science/experiments/alice` (visited on 08/11/2023).

[11] *ISOLDE*, `https://www.home.cern/science/experiments/isolde` (visited on 08/11/2023).

[12] *The CERN accelerator complex, layout in 2022*, https://cds.cern.ch/images/CERN-GRAPHICS-2022-001-1 (visited on 06/08/2023).

[13] G. Apollinari et al., *High Luminosity LHC Project Description*, technical report (2014), https://cds.cern.ch/record/1974419.

[14] M. Benedikt et al., "FCC-ee: The Lepton Collider: Future Circular Collider Conceptual Design Report Volume 2. Future Circular Collider", 10.1140/epjst/e2019-900045-4 (2019).

[15] H. Timko et al., "Beam longitudinal dynamics simulation studies", Physical Review Accelerators and Beams **26**, Publisher: American Physical Society, 114602 (2023).

[16] BLonD, *CERN Longitudinal Beam Dynamics Simulation Code*, http://blond.web.cern.ch.

[17] F. Tecker, *Longitudinal Beam Dynamics in Circular Accelerators*, Introductory CAS Lecture, Budapest, Feb. 2016, https://cas.web.cern.ch/sites/default/files/lectures/budapest-2016/tecker.pdf.

[18] G. Dôme, *The SPS acceleration system travelling wave drift-tube structure for the CERN SPS*, technical report (1976), https://cds.cern.ch/record/319440.

[19] D. Quartullo, "Simulations of RF beam manipulations including intensity effects for CERN PSB and SPS upgrades", Ph.D. Thesis (Sapienza – Università di Roma, Rome, Feb. 2019).

[20] Fraser, M. et al., "Production of slow extracted beams for CERN's East Area at the Proton Synchrotron", IPAC 2023, 10.18429/JACOW-IPAC2023-MOPA099 (2023).

[21] Y. Baconnier et al., "Extraction from the CERN SPS", IEEE Transactions on Nuclear Science **24**, Conference Name: IEEE Transactions on Nuclear Science, 1434–1436 (1977).

[22] R. Garoby, *RF gymnastics in synchrotrons*, arXiv:1112.3232, Dec. 2011.

[23] K. Ng, *Physics of Intensity Dependent Beam Instabilities* (World Scientific, Dec. 2005).

[24] G. Rumolo et al., *Collective effects in Beam Dynamics*, USPAS Course, 2015, https://uspas.fnal.gov/programs/2015/ODU/courses/collective-effects.shtml.

[25] A. Lasheen, *Numerical noise due to binning in macroparticle simulations*, technical report (Jan. 2022), https://cds.cern.ch/record/2798923.

[26] R. N. Bracewell, *Fourier Transform and Its Applications*, 3rd edition (2000).

[27] A. Lasheen, *PS Longitudinal Impedance Model*, Mar. 2020, https://zenodo.org/record/4722835 (visited on 05/31/2023).

[28] A. Lasheen Et Al., "Measurements of SPS Longitudinal Impedance Model", CERN Proceedings, 73 (2017).

[29] S. Aumon, "Optimization of the Position of the Radial Loop Pickups in the CERN PS", IPAC 2010 (2010).

[30] F. M. Velotti, *Momentum Spread Measurements SPS*, Apr. 2022, https://gitlab.cern.ch/abt-projects/operation/sps/lss2/py_mom_spread_meas/-/tree/master (visited on 08/15/2023).

[31] C. Ahdida et al., *Findings of the Physics Beyond Colliders ECN3 Beam Delivery Task Force*, technical report (2023), https://cds.cern.ch/record/2847433.

[32] Cotte, D. et al., "Beam performance and operational efficiency at the CERN Proton Synchrotron", IPAC 2023, 1671–1674 pages, 0.97 MB (2023).

[33] C. Hernalsteens et al., *Design and Beam Measurements of Modified Fast Extraction Schemed in the CERN PS for Installing a Dummy Septum to Mitigate Ring Irradiation*, technical report (2013), https://cds.cern.ch/record/1591604.

[34] O. Naumenko and A. Lasheen, *Modelling of the PS Beam Phase and Radial Feedback Loops*, [Manuscript in preparation], 2024.

[35] D. Thain et al., "Distributed computing in practice: the Condor experience.", Concurrency - Practice and Experience **17**, 323–356 (2005).

[36] P. A. A. Sota et al., "RF techniques for spill quality improvement in the SPS", JACoW IPAC **2023**, MOPA116 (2023).

[37] H. Wiedemann, *Particle Accelerator Physics*, Graduate Texts in Physics (Springer International Publishing, Cham, 2015).

[38] K. R. Rao et al., "Discrete Fourier Transform", in *Fast Fourier Transform - Algorithms and Applications*, edited by K. Rao et al., Signals and Communication Technology (Springer Netherlands, Dordrecht, 2010), pages 5–40.

[39] C. H. Grindheim and S. Albright, *Longitudinal Phase Space Tomography Version 3*, technical report (2021), `https://cds.cern.ch/record/2750116`.

[40] C. H. Grindheim, "A Python Library for Longitudinal Beam Tomography", PhD thesis (HVL, Norway, 2020).

[41] C. E. Rasmussen and C. K. I. Williams, *Gaussian processes for machine learning*, Adaptive computation and machine learning (MIT Press, Cambridge, Mass, 2006).

Appendix

A. Small Oscillations in Longitudinal Phase Space

To gain an intuitive understanding of the dynamics described in Sections 2.3 and 2.4, analysing how the system behaves under a small excitation is instructive. To simplify, the arrival time difference Δt is transformed to the RF phase $\varphi(\Delta t) = \omega_{\mathrm{rf}}\Delta t + \chi_{\mathrm{rf}}$, and acceleration δE_0 is assumed to be constant and small, implying $\omega_{\mathrm{rf}}, T_{\mathrm{rev},0}, \chi_{\mathrm{rf}} \approx \mathrm{const.}$. Further setting $N_{\mathrm{rf}} = 1$, equations (2.3.8), (2.3.9) become:

$$\dot{\Delta E}(t) = \frac{q}{T_{\mathrm{rev},0}} V_{\mathrm{rf}}(\sin(\varphi(t)) - \sin(\varphi_0)). \tag{A.1.1}$$

$$\dot{\varphi}(t) = \left(\frac{\omega_{\mathrm{rf}}\eta_0}{(\beta_0)^2 E_0}\right) \Delta E(t), \tag{A.1.2}$$

Note that the synchronous phase φ_0 satisfies, by its definition in the previous section, $\sin(\varphi_0) = \delta E_0 / q V_{\mathrm{rf}}$.

Taking the second time derivative of φ, the equations of motion reduce to

$$\ddot{\varphi}(t) = \frac{\omega_{\mathrm{rf}}\eta_0}{(\beta_0)^2 E_0} \frac{q V_{\mathrm{rf}}}{T_{\mathrm{rev},0}} (\sin(\varphi(t)) - \sin(\varphi_0)). \tag{A.1.3}$$

Now assuming a small amplitude deviation of the RF phase from the synchronous one, $\varphi(t) \approx \varphi_0 + \Delta\varphi(t)$ with $\Delta\varphi \ll 1$, the sine can be expanded in the small angle approximation:

$$\begin{aligned} \ddot{\Delta\varphi}(t) &\approx \frac{\omega_{\mathrm{rf}}\eta_0}{(\beta_0)^2 E_0} \frac{q V_{\mathrm{rf}}}{T_{\mathrm{rev},0}} \cos(\varphi_0)\Delta\varphi(t) \\ &:= -\Omega_s^2 \Delta\varphi(t), \end{aligned} \tag{A.1.4}$$

with the synchrotron frequency

$$\Omega_s = \sqrt{\frac{\omega_{\mathrm{rf}}}{(\beta_0)^2 E_0} \frac{q V_{\mathrm{rf}}}{T_{\mathrm{rev},0}} (-\eta_0 \cos(\varphi_0))}.$$

This is the equation of a harmonic oscillator with an oscillation frequency of Ω_s. Therefore, as long as the stability condition $\eta_0 \cos(\varphi_0) \leq 0$ is fulfilled, the solution is

$$\varphi(t) = \varphi_0 + A\cos(\Omega_s t + \theta), \tag{A.1.5}$$

with the oscillation amplitude $A = \max\{\varphi(t)\} - \varphi_0$ and a phase offset θ. Differentiating Eq. (A.1.5) and inserting into Eq. (A.1.2) yields the solution for $\Delta E(t)$, which also becomes a sinusoidal oscillation with the same frequency Ω_s.

This means that the particle coordinates follow elliptical orbits in phase space if starting close to the synchronous phase, as can be seen in Fig. (A.1.1). Most importantly, the phase and energy amplitudes both stay constant. Consequently, a particle bunch which is initially centred around the reference particle (e.g. Fig. (2.3.1)) will remain centred this way, i.e. it will remain stable.

The aforementioned stability condition meanwhile implies that for $\eta_0 > 0$ (meaning accelerator operation above transition crossing), the synchronous phase must fulfil $\varphi_0 \in [\frac{\pi}{2}, \frac{3\pi}{2}] (\mathrm{mod}\ 2\pi)$. This is the case for the beams considered in this thesis. Especially in the case of no acceleration $\delta E_0 \equiv 0 \implies \varphi_0 = \pi$ according to Eq. (2.3.1), where the result of the arcsin principal branch has to be shifted by π to lie in the range $[\frac{\pi}{2}, \frac{3\pi}{2}]$.

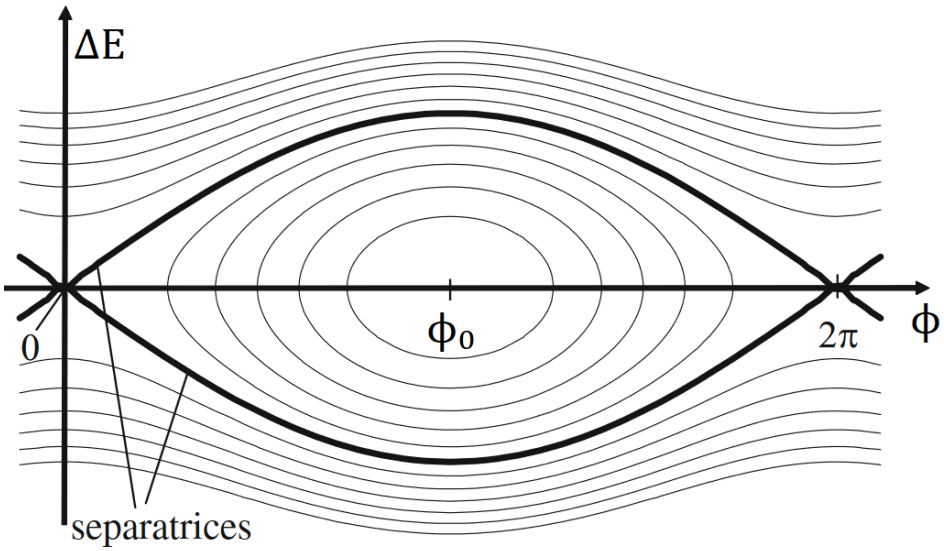

Figure A.1.1: Longitudinal phase space diagram, showing orbits of the particle coordinates $(\varphi, \Delta E)$ in the case of no acceleration. Orbits close to the synchronous phase φ_0 are elliptical and closed, forming stable trajectories. As they come closer to the separatrices they deform, and after passing the separatrices, they become open and unstable.
Source: adapted from [37].

B. The BLonD Library and Benchmarks

This chapter elaborates on the numerical tools used in optimizing the quality of beams. First, focus is laid on the structure of the BLonD library, which is used to simulate longitudinal particle dynamics in accelerators [15, 16]. Drawing upon the theoretical knowledge of Chapter 2, reference values for all necessary numerical simulation parameters are then determined to be able to run the simulations with minimal error.

B.1. The BLonD Code

The BLonD code is structured in building blocks, which allow the user to construct a longitudinal beam dynamics simulation to the desired level of accuracy and neglect or include certain aspects, such as collective effects. There are three core building blocks implemented as classes, feeding information into a tracker class, which applies the longitudinal equations of motion. As can be seen in Fig. (B.1.1), the three core blocks are:

1. The ring: contains machine parameters such as circumference C, bending radius ρ and slippage parameter η. Also receives information about the desired energy program $E_0^{(n)}$, i.e. what energy the reference particle has at each turn. Thereby also defines magnetic field, revolution time, etc., at each turn.

2. The beam: contains the $(\Delta t, \Delta E)$ phase space coordinates of each particle at the current turn and is able to calculate beam statistics, such as average bunch length, based on that information.

3. The RF station: contains RF station parameters such as voltage $V_{\mathrm{rf}}^{(n)}$ and RF frequency $\omega_{\mathrm{rf}}^{(n)}$ for each turn. Therefore also defines the synchronous phase $\varphi_0^{(n)}$ and conversion from time to phase coordinates, $\varphi(\Delta t) = \omega_{\mathrm{rf}} \Delta t + \chi_{\mathrm{rf}}$.

Based on the information provided by the ring and RF station, the "Ring and RF tracker" then applies the equations of motion (Eq. (2.3.6), (2.3.7)) to the coordinates saved in the beam class, updating them turn by turn. Note that the parameters of the reference particle are already saved in the ring class for every turn at the start of the simulation.

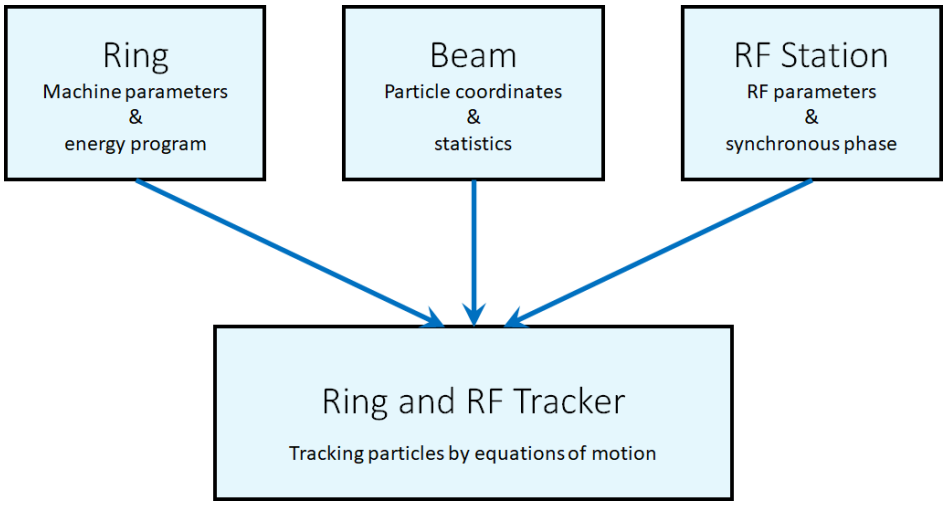

Figure B.1.1: Core structure of the BLonD code. The three main classes are passed to the Ring and RF Tracker, which performs the particle tracking turn by turn.

For more complex simulations, e.g. ones including collective effects, auxiliary building blocks can be used. The most commonly used ones, shown in Fig. (B.1.2), are:

1. The profile: this class calculates the line density λ. Specifically, it creates a histogram of λ by slicing a given Δt interval into N_{slice} equally spaced slices and counting how many particles are in each slice. This enables the calculation of the beam spectrum via fast Fourier transform (FFT), where each slice is an FFT bin.

2. The induced voltage: Given the profile's slicing of the considered Δt interval and beam spectrum, this class is responsible for calculating the total induced voltage V_{ind} and applying the corresponding kick to the particles in the beam. For this, it must also be provided information about the machine impedance by way of impedance models, e.g. [27],[28].

3. Various classes for data acquisition: as the name suggests, these take desired information, plotting or saving it directly to disk, as the user desires.

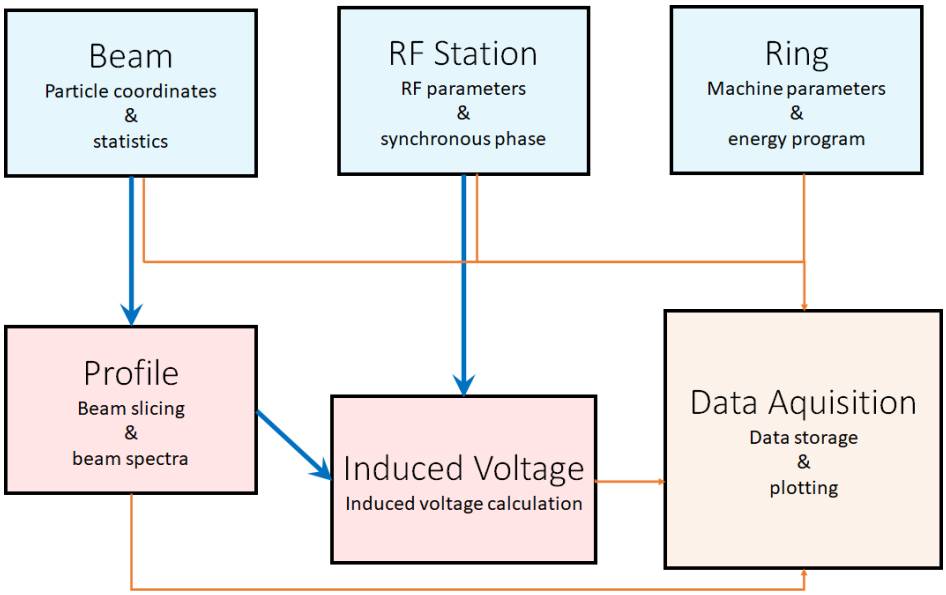

Figure B.1.2: Structure of auxiliary blocks of the BLonD code, allowing e.g. inclusion of collective effects. Blue arrows represent the dependencies of the depicted building blocks on each other. Orange arrows depict that all the data produced in the respective blocks may be stored and visualized.

B.2. Error and Noise

B.2.1. Theoretical Considerations

A major problem for beam dynamics simulations are the particle numbers: as each particle is tracked individually and a beam usually contains on the order of $10^{12} - 10^{13}$ particles, the runtime and memory necessary to simulate all particles would be enormous. To alleviate this, a certain number N_p of so called macroparticles to be tracked is chosen, which simply represent multiple real particles. For example, if a simulation with 10^{13} protons uses 10^6 macroparticles, each macroparticle represents 10^7 particles and has a charge of $q = 10^7 \cdot e$, with e being the elementary charge. These macroparticles are then used in the simulation instead, reducing computational complexity but introducing error.

Additional error is also introduced by tracking a certain fraction of buckets N_b of the total beam to reduce computational complexity, e.g. only $N_b = 2000$ out of $h = 4620$ total buckets in the SPS. Similarly, further error is caused by discretizing the beam into $N_s = N_b N_{sb}$ slices in the profile class, which directly specifies a number of slices per bucket, N_{sb}. These two error sources solely impact the FFT for calculating the induced voltage, and are therefore only relevant for collective effects. However, due

to the sensitivity of the phase jump to the initial particle distribution, these can still affect the studied dynamics significantly.

To gain benchmark values for N_b, N_{sb}, one can observe the FFT's frequency resolution

$$\Delta f = \frac{1}{N_{\text{sample}} \Delta T_{\text{data}}} = \frac{1}{T_{\text{data}}}, \tag{B.2.1}$$

and maximal resolved frequency [38]

$$f_{\max} = N_{\text{sample}} \Delta f = \frac{1}{\Delta T_{\text{data}}}. \tag{B.2.2}$$

Here $T_{\text{data}} = N_{\text{sample}} \Delta T_{\text{data}}$ and ΔT_{data} are the timeframe spanned by the FFT data in the time domain and the corresponding time resolution, respectively.
In the case of the FFT of a beam profile, N_{sample} is the amount of slices of the beam profile, $N_{\text{sample}} = N_s = N_b N_{sb}$. Additionally, the amount of buckets sliced is directly given by $T_{\text{data}} = N_b T_{\text{rf}}$, assuming T_{rf} to be a constant or an average bucket width of the given accelerator during the simulated timeframe.

As discussed in Section 2.7, ω_0 in Eq. (2.7.11) defines a natural frequency resolution of the beam spectrum. Therefore, to fully resolve it, the FFT benchmark frequency resolution $\overline{\Delta f}$ must correspond to ω_0:

$$\begin{aligned} \overline{\Delta f} &= \frac{\omega_0}{2\pi} = \frac{c}{C} \\ \implies \overline{T_{\text{data}}} &= \frac{C}{c} = T_{\text{rev},0}. \end{aligned}$$

Therefore, to resolve all details of the beam spectrum, one must simulate all buckets of the accelerator,

$$\begin{aligned} \overline{T_{\text{data}}} &:= \overline{N_b} T_{\text{rf}} = T_{\text{rev},0} \\ \implies \overline{N_b} &= \frac{T_{\text{rev},0}}{T_{\text{rf}}} = h. \end{aligned} \tag{B.2.3}$$

Meanwhile, the impedance models used for the simulation have a maximal frequency up to which they are defined [27], [28]. So for a given maximal frequency $\overline{f_{\max}}$, one obtains

$$\begin{aligned} \overline{f_{\max}} &= \frac{1}{\overline{\Delta T_{\text{data}}}} = \frac{\overline{N_s}}{\overline{T_{\text{data}}}} = \frac{\overline{N_b}\overline{N_{sb}}}{\overline{N_b} T_{\text{rf}}} \\ \implies \overline{N_{sb}} &= \overline{f_{\max}} T_{\text{rf}} \end{aligned} \tag{B.2.4}$$

Establishing a benchmark for the amount of macroparticles to use is more difficult, but can be done by considering the numerical noise generated by discretization of the line density within the profile class. Assuming a Bi-gaussian line density for the bunches, the signal-to-noise ratio SNR(f) between the bunch spectrum and the spectrum of the noise at a given frequency is [25]

$$\text{SNR}(f) = \sqrt{N_{pb}} \left(\frac{2}{\pi}\right)^{\mu+2} \frac{\Gamma(\mu + \frac{3}{2})}{(\tau_l f)^{\mu+1}}.$$

Here, N_{pb} are the macroparticles per bunch, Γ is the gamma function, τ_l is the full bunch length, meaning the length of the Δt interval which contains all particles of the bunch, and μ is a parameter classifying the bunch shape. $\mu = 1$ means the bunch follows a parabolic distribution, while it becomes Gaussian as $\mu \to \infty$.
Rearranging therefore yields a benchmark number of macroparticles $\overline{N_{pb}}$ per bunch, depending on the SNR:

$$\overline{N_{pb}}(f) = \left[\left(\frac{\pi}{2}\right)^{\mu+2} \frac{(\tau_l f)^{\mu+1}}{\Gamma(\mu + \frac{3}{2})} \text{SNR}(f) \right]^2.$$

If at least SNR $= 1$ is desired, the benchmark number of particles per bunch for a given maximal frequency $\overline{f_{\max}}$ becomes

$$\overline{N_{pb}} = \left[\left(\frac{\pi}{2}\right)^{\mu+2} \frac{(\tau_l \overline{f_{\max}})^{\mu+1}}{\Gamma(\mu + \frac{3}{2})} \right]^2. \tag{B.2.5}$$

Summarizing all three results of Equations (B.2.3), (B.2.4) and (B.2.5), the main relevant parameter for error and noise is the maximum resolved frequency $\overline{f_{\max}}$ of the beam spectrum and impedance. Therefore, these equations present a trade-off between numerical error, mainly affecting the calculation of collective effects, and runtime due to the increased number of particles and profile slices. If one desires to only resolve low-frequency contributions to the collective effects, e.g. ones due to the kickers and

main cavities of an accelerator, a low runtime can be maintained. However, if one takes into account all impedance contributions, the runtime will either significantly increase, or additional error will have to be introduced by lowering the number of slices or macroparticles.

B.2.2. Practical Applications for the PS and SPS

Applying Equations (B.2.3), (B.2.4) and (B.2.5) to both beam cycles covered in this thesis, the concrete benchmarks are as follows:

The SPS SFTPRO cycle has bunches with a length of $\tau_l \approx 1.7$ ns and $\mu \approx 3.5$ just before the phase jump and extraction based on measurements in 06.2023. The major impedance contributions lie at $f_{\max} = 200$ MHz due to the RF cavities. These main 200 MHz cavities contribute up to $f_{\max} = 1.4$ GHz, with contributions from additional components ranging up to $f_{\max} = 3$ GHz. The corresponding benchmark values of $\overline{N_b}, \overline{N_{sb}}$ and $\overline{N_{pb}}$ are shown in Table (B.2.1).

SPS Benchmark Values			
Value	$\overline{f_{\max}} = 200$ MHz	$\overline{f_{\max}} = 1.4$ GHz	$\overline{f_{\max}} = 3$ GHz
$\overline{N_b}$	4620	4620	4620
$\overline{N_{sb}}$	1	7	15
$\overline{N_{pb}}$	1	600	580'000

Table B.2.1: Numerical benchmark values for the SPS SFTPRO cycle near extraction with $\tau_l \approx 1.7$ ns and $\mu \approx 3.5$, with $T_{\text{rf}} \approx 5$ ns.

In the PS, the BigTOFEAST cycle has 2 bunches, with the TOF bunch having a significantly higher μ than the EAST bunch. Therefore, the average TOF and EAST bunch length of $\tau_l \approx 80$ ns seen in the PS BigTOFEAST cycle, and the TOF bunch's $\mu \approx 2{,}5$ will be considered for the benchmarking. The major impedance contributions lie at $f = 3.8$ MHz and $f = 20$ MHz due to the main 10 MHz and 20 MHz cavities. Additional contributions lie at 40,80 and 200 MHz due to further RF cavities. The benchmark values for three main limits of $f_{\max} = 25$ MHz, $f_{\max} = 80$ MHz and $f_{\max} = 200$ MHz are shown in Table (B.2.2).

PS Benchmark Values			
Value	$f_{\max} = 25$ MHz	$f_{\max} = 80$ MHz	$f_{\max} = 200$ MHz
$\overline{N_b}$	8	8	8
$\overline{N_{sb}}$	7	21	52
$\overline{N_p}$	207	711'000	434'000'000

Table B.2.2: Numerical benchmark values for the PS BigTOFEAST cycle, during the first flat top with $\tau_l \approx 80$ ns, $\mu \approx 2.5$, and $T_{\text{rf}} \approx 262.25$ ns.

C. Longitudinal Phase Space Tomography

Longitudinal phase space tomography is used, like all tomographic techniques, to reconstruct a D dimensional space from multiple $(D-1)$ dimensional projections of that space. In this specific case, the $D = 2$ dimensional longitudinal phase space is reconstructed by measurements of the time projection, i.e. the profile $P(\Delta t)$ at different times t [39, Ch.1]. This is possible due to the synchrotron motion the particles perform in phase space (see Fig. (2.5.1)), meaning that the measured time projections sample the phase space distribution at different "angles" for different times t.

C.1. Basic Principle

The following explanation leans heavily on [39]. For further details and the concrete implementation of the longitudinal phase space tomography code used in this thesis, both [39] and [40] are therefore heavily recommended.

To perform longitudinal phase space tomography, henceforth just tomography, two sets of data are necessary:

1. Measured profiles $P_j(\Delta t)$, $j = 1, 2, ..., K$, where P_j is measured at time t_j, with $t_j < t_{j+1}$. The measurement is usually discretized, i.e. the profile $P_j(X_l)$ is only measured at discrete Δt values, forming Δt bins $X_1, \ldots, X_L$ (see Fig. (C.2.1)).

2. The evolution of a simulated phase space distribution. This is given via particle coordinates $\Delta t_{i,j}$ and $\Delta E_{i,j}$ for times t_j, where $i = 1, 2, \ldots, N_p$ numbers the particles and j the time. Therefore, the measured profile P_j corresponds to the profile of the simulated distribution at time t_j with particle coordinates $\Delta t_{i,j}$ and $\Delta E_{i,j}$.

   For the simulation performed to obtain these particle coordinates, the initial distribution is chosen to be homogeneous in the area enclosed by the separatrix, as seen in Fig. (C.1.1). For this, $\Delta t_{i,1}$ values are evenly distributed in the Δt-interval where $P_1(\Delta t) > 0$ has been measured. The separatrix is then computed via Eq. (2.4.3), defining ΔE-intervals in which particles are again homogeneously

placed. The evolution of these coordinates is then computed numerically to obtain $\Delta t_{i,j}$ and $\Delta E_{i,j}$ for all t_j.

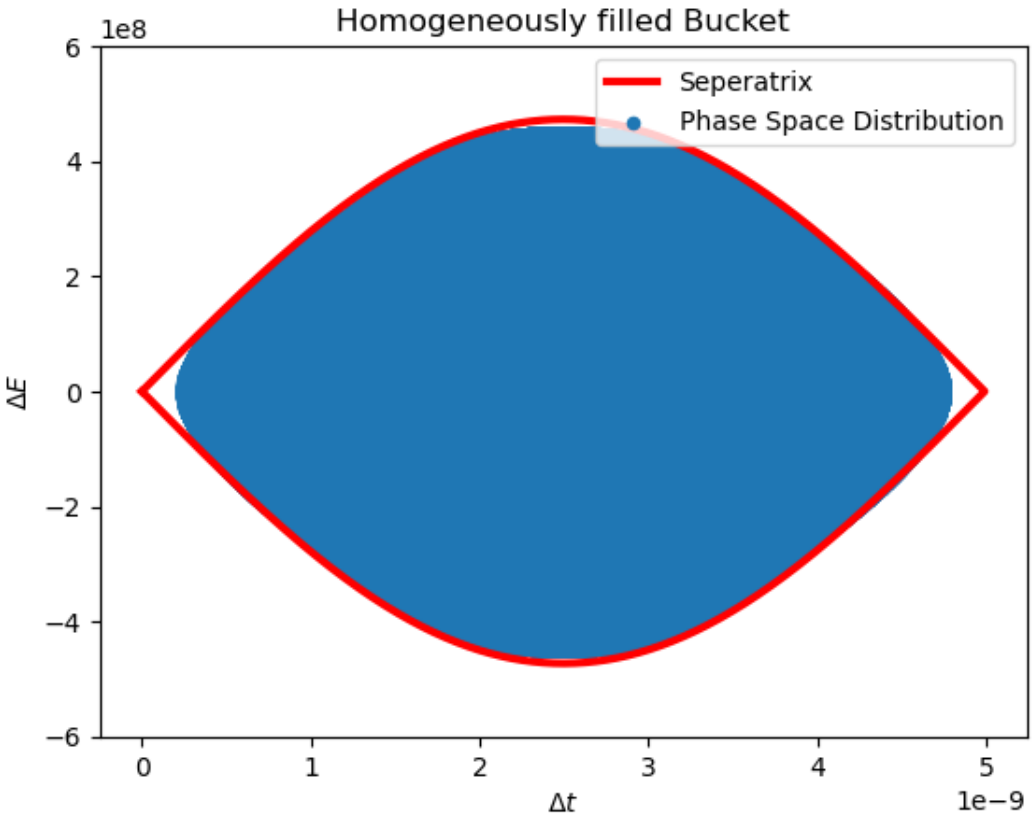

Figure C.1.1: A bucket filled with a homogeneous distribution of particles, used as an initial distribution for the particle tracking simulations necessary for tomography. The edges are not filled due to the measured profile having decayed to 0 before reaching that area.

Given these two initial data sets, the main tomography algorithm iteratively assigns each particle a weight $g_i \geq 0$ with which it contributes to the reconstructed phase space. These weights are optimized such that measured and reconstructed profiles differ as little as possible. Each algorithm iteration is divided into three steps:

C.2. Back Projection

In the first step, the measured profiles are used to adjust the particle weights. For this, the simulated particle coordinates are discretized into bins to match the discretized measurement data, creating a profile histogram $\overline{P_j}(X[i])$, as seen in Fig. (C.2.1). This yields L Δt bins $X_1, ..., X_L$, with $X[i]$ denoting the bin particle i is in.

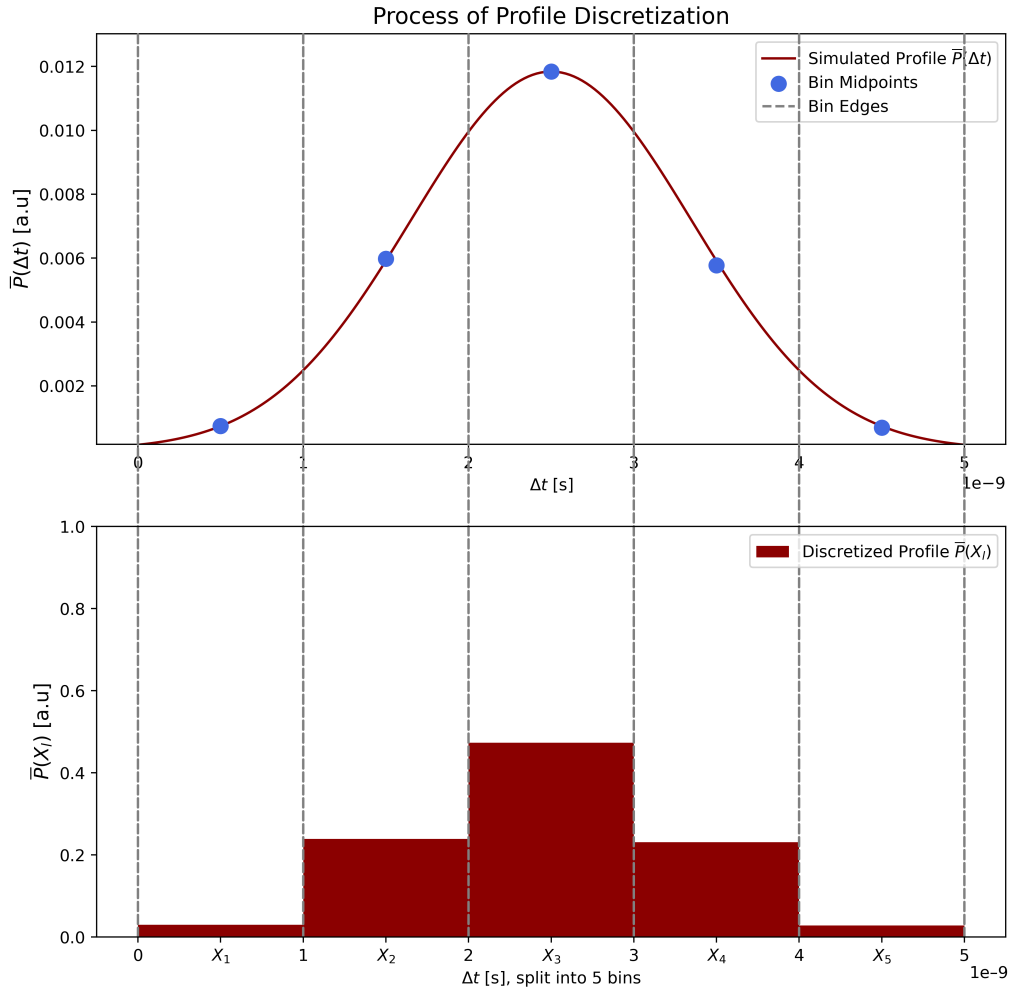

Figure C.2.1: The top plot shows the simulated, continuous profile $\overline{P}(\Delta t)$. It is discretized by dividing the x-axis into 5 Δt bins $X_1, ..., X_5$ of length 10^{-9} s, with the bin midpoints marked in blue and edges marked with grey lines. The corresponding, discretized profile $\overline{P}(X_l)$ is shown in the bottom plot, and is used in the main tomography algorithm.

Then, each particle's weight is adjusted according to

$$g_i = g_i + \sum_{j=1}^{K} \Delta P_j(X[i]). \tag{C.2.1}$$

Here, $\Delta P_j(X[i]) = P_j(X[i]) - \overline{P_j}(X[i])$ is the difference between the measured and reconstructed profiles for each particle i at time t_j. Initially, $g_i = 0\ \forall i$ and $\Delta P_1(X[i]) = P_1(X[i])\ \forall i$. Fig. (C.2.2) shows an example of how particle weights are updated for $N_p = 2$ particles and $K = 5$ identical profile differences ΔP_1,...,ΔP_5.

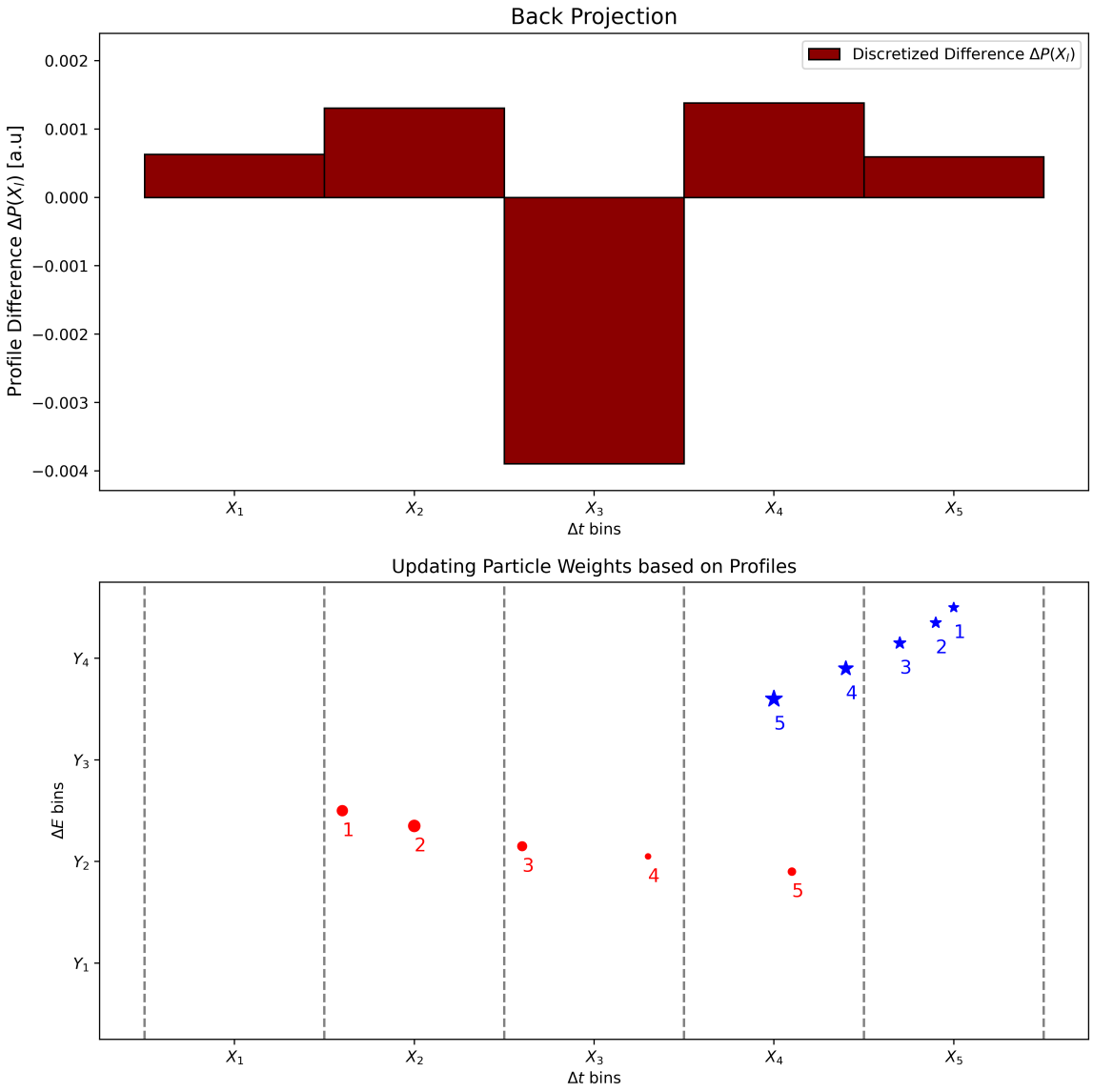

Figure C.2.2: The top plot shows the discretized profile difference $\Delta P_j(X_l)$, which is assumed to be identical for $K = 5$ input and simulated profiles.
The bottom plot displays the weights of two particles updated based on their coordinates and $\Delta P_j(X_l)$. The marker size indicates the weight of the corresponding particle, with it growing or falling proportionally to the profile difference $\Delta P_j(X_l)$ in the particle's bin for time t_j.
Source: modified from [39].

C.3. Projection

Given the particle weights g_i, a weighted projection is performed as a second step to obtain the reconstructed profile. To this end, the weights of all particles in a bin X_l are summed, and the resulting profile normalized to match the normalization of the measured profiles. Concretely, each iteration is performed by calculating

$$\overline{P_j}(X_l) = \sum_{i \in I_l} g_i, \text{ with } I_l = \{i \,|X[i] = X_l;\ i = 1, 2, ..., N_p\}, \tag{C.3.1}$$

for each simulated profile $\overline{P_j}$ and then multiplying $\overline{P_j}$ by a normalization factor defined by the normalization chosen for the measured profiles P_j.

C.4. Difference

Finally, the difference at iteration j

$$\Delta\tilde{P_j}(X_l) = P_j(X_l) - \overline{P_j}(X_l) \tag{C.4.1}$$

is calculated. Additionally, to improve convergence, $\Delta\tilde{P_j}(X_l)$ is multiplied by a weighing factor based on the number of particles $N_p(X_l)$ in the bin X_l to obtain the final difference $\Delta P_j(X_l)$:

$$\Delta P_j(X_l) = \Delta\tilde{P_j}(X_l)\frac{\max\limits_{1 \le l \le L}\{N_p(X_l)\}}{N_p(X_l)}. \tag{C.4.2}$$

This ensures that the reconstructed profiles converge quickly, even for bins with few particles, e.g. at the tails of profiles. The total weight in those tail bins is smaller than for bins with many particles, so even a small difference in weight should affect a significant change, which this weighing ensures.

C.5. Energy Distribution Reconstruction

This process is now performed for the desired number of iterations or until the algorithm converges below a desired difference. The resulting weights can then be used to recreate the energy distribution $N(Y_l)$ similarly to Eq. (C.3.1)

$$N(Y_l) = \sum_{i \in I_l} g_i, \text{ with } I_l = \{i \,|Y[i] = Y_l;\ i = 1, 2, ..., N_p\},$$

where Y_l is the l-th energy bin, gained by discretizing the ΔE-axis of the simulated phase space.

D. Gaussian Processes

This appendix essentially is a short summary of [41], containing the minimum knowledge necessary to gain an overview over what Gaussian processes are and how they are used in this thesis. For full details on Gaussian processes and their application beyond their usage in this thesis, the reader is highly encouraged to read through [41].

D.1. Motivation and Definitions

A difficult to evaluate, possibly non-differentiable function $f : \mathbb{R}^n \to \mathbb{R}$ is given, which needs to be optimized, i.e. a global extremum found, in the fewest possible evaluations. Since the gradient and the function itself is unknown, the function values are assumed to be randomly distributed, following a normal distribution at each point $x_i \in \mathbb{R}^n$: $f(x_i) \sim \mathcal{N}(\mu_i,\sigma_i^2)$ with μ_i being the mean and σ_i^2 the variance of f at x_i. Formally:

A **Gaussian process** is a collection of random variables (e.g. $f(x_i)$ at each x_i), any finite of which have a joint Gaussian distribution.

This joint Gaussian distribution the Gaussian process induces is specified fully by the mean m and covariance k functions, defining the distribution at each point:

$$\begin{aligned} m(x) &= \mathbb{E}[f(x)] \\ k(x,x') &= \mathbb{E}[(f(x) - m(x))(f(x') - m(x'))], \end{aligned} \tag{D.1.1}$$

and one writes

$$f(x) \sim \mathcal{GP}(m(x), k(x,x')). \tag{D.1.2}$$

Given the assumption of $f(x_i)$ being normally distributed at each x_i, an evaluation of f at a specific point x^* allows an update of the distributions $f(x_i)$ by updating the covariances. Simply speaking: If the value of $f(x_*)$ is exactly known at x_*, then the variance of $f(x_i)$ in the neighbourhood around x_* will be significantly reduced.

This updating of the distribution $f(x_i)$ via the covariance function $k(x,x')$ means that a Gaussian process "learns" and becomes more accurate as more points are evaluated.

It also allows single function evaluations at x to make a significant impact on the surrounding distributions of f around x, even though f might not be differentiable. How much the neighbourhood of x is impacted depends on the covariance function k, also called **kernel**. These updates affecting not just $f(x)$, but all distributions in a neighbourhood, reduce the amount of evaluations needed to optimize f. However, this comes at the cost of not being fully accurate, as the model is a statistical model. Figure (D.1.1) shows this learning process.

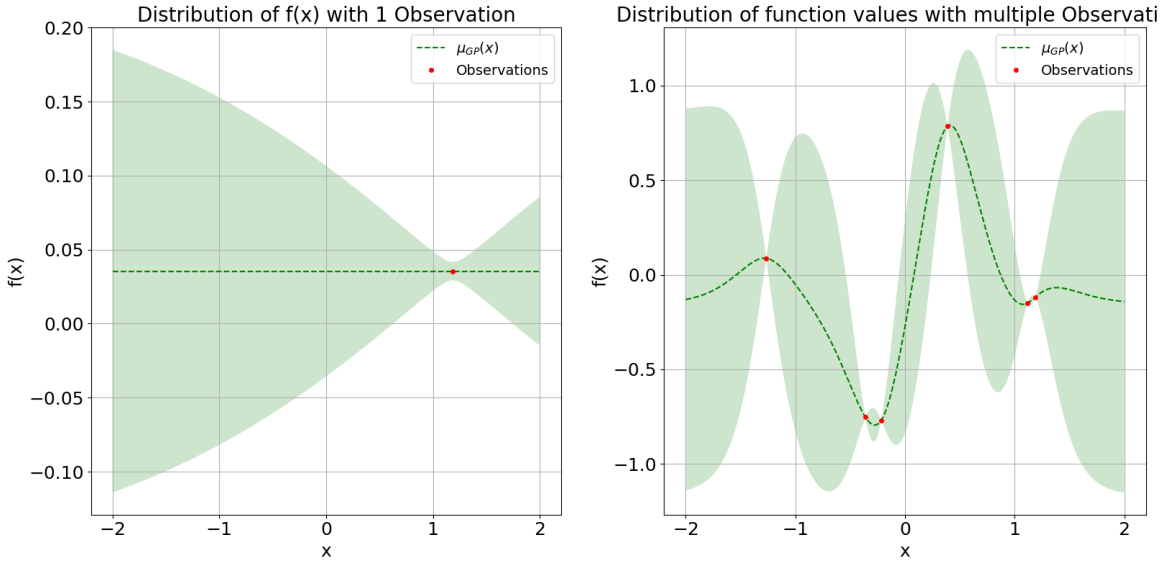

(a) Gaussian process with only 1 observed point.

(b) Gaussian process after 6 observed points.

Figure D.1.1: The mean $m(x)$ (dotted green line) and variance $k(x,x)$ (green shading) of a target function distribution $f(x)$ for different numbers of observations. On the left, only 1 point has been observed, i.e. f has only been evaluated there. On the right, 5 more points have been observed, updating the variance in their neighbourhoods and yielding a better approximation of the target function f.

D.2. Updating the Function Distributions

Given a new point the function is evaluated at, the updating of function distributions is possible because of Bayes' Rule: Given a set of M points $X_* = \{x_{*,i} | i = 1, 2, ..., M\}$ the function has been evaluated at and the corresponding function values $y_* = (y_{*,1}, ..., y_{*,M}) \in \mathbb{R}^M$ at those points, the update is performed as follows: looking at the conditional distribution $(f|x,y_*,X_*)$, i.e. how f is distributed at the point x, given that f has assumes the values y_* at X_*, one can prove:

$$f_* := (f|x,y_*,X_*) \sim \mathcal{N}(\mathbb{E}[f_*], \mathrm{cov}(f_*)), \tag{D.2.1}$$

with

$$\begin{aligned} m_*(x) &:= \mathbb{E}[f_*(x)] = m(x) + K(X_*,x) \cdot K(X_*,X_*) \cdot (y_* - m(X)) \\ k_*(x,x') &:= \mathrm{cov}[f_*](x,x') = k(x,x') - K(X_*,x)^T \cdot K(X_*,X_*)^{-1} \cdot K(X_*,x). \end{aligned} \tag{D.2.2}$$

Here, $m(X) = (m(x_1), m(x_2),...)$, and $K(X,Z)$ is the covariance matrix between all points $x_i \in X \subset \mathbb{R}^n$ and $z_j \in Z \subset \mathbb{R}^n$:

$$K(X,Z) = \begin{pmatrix} k(x_1,z_1) & k(x_1,z_2) & k(x_1,z_3) & ... \\ k(x_2,z_1) & k(x_2,z_2) & k(x_2,z_3) & ... \\ ... & ... & ... & ... \end{pmatrix}.$$

Therefore, new function evaluations adjust the mean and kernel of the Gaussian process, allowing it to "learn" as the function is evaluated at additional points. The goal is for the mean $m(x)$ to eventually resemble the target function f near the desired optimum. However, m itself does not influence the learning of the Gaussian process significantly. Instead, as shown in Eq. (D.2.2), the main cause of adjustments to both m and k is the covariance matrix K, and therefore the kernel k itself.

D.3. Process Kernels (Covariance Functions)

Given that the kernel k defines the way the Gaussian process "learns", it is worth studying in more detail. In fact, it defines assumptions about the type of function f the Gaussian process is estimating, and should be adjusted based on the problem to be solved.

First, k must fulfil the following properties to be a well-defined covariance function:

$$k(x_i, x_j) \geq 0 \; \forall i,j \qquad \text{(Positive semidefinite)}$$

$$k(x_i, x_j) = k(x_j, x_i) \; \forall i,j \qquad \text{(Symmetry)}$$

To speak of continuity and differentiability of a Gaussian process, i.e. of the continuity and differentiability of the distributions $f(x)$ at each point, these terms need to be defined for general stochastic processes.

Mean Square Continuity: Consider a sequence of points $(x_k)_{k\in\mathbb{N}}$ with x_∞ defined such that $\lim_{k\to\infty} |x_k - x_\infty| = 0$. Then a stochastic process $f(x)$ is continuous in mean square at x_∞ if $\lim_{k\to\infty} \mathbb{E}[|f(x_k) - f(x_\infty)|^2] = 0$.

This definition also implicitly defines a limit in mean square : The stochastic process $f(x)$ tends towards its limit L at x_∞ in mean square, i.e. $\overline{\lim_{x\to x_\infty}} f(x) = L$ iff $\overline{\lim_{k\to\infty}} \mathbb{E}[|f(x_k) - L|^2] = 0$.

Mean Square Differentiability: Therefore, the partial derivative of a stochastic process can also be defined in a standard manner. The partial derivative of $f(x)$ in the i-th direction, with e_i being the corresponding unit vector, is

$$\frac{\partial f(x)}{\partial x_i} := \overline{\lim_{h\to 0}} \frac{f(x + he_i) - f(x)}{h},$$

and it is well-defined as long as the mean square limit on the right exists.

Given these definitions, one can prove the following statements:

If k and k' are kernels, then:

$$\tilde{k} = k + k' \text{ and } \bar{k} = k \cdot k' \text{ are both kernels} \tag{1}$$

$$f \text{ (mean square) continous at } x_* \iff k(x, x') \text{ continous at } x = x' = x_* \tag{2}$$

$$\frac{\partial f(x)}{\partial x_i} = \frac{\partial^2 k(x, x')}{\partial x_i \partial x_i'} \tag{3}$$

(1) means that one can combine different kernels to define the desired assumptions about the function f studied. (2) and (3) state how the choice of kernel affects the studied function: A continuous kernel will produce continuous functions, a twice differentiable

one will produce differentiable functions, and so on. Therefore, one should choose the kernel based on the physical process being modelled. Examples of commonly used kernels are:

1. **The square exponential:**

$$k_{SE}(r) = S_f^2 \exp(-\frac{1}{2}(r^T \cdot M_l^2 \cdot r)),$$

with $r = x - x'$, S_f being the signal strength and M_l defining the characteristic length scales for the different variables in $r \in \mathbb{R}^n$, e.g. $M_l = \text{diag}[(\frac{1}{l_1}, \frac{1}{l_2}, ..., \frac{1}{l_n})]$. This kernel is smooth, hence the Gaussian process will assume that the function searched for is also smooth. Most physical processes in a high-dimensional parameter spaces are not fully smooth, however. Hence, a kernel that is twice or quadruply differentiable in x and x' might therefore be of use:

2. **The Matérn Kernel:**

$$k_M(r, \nu) = S_f^2 \left[\frac{2^{1-\nu}}{\Gamma(\nu)} \left(\sqrt{2}\nu M_l \cdot r \right)^\nu K_\nu \left(\sqrt{2}\nu M_l \cdot r \right) \right], \tag{D.3.1}$$

with Γ being the gamma function, and K_ν the modified Bessel function of the second kind. This kernel is very rough for low ν and easy to evaluate for half integer ν: At $\nu = \frac{1}{2}$, the searched for function has no guarantee to be differentiable. At $\nu = \frac{3}{2}$ it is at least once differentiable, for $\nu = \frac{5}{2}$ twice differentiable, etc. Therefore, physically $\nu = \frac{3}{2}$ and $\nu = \frac{5}{2}$ are usually interesting.

D.4. Hyperparameter Optimization

In the examples of the previous sections, the matrix M_l of length scales has been defined. These length scales define how strongly the covariance varies as the corresponding parameters vary. For example, if $r_i = (a,b,c) \in \mathbb{R}^3$, set $M_l = \text{diag}[(\frac{1}{l_a}, \frac{1}{l_b}, \frac{1}{l_c}))]$. Then if $l_a = 10$ and $l_b = 1$, variations in a will result in significantly smaller changes to the covariance k in the neighbourhood of r_i, than those same variations in b.

The length scales are examples of hyperparameters: parameters of the kernel itself. For the kernel to find the correct function modelling a selected physical process, these

hyperparameters should be set correctly. However, the optimal hyperparameters are not always known. Nonetheless, they can be dynamically adjusted during the optimization carried out with the Gaussian process by studying the marginal likelihood $p(y|X,\theta)$. This is the likelihood that M observed values $\mathbb{R}^M \ni y_* = f(x_{*,i})$ at M points $x_{*,i} \in X_*$ will be modelled correctly by the Gaussian process with the current kernel, whose hyperparameters are described in the hyperparameter vector $\theta = (\theta_1, \theta_2, \dots)$. The logarithm of the marginal likelihood is calculated as

$$\ln[p(y_*|X_*,\theta)] = -\frac{1}{2} y_*^T \cdot K(X_*, X_*; \theta)^{-1} \cdot y_* - \frac{1}{2} \det(K(X_*, X_*; \theta)) - \frac{n}{2} \ln(2\pi).$$

Here, $K(X,Z;\theta)$ is simply a more detailed notation for the previously defined covariance matrix $K(X,Z)$, noting that K might depend on the hyperparameters themselves. In the equation, the first term determines how well the actual data y is fitted with the current kernel hyperparameters, and the second one penalizes the complexity of the model via $\det(K)$. The third term is simply a normalization.

Minimizing the logarithm of the marginal likelihood with respect to θ yields

$$\frac{\partial}{\partial \theta_j} \ln(p(y_*|X_*,\theta) = \frac{1}{2} \mathrm{tr} \left((\alpha(X_*;\theta) \cdot \alpha(X_*;\theta)^T - K(X_*,X_*;\theta)^{-1}) \frac{\partial K(X_*,X_*;\theta)}{\partial \theta_j} \right),$$

with $\alpha(X;\theta) = K(X,X;\theta)^{-1} \cdot y_*$. This can now be used to find values of θ_j which set the above derivative to 0, therefore maximizing the marginal likelihood and optimizing the kernel to fit observed data.

Selbstständigkeitserklärung

Hiermit versichere ich, dass ich die vorliegende Masterarbeit selbstständig verfasst habe und keine anderen als die angegebenen Hilfsmittel und Quellen verwendet habe. Alle Stellen, die wörtlich oder sinngemäß aus anderen Quellen übernommen wurden, habe ich als Entlehung kenntlich gemacht.

Hiermit erklärt ich weiterhin, dass diese Arbeit in gleicher oder ähnlicher Form noch keiner Prüfungsbehörde vorgelegen hat.

Genf, 05.03.2024

Ort, Datum

Unterschrift